

**Quantum rotor tunnelling in methyl
ethyl ketone and acetophenone studied
using field-cycling NMR techniques**

Thesis submitted to the University of Nottingham for the degree of

Doctor of Philosophy by

Sabah Abu-Khumra, M.Sc.

Under the supervision of

Prof. A. J. Horsewill

2013

Contents

CHAPTER 1 INTRODUCTION.....	1
<i>1.1 Introduction</i>	1
<i>1.2 The NMR spectrum of tunnelling methyl group</i>	6
CHAPTER 2 THEORETICAL.....	16
<i>2.1 Fundamental principles of tunnelling</i>	16
2.1.1 The de Broglie Wavelength and the Heisenberg uncertainty principle	16
2.1.2 Coherent and incoherent tunnelling.....	18
<i>2.2 NMR Theory.....</i>	18
2 . 2 . 1 . Relaxation Times.....	19
2 . 2 . 2 . Spin-lattice relaxometry.....	20
2 . 2 . 3 . Applications of Measuring Relaxation Times.....	24
<i>2.3 Hydrogen Bond Quantum Tunnelling.....</i>	24
2.3.1 NMR spin-lattice relaxometry (homonuclear case)	25
2 . 3 . 2 . NMR relaxometry.....	27
2.3.3. Models incorporating tunnelling.....	27
<i>2.4 Tunnelling Properties of Methyl Group Rotation.....</i>	29
2.4.1 Spin symmetry species.....	30
2.4.2 The thermodynamics of the methyl group.....	31

2.4.3 Manifestation of methyl group reorientation in nuclear magnetic resonance.....	33
2.5 <i>Methyl ethyl ketone and Acetophenone (low field experiments)</i> ..	36
2.5.1Transitions that involve an A to E change in rotational state.	36
2.5.2 Heat capacities of Zeeman and tunneling reservoirs	40
2.5. 3 Methyl ethyl ketone	41
2.5. 4 Acetophenone.....	43
2.6 <i>Fundamental theoretical principles for dynamic tunnelling polarization (DTP) experiments</i>	44
2.6.1 Collection of Non-Interacting Spins :- Bulk Magnetization.	44
2.6.1.1 Rotational Tunnelling	45
2.6.1.2 The Methyl Rotor, CH ₃	47
2.6.1.3 The Exclusion Principle applied to CH ₃	48
2.6.2 Dipolar and Zeeman orders.....	50
2.6. 3 Polarization by forbidden transitions.....	56
2.6. 4 Adiabatic field changes.....	58
2.6. 5 The investigation of Methyl tunnelling spectra.....	58
2.6.5.1 The investigation of tunnel resonance through the level crossing technique.....	59
2.6. 5.2 The investigation of NMR tunnel resonance spectra.	59

CHAPTER 3 EXPERIMENTAL 63

3.1 Introduction to pulsed NMR spectroscopy	63
3.2 NMR pulse sequence.....	66
3.2.1. Saturation recovery pulse sequence.....	66
3.2.2. Curve fitting.....	68
3.3 The NMR spectrometer.....	69
3.4 Methods in data treatment.....	72

CHAPTER 4 DYNAMIC TUNNELLING POLARIZATION : ACETOPHENONE.....80

4.1 The conventional low field scan and Dynamic Tunnelling Polarization.....	80
4.1.1. Conventional Low Field scan.....	80
4.1.2. Dynamic Tunnelling Polarization	82
4.2 The effect of changing the irradiation time in the (b-) region....	89
4.3 The effect of changing the level crossing delay time in the (b-) region.....	91
4.4 The Level Crossing Spectrum.....	92
4.5 The tunnelling relaxation time.....	94
4.6 The relative heat capacities of the Zeeman and tunnel reservoirs.	100
4.7 The Spin-Lattice Relaxation Time T_1 Measurements.....	102

CHAPTER 5 DYNAMIC TUNNELLING POLARIZATION :	
METHYL ETHYL KETONE.....	107
<i>5.1 The conventional low field scan and Dynamic Tunnelling</i>	
<i>Polarization scan</i>	108
5.1.1. Conventional Low Field scan.....	108
5.1.2. The DTP pulse sequence	109
5.1.3 Dynamic Tunnelling Polarization (DTP) scans	110
<i>5.2 The effect of changing the Zeeman polarization time on the spectrum</i>	
5.2.1. The effect of changing the polarization time in the (180)G low field case.....	116
5.2.2. The effect of changing the polarization time in the (290)G low field case.....	122
<i>5.3 The effect of changing the irradiation time on the spectrum</i>	
5.3.1. The effect of changing the irradiation time in the (180)G low field case	124
5.3.2. The effect of changing the irradiation time in the (290)G low field case	126
<i>5.4 The Spin-Lattice Relaxation Time T_1 Measurements.....</i>	
<i>5.5 The Level Crossing Spectrum.....</i>	
	130
	133

<i>5.6 Measuring the lifetime of the A and E states: relaxation of the tunnelling reservoir.....</i>	135
<i>5.7 The Relative Heat Capacity.....</i>	144
CHAPTER 6 Conclusions and discussions.....	148
CHAPTER 7 BIBLIOGRAPHY	154

Abstract

In the solid state the rotation of a methyl group is hindered by a potential barrier and at low temperature the rotational motion is characterised by quantum tunnelling. The Pauli Exclusion Principle imposes constraints on the allowable eigenstates of the methyl rotor and leads to a combination of spatial and spin variables. The characteristics of these quantum tunnelling states, labelled *A* and *E*, are explored experimentally and methods are investigated for creating prescribed non-equilibrium states. We will investigate and explore the tunnelling polarization associated with the *A* and *E* tunnelling-magnetic levels by means of field-cycling NMR. Secondary rf irradiation is used to drive *A-E* and *E-A* transitions associated with NMR tunnelling sidebands. This polarization is then transferred to the 1H Zeeman system at a field-dependent level-crossing where the methyl tunnelling frequency equals one or two times the 1H Larmor frequency. The level-crossing contact is a necessary step since the tunnel temperature cannot be measured directly with a pulse. A new pulse sequence is described and the resulting spectra are analogous to the solid effect and dynamic nuclear polarization. Therefore we assign the phrase ‘dynamic tunnelling polarization’ to describe the experiments. Two samples are studied in depth, methyl ethyl ketone and acetophenone which have tunnel frequencies of 495 and 1435 kHz respectively. The experiments investigate the phenomena as a function of a variety of physical parameters in order to determine the fundamental physics.

Acknowledgements

This thesis is dedicated to my beloved parents: Mrs Amal Al-Hitti and Mr Mowafaq Abu-Khumra and my brother and sister Uday and Wid Abu-Khumra.

Sincere thanks go to my PhD supervisor Professor Anthony J. Horsewill for all his kindly supervision throughout the last three years. I have acquired a great deal of knowledge about molecular quantum tunnelling and NMR from him, and for that I am truly grateful.

I would like to thank Dr. Ilya Frantsuzov for his guidance on the use of the field-cycling NMR spectrometer and the invaluable discussions regarding physics.

Thanks also go to Chris Pallender and David Holt for their help with helium supply and to Bob Chettle for his help in maintaining the NMR probes.

Finally, I would like to thank the University of Nottingham for the EPSRC scholarship support and the Iraqi postgraduate research scholarship.

Chapter 1 Introduction

1.1 Introduction

One of the motivations for the experiments to be discussed in this chapter was to explore experimental techniques for manipulating the tunnelling polarization in a prescribed manner. It is established in the literature how tunnel resonance experiments can use the magnetic field as a variable to bring the CH₃ tunnelling system into contact with a spin Zeeman system at a level crossing. However, while the ¹H Zeeman polarization that is created at such a tunnel resonance can be measured with a resonant rf pulse, there are no published techniques for determining the tunnelling polarization. Therefore insight can usually only be obtained by numerical simulation and published work rarely reports an experimental determination of the CH₃ tunnelling states that arise.

In the solid state the motion of atoms and molecular sidegroups is usually hindered by the presence of a potential barrier. As a result molecular dynamics is often described by an Arrhenius rate law represented in terms of an activation energy closely related to the barrier height. The Arrhenius description is predominantly a classical one, based on Newtonian mechanics. However, for light atoms and molecular subgroups, the de Broglie wavelength can be of similar order to the barrier width, meaning quantum tunnelling pathways become available for barrier crossing. In this thesis we shall investigate particular examples where quantum tunnelling dominates the molecular dynamics.

At the beginning we identify two forms of tunnelling. Firstly, incoherent tunnelling arises when there is asymmetry between the well regions characterising ‘reactants’ and ‘products’ on either side of the barrier. Here, the energy mismatch means energy exchanging interactions with the ‘environment’ are required to theoretically describe

the barrier crossing process. This usually involves the intervention of phonons and the process is a stochastic barrier crossing one characterised by a rate. Secondly, coherent tunnelling characterises the rotation of symmetrical groups such as the methyl group, CH_3 . Here the molecular symmetry means there is symmetry in the potential energy surface and the tunnelling is characterised by a coherent frequency. The dynamical properties of such quantum rotors are also strongly influenced by the Antisymmetry Principle, equivalently the Pauli Exclusion Principle, which impose strict constraints on the allowable quantum states. This leads to an entanglement of space and spin variables and the identification of ‘spin-symmetry species’ or ‘nuclear spin-isomers’.

Proton transfer in the hydrogen bond is a simple type of chemical reaction. It is important to many biological processes. In the simplest description it is characterised by a double minimum potential which is coupled to a heat bath or ‘reservoir’. Due to the wave-like nature of matter, the barrier between the two wells becomes partially ambiguous and quantum mechanics permits new barrier penetrating pathways. The proton becomes delocalised and there is the possibility of proton transfer by quantum tunnelling which is a significant research subject to understand its motions.

Tunnelling matrix components provide the pathways for proton transfer across the barrier so quantum effects dominate the low temperature dynamics. These ideas have been investigated in the benzoic acid (BA) dimer, which has been studied extensively [1, 2, 3, and 4].

Benzoic acid (BA) forms dimers linked by a pair of hydrogen bonds. The system is coupled to internal and external vibrational modes of the host molecule; see Figure 1.1. The two wells of the potential correspond to the two tautomers, Figure 1.1, and interdimer interactions in the solid state lead to the weak energy asymmetry. At higher

temperature there is dynamic disorder and coordinated double proton transfer occurs within the hydrogen bonds, characterised by the correlation time τ_c , [1].

We can study the dynamics of the proton transfer by employing the NMR relaxometry method [1]. Here, magnetic field-cycling is incorporated in a conventional spin-lattice relaxation pulse sequences to enable T_1 to be recorded as a function of applied field.

Plotting the spin-lattice relaxation rate as a function of magnetic field maps out the spectral density , enabling a direct measurement of the correlation time that characterises the motion.

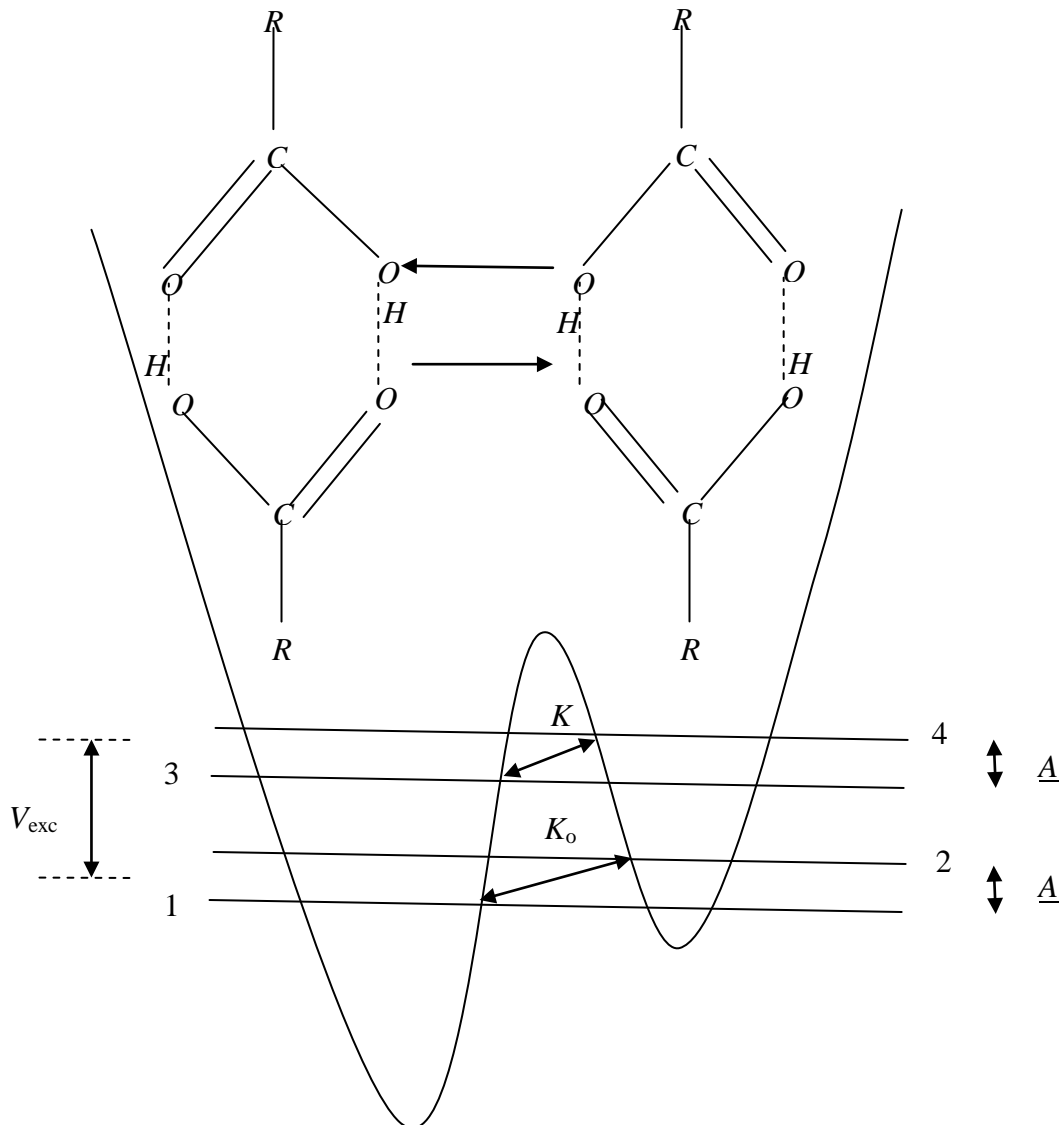


Figure 1.1: Sketch of the benzoic acid dimer showing the asymmetric double well potential and the ground and first excited states. Proton transfer is mediated by the tunnelling pathways shown.

In principle, NMR has exceptional resolving power and is a highly effective technique for measuring molecular dynamics. However, there are instrumental constraints, for example to obtain an acceptable signal-to-noise ratio in the received signal the transmitter and receiver coils must be a part of a tuned rf circuit, and this severely limiting the technique ability. Additionally, commercial superconducting magnet systems operate in persistent mode and this also severely restricts the range of accessible magnetic field. In these circumstances, spin-lattice relaxation

measurements can only be made at a chosen spot of frequency and the interpretation of T_1 data invariably requires fitting with a theoretical model. For classical motional processes where the dynamics are well-characterised by, for example, an Arrhenius rate law, this procedure can be perfectly adequate. However, when there are strong quantum aspects to the motion any theoretical description may not be well-founded and it is desirable to have a model for the interpretation of the data. For example, the inverse spin-lattice relaxation directly maps out the spectral density function. To determine the spectral density it would be better to have measurements over a wide range of magnetic field (and hence Larmor frequency) in order that the dynamics may be characterised directly without assuming any functional form to the spectral density. By adopting field-cycling procedures in NMR these requirements can be met making the technique highly effective for molecular dynamics.

An example of a quantum rotor that has been investigated widely concerns the quantum tunnelling behaviour of the methyl group CH_3 . The spin-symmetry substantially affects the dynamics of the CH_3 rotor which has a high level of spatial symmetry; this is an example of coherent tunnelling where the probability of finding the protons oscillates among the three potential wells. As with proton transfer in the hydrogen bond, field-cycling NMR provides a very effective technique for studying the tunnelling dynamics. However, with quantum rotors an additional motivation for field-dependent studies comes from the fact that the tunnelling-magnetic energy level diagram exhibits level-crossings at particular magnetic fields where the tunnelling frequency is equal to the ^1H Larmor frequency ω_L or twice the Larmor frequency $2\omega_L$. This is the topic of methyl tunnelling resonance, which will be important to the research in this thesis.

1.2 The NMR spectrum of a tunnelling methyl group: -

Tunnelling: - Consider a quantum particle in a two-well potential (Figure 1.2) [5].

Because the wave function of the particle according to quantum mechanics is not confined to its potential well, there is a small probability for the molecule to pass through the energy barrier without receiving the classically expected energy. A classic example is of the ammonia molecule [6],

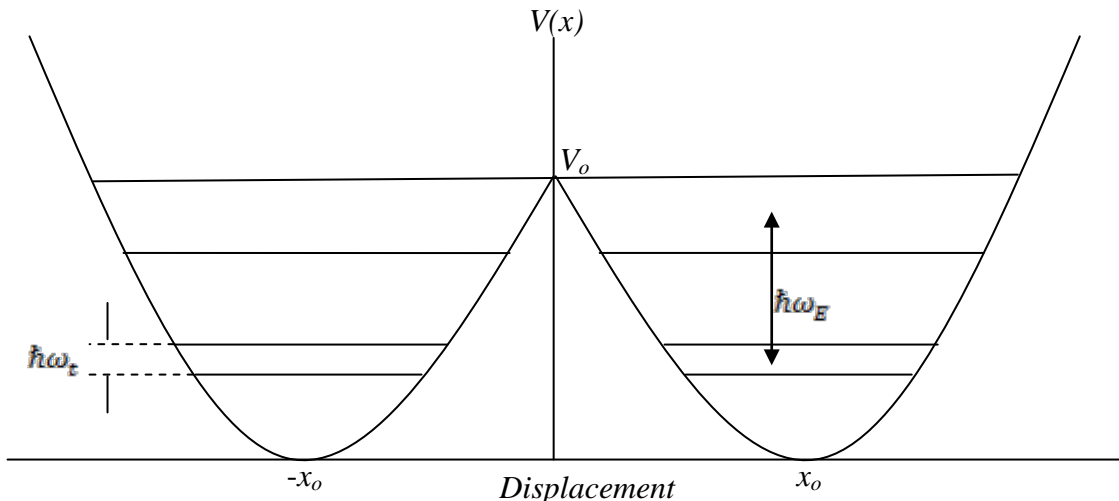


Figure 1.2 The ammonia molecule potential energy surface and its inversion (tunnelling) splitting ($\hbar\omega_t$) of the oscillator ground state. $\hbar\omega_E$ is the harmonic oscillator energy splitting.

The tunnel splitting ($\hbar\omega_t$) of the levels within a pair appears since the harmonic oscillator positioned at x_o and $-x_o$ are not stationary states. There is a limited overlapping of the wavefunction beneath the barrier which gives rise to the splitting. The splitting defines the tunnelling frequency ω_t which relies on the fraction of the barrier height to the oscillator energy (where $V_o > \hbar\omega_E$).

This translational tunnelling has the same basic characteristics as rotational tunnelling. The hindering barrier confines the particles among two equivalent sites. The measurement of barrier height can be undertaken at elevated temperatures using BPP theory [21] of thermally activated random re-orientations; the gradient of an Arrhenius

plot of the spin-lattice relaxation time vs. inverse temperature is equal to the activation energy, which yields an estimate of the barrier height. Knowing the barrier height can lead to an estimate of the tunnelling frequency, ω_t by solving the Schrödinger equation.

Powder N.M.R. lineshapes of methyl groups: -

The NMR lineshape of a methyl group can be computed assuming an equilateral triangle of protons rotating about the C_3 axis. In practice, the observed lineshape is much narrower. This observation is explained by motional narrowing, which gives rise to a partial averaging of the dipolar interactions. For strongly hindered methyl groups the NMR absorption spectrum is narrow at room temperature and shows systematic broadening as the temperature is reduced. However, for some materials containing methyl group, the NMR lineshape remains narrow down to low temperatures. In these cases the quantum tunnelling rotation of the methyl groups is responsible for the averaging of the dipolar interaction. However, such lineshape investigations do not provide a sensitive and accurate technique for studying tunnelling.

The reorientation of a methyl group about its 3-fold axis is hindered by non-bonding interactions between the hydrogen atoms and neighbouring atoms. The orientation of the methyl group relative to its equilibrium position is defined by an angle. If the barrier height is V_o then the potential may be written,

$$V = \frac{V_o}{2} (1 + \cos 3\phi)$$

Combining the rotation operator \mathcal{H}_R with \mathcal{H}_z and \mathcal{H}_d which are the Zeeman and dipolar interaction operators will produce the unsolved Hamiltonian

$$\mathcal{H} = \mathcal{H}_R + \mathcal{H}_z + \mathcal{H}_d \quad (1)$$

And its solution requires a detailed specification of the superposition for the space-spin states. The suggestion of Apaydin and Clough [7] that tunnelling is introduced into the

spin Hamiltonian \mathcal{H}_R by the interchange spin operator, which is $-2j(I_j \cdot I_k)$, represents a step into solving this problem. Since it correctly reproduces the tunnelling splitting ($\Delta = 3j$) between the A and E states. It was illustrated [7] that the solid lattice limit represents $j=0$ while with increasing dipolar interaction j values there will be an appearance of detailed spectral characteristics ending with the narrowed spectrum at $j=\infty$.

N.M.R. spin-lattice relaxation: -

The tunnel splitting of the torsional ground state of molecules is used successfully to analyze the N.M.R. line-shapes in contrast to the difficulty of explaining the spin-lattice relaxation. An efficient explanation for both of the lineshape changes as well as T_1 is provided by the BPP model [21] of random thermal re-orientation at higher temperatures. While at lower temperatures tunnelling as a coherent process does not explain the spin-lattice relaxation, the model of tunnelling frequency modulation (TFM) suggested by Allen and Clough [8] succeeded in explaining this problem. Here the tunnelling process and tunnelling relaxation is modulated by a thermal mixing of the ground and first excited torsional states. The interaction with the lattice drive this torsional excitation that are supposed to be spin-independent, so the symmetrical conversion from A to E and in the opposite way occurs without altering the spin which is a fault in the model. When the system temperature is raised rapidly, if we add up the transitions dominated by phonon absorption rather than emission processes, the result will be a decrease in the Zeeman polarization order to zero. But by considering the dipolar shifts of all the levels in the estimation of dipolar order, it will be non-zero. According to S. Clough et al. [9], the tunnelling of a methyl group manifests itself in a pair of weak sidebands to the main $\Delta m = \pm 1$ NMR transition. These sidebands appear at $\omega_L \pm \omega_t$. Since the sidebands involve simultaneous changes in spatial (tunnelling)

and spin states, they are forbidden. However, the dipole-dipole interaction between nuclei gives rise to some mixing of the pure A and E states with the result that the tunnelling sidebands become weakly allowed. Various experimental schemes have been devised in NMR to reveal these sidebands and enable methyl tunnelling to be investigated. Tunnelling frequencies are exponentially dependent on the barrier properties, so are very sensitive to the height of the hindering barrier.

When a nucleus with a magnetic moment exists in a solid state material it will undergo the following principal magnetic interactions [10]: -

The Zeeman interaction H_Z : - This interaction arises between the nuclear magnetic moment and the external magnetic field B_o for most of the nuclei with odd atomic number like 1H (with a nuclear spin quantum number $I=1/2$), this interaction will cause the Zeeman splitting $h\omega_o=\gamma hB_o$ of the energy levels. Hence the Hamiltonian may be expressed as (2),

$$H_z = -\gamma \hbar B_o I_z = -g_N \beta_N B_o I_z \quad (2)$$

where γ is the magnetogyric ratio (for 1H , $\gamma/2\pi=42.57$ MHz/Tesla), ω_o the associated Larmor frequency, g_N the nuclear g factor and β_N the Bohr magneton for the specific nucleus.

The Dipolar interaction H_D : - The interaction between magnetic moments is described by the dipole-dipole interaction H_D . For a pair of isolated spins in a solid with the same spin (I) and magnetogyric ratio γ_I , the interaction may be expressed as (3): -

$$H_D = H_{II} = \frac{\gamma_I^2 \hbar^2}{r_{II}^3} \vec{I} \cdot \vec{D} \cdot \vec{I} \quad (3)$$

while for a pair of different spins (\vec{I} and \vec{S}) with magnetogyric ratios(γ_I, γ_S), the interaction may be expressed as (4): -

$$H_D = H_{IS} = \frac{\gamma_I \gamma_S \hbar^2}{r_{IJ}^3} \vec{I} \cdot \hat{D} \cdot \vec{S} \quad (4)$$

where r_{IJ} is the internuclear distance and \hat{D} is the dipolar coupling tensor. For spin 1/2 nuclei with large magnetic moments (1H) and magnetogyric ratios, this interaction will be very strong, while it is independent of the applied field H_o and it falls off quickly ($1/r^3$) with the internuclear distance.

In solids the dipolar interaction is also dependent on the orientation of the inter-nuclear vector relative to the applied field, as shown by the tensor notation that describes the interaction.

The 1H - 1H dipolar interactions are strong and give rise to broad NMR absorption lines. These broad lines are characterized by the linewidth and the second moment $(\Delta H)^2$ of the spectra. The pulsed NMR experiment applied in our NMR investigations is sketched in Figure 1.3 where the M_z magnetization along z' is rotated by 90° into the x',y' plane by resonant radio frequency pulse ω_o applied along the x' direction in the rotating frame. After the pulse, M_z is aligned along the y' -axis and an FID is recorded which will be Fourier transformed to produce the NMR absorption spectrum.

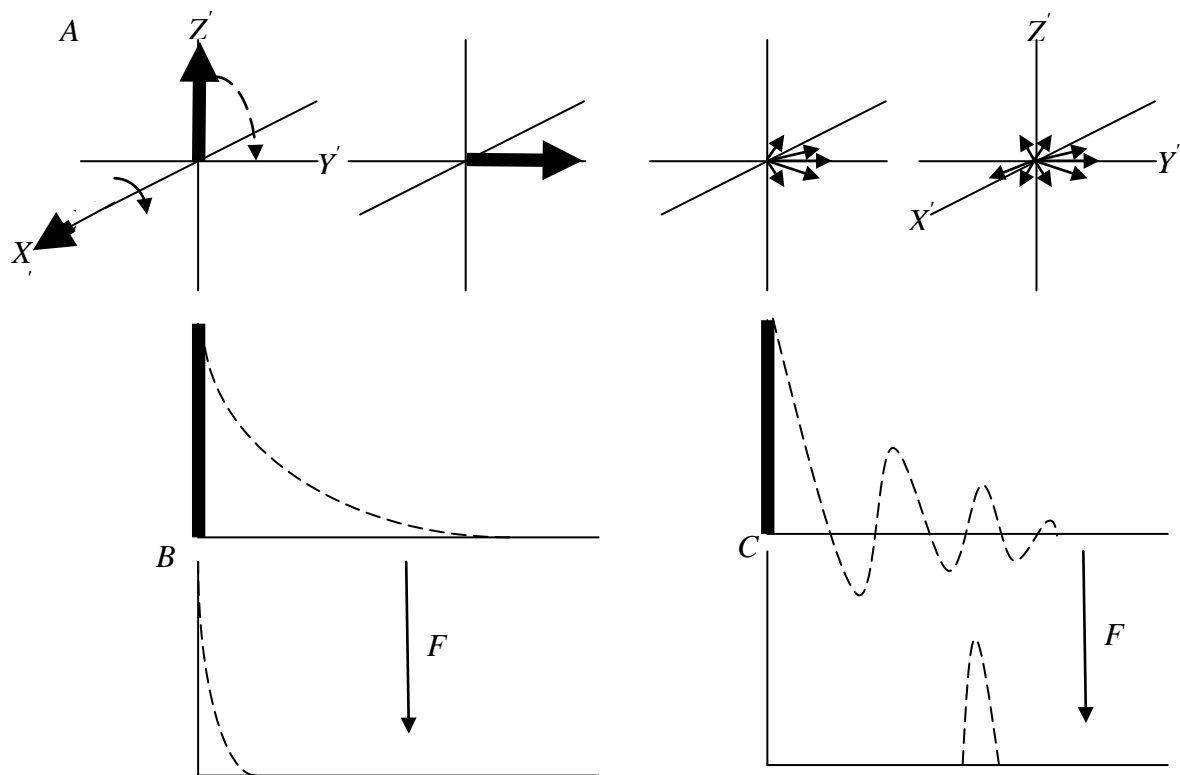


Figure 1.3: - In the rotating frame a simplified illustration of the pulse F/T sequence

including (A) the effect of an on-resonance rf pulse applied along the x' axis rotates the

magnetization by 90° . Then dephasing of the spins in the $x'y'$ plane gives rise to a

decaying time-dependent signal, the free-induction decay (FID). (B) and (C) The FID

that will be Fourier transformed to give the NMR absorption spectrum.

A pre-amplifier and radio receiver with a very short 'dead-time' must be employed to

catch the very fast decay as close to time zero as possible. This is important for

solid-state samples which have a broad absorption line and hence very fast decaying

FIDs.

Nuclear spin-lattice relaxation in solids is driven by magnetic fluctuations in the

molecular environment. These originate from the molecular motions that modulate the

dipolar interactions between nuclei. The nuclear spin lattice relaxation time (T_1) is

defined in equation (5) which describes the recovery of the nuclear magnetization following a disturbance away from equilibrium.

$$\frac{dM_z}{dt} = \frac{-(M_z - M_o)}{T_1} \quad (5)$$

The measurement of the spin-lattice relaxation time can be made by a two pulse NMR sequence. The first pulse disturbs the system from equilibrium, then following a delay during which the system can begin to recover towards equilibrium, a second resonance rf pulse is applied. (The sketch in Figure 1.4 shows the saturation-recovery sequence

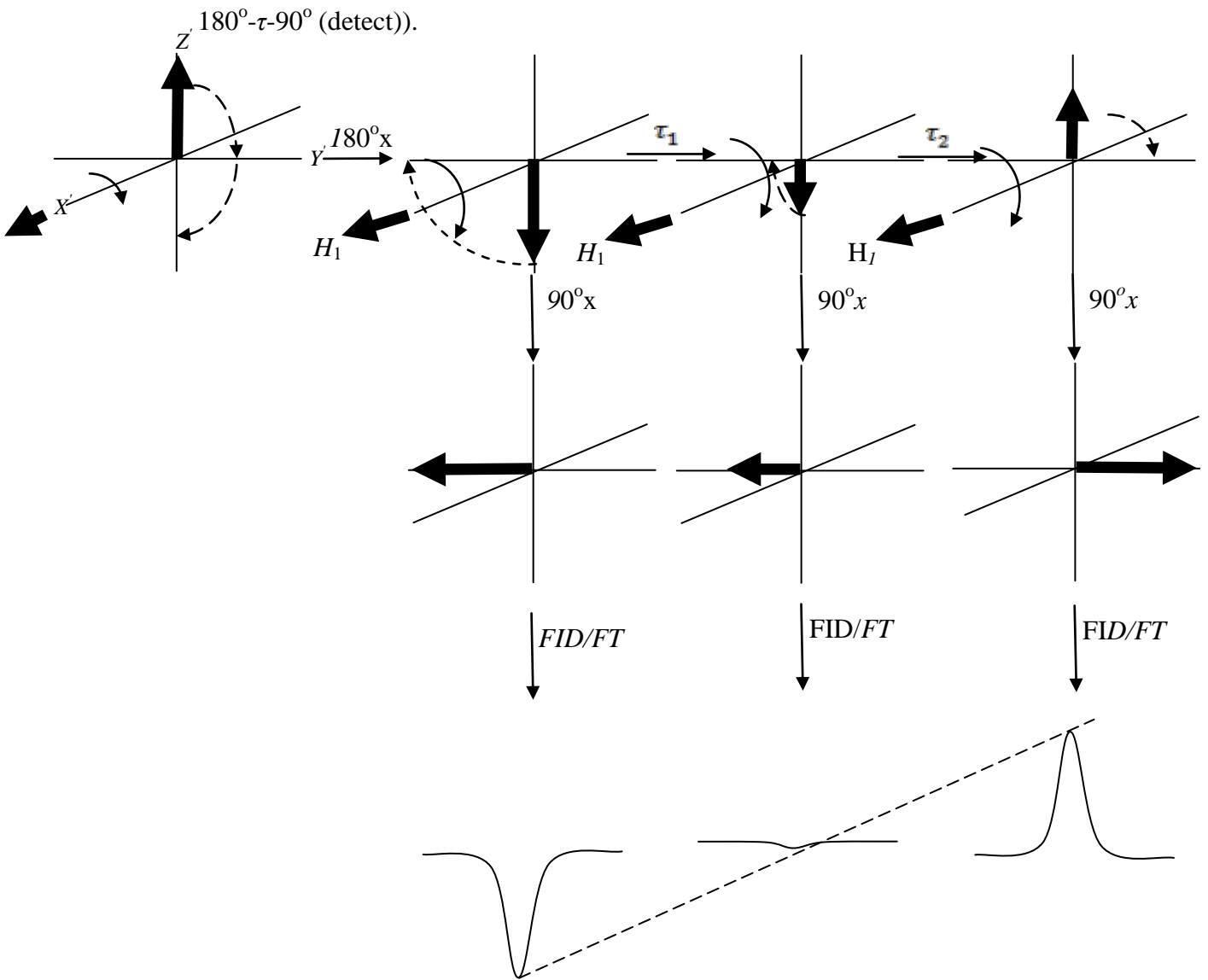


Figure 1.4: Sketch of the NMR pulse sequence used to measure the spin-lattice relaxation time (T_1) assessments using the $180^\circ\text{-}\tau\text{-}90^\circ$ succession.

In the 'high field' theory of Bloembergen, Purcell and Pound [21] a single molecular reorientation process characterized by a single temperature dependent correlation time τ_c drives the nuclear spin relaxation. The spin-lattice relaxation time is expressed as

(6)

$$\frac{1}{T_1} = C \left[\frac{\tau_c}{1 + \omega_o^2 \tau_c^2} + \frac{4\tau_c}{1 + 4\omega_o^2 \tau_c^2} \right] \quad (6)$$

Where C is a constant which represents the proton second moment parameter and ω_o is the nuclear precession frequency. The nuclear relaxation times can be employed to determine the energy barriers that characterize the dynamics, for CH_3 groups typically involving hopping between equivalents positions that characterize the potential wells of the 3-fold hindering potential.

An important aim is to devise experimental procedures to record the polarization of the methyl tunnelling system and, importantly, to manipulate this polarization in a prescribed manner. The ability to drive with rf irradiation the forbidden transitions between A and E species is demonstrated in the low-field dipole-dipole driven NMR experiments [11]. This enables us to control the populations of both nuclear Zeeman and methyl tunnelling levels with rf irradiation.

It is important to define some thermodynamic properties of the Zeeman and Tunnelling systems: we may characterize the polarizations in terms of the nuclear-Zeeman and methyl tunnelling reciprocal temperatures. At low temperature the CH_3 group is in the ground torsional state, with tunnelling splitting $\hbar\omega_t$ separating the rotational states A and E (where the latter is split into E_a and E_b). Hence the tunnelling temperature θ_t is defined by finding the ratio of the populations

$$\frac{p(E)}{p(A)} = \exp(-\beta_t \omega_t) \quad (7)$$

where $\beta_t = \hbar/k_B\theta_t$. The reciprocal Zeeman temperature $\theta_z^{-1} = k_B\beta_z/\hbar$ is similarly defined from the populations of the Zeeman levels. From the Curie Law we know the nuclear magnetization is proportional to θ_z^{-1} so this can be measured from the NMR signal following a resonant rf pulse.

The field switching rate of the field-cycling magnet is typically of order $10 T s^{-1}$, therefore with nuclear spin-lattice relaxation times of a few minutes, the evolution of the magnetization during the field switch is negligible. This means the recorded NMR behaviour is dependent only on the evolution periods in the experiment, for example when driving the forbidden transitions among *A* and *E* methyl states. All measurements of magnetization are recorded at the same field, corresponding to resonance between the rf frequency and the Larmor frequency. In low-field dipole-dipole driven NMR, the resultant spectrum contains a principle peak at the nuclear Larmor frequency ($\Delta m=\pm 1$) and another one at double of this frequency ($\Delta m=\pm 2$) but with smaller amplitude.

Additionally, pairs of sidebands accompany each of the $\Delta m=\pm 1$ and $\Delta m=\pm 2$ lines, offset by plus and minus the methyl tunnel frequency ω_t . A small peak is sometimes observed at the tunnel frequency, ω_t and is an unusual feature in representing a sideband of the $\Delta m=0$ spectrum [12]. The energy levels E_i of the tunnelling-Zeeman manifold can be specified by a pair of integers m_i, n_i (the magnetic and tunnelling quantum numbers) as follows:

$$E_i = \hbar\omega_z m_i + \hbar\omega_t n_i \quad (8)$$

The levels m_i takes values (3/2, 1/2, -1/2, -3/2) for *A* and it is ±1/2 for the doubly degenerate *E* levels (E_a and E_b), while n_i is assigned to be 1/2 for *E* and -1/2 for *A* states. Transitions driven by rf irradiation alter the populations of the levels; we can define the populations in terms of the inverse tunnelling and Zeeman temperatures β_t and β_z by the relation:

$$p_i = \beta_z m_i \omega_z + \beta_t n_i \omega_t \quad (9)$$

Alternatively, the inverse temperatures can be defined in terms of the populations by the relations:

$$\beta_z = \frac{\sum_i p_i m_i}{(\omega_z \sum m_i^2)} \quad (10)$$

$$\beta_t = \frac{\sum_i p_i n_i}{(\omega_t \sum_i n_i^2)} \quad (11)$$

The emphasis will be on transitions that involve conversion between spin-symmetry species for which $\Delta n = \pm 1$, while Δm may be 0, 1 or 2. In case of strong or persistent irradiation, the populations change until $p_i - p_j = 0$, when the transition is ‘saturated’, and the saturation condition applies when :-

$$\frac{\beta_z}{\beta_t} = -\frac{\omega_t \Delta n}{\omega_z \Delta m} \quad (12)$$

Chapter 2 Theoretical

2.1 Fundamental principles of tunnelling:-

When a fundamental particle is incident upon a potential barrier, there is a finite probability the particle will be transported across the barrier even if its kinetic energy is less than the barrier height. In practice this is most likely to occur when the de Broglie wavelength of the particle is comparable with the barrier width. This phenomenon, which has its origin in quantum mechanics, is a manifestation of the wave-like character of matter. It is known as quantum mechanical tunnelling and has been widely observed in many areas of physics, chemistry and biology providing a mechanism for the transport of atoms and molecules [13].

2.1.1 The de Broglie wavelength and the Heisenberg uncertainty principle:-

Initially suggested by de Broglie, the wave-particle duality of quantum particles of mass m and velocity v are characterized by a wavelength λ , is shown by the equation:

$$\lambda = \frac{\hbar}{mv} \quad (1)$$

where $\hbar = h/2\pi$ and h is Planck's constant ($h = 6.626 \times 10^{-34} Js$).

When λ is very small compared with the dimensions of the structures in which it exists, the dynamics of the particle may be described with adequate precision by Newtonian mechanics; this is because h is very small. The quantum tunnelling effects become evident when λ becomes comparable with the dimensions of its environment. It is for this reason that it is interesting, to compare the de Broglie wavelengths of particles with various masses. In chemical processes the barrier heights are typically 20 kJmol^{-1} (0.2 eV). As an illustration, we will consider particles having a similar kinetic energy E_k . Then equation (1) can be written in the form:

$$\lambda = h(2mE_k)^{-1/2} \quad (2)$$

The de Broglie wavelengths corresponding to the particles e^- , H , D , T , C and Br are shown in Table 2.1.

Particle	e^-	H	D	T	C	Br
m (amu)	1/1750	1	2	3	12	80
λ pm	26.90	0.64	0.45	0.36	0.18	0.07

Table 2.1: The de Broglie wavelength for particles with various masses and energy

0.2 eV.

Hence, the de Broglie wavelength of 1H is comparable with atomic distances and one may expect to observe quantum effects of such low-mass nuclei.

The Heisenberg uncertainty principle may alternatively be used to connect the tunnel phenomenon to the fundamental quantum principles. This states that it is impossible to simultaneously determine with perfect precision, the position of a particle along a stated axis, and its momentum along the same axis. The precision with which these two conjugate variables may be measured is determined by the quantity $h/2\pi$, where h is Planck's constant. Heisenberg's uncertainty principle is expressed as:

$$|\Delta x||\Delta p_x| = |\Delta x||m\Delta v_x| \approx \frac{h}{2\pi} \quad (3)$$

Because this description does not represent a specific position and momentum of the particle, but an uncertainty in such values, this is consistent with a wave-packet picture for the particle.

Deviations from Newtonian mechanics are particularly evident when the wave description of a particle is applied to bound molecular systems. This is manifest by

the existence of discrete energy levels, for example associated with vibrational energy. What also results from the Uncertainty Principle is the appearance of zero-point energy [14].

2.1.2 Coherent and incoherent tunnelling:-

It is suitable to identify two types of tunnelling process; incoherent and coherent tunnelling. Both are characterized by a tunnelling matrix element, J , which defines the permeability of a potential barrier. In the wave-packet description, J has its origin in the ‘overlap’ of the wavefunctions that characterize the eigenstates of two wells which are separated by the intervening barrier. Coherent tunnelling is related to the characteristic splitting that arises from symmetric and antisymmetric combinations of the above wave-packet states. In a time-dependent description, if a particle is placed in one well then it will oscillate between the wells with the frequency $2J$. Coherent tunnelling is only observed when the potential wells have equal depth. When the wells have non-equivalent depth defining an asymmetric potential energy surface, then incoherent tunnelling invariably arises. Here there is no coherent oscillation of particle probability between two wells, but the particle ‘decays’ through the barrier into the adjacent well.

2.2 NMR theory:-

At its simplest level, the topic of NMR arises when an externally applied magnetic field, $\overline{B_o}$, interacts with the magnetic moments of the nuclei in a material under investigation [15]. An NMR spectrometer is an instrument able to do the following:

1. Applying a magnetic field we can polarize the nuclear spins giving rise to a bulk magnetization of the sample that is aligned parallel to the field. This is longitudinal magnetization.

2. By applying a resonant rf pulse, the magnetization is rotated away from the field axis into the transverse plane. In so doing, transverse magnetization is created which in the presence of a receiver coil results in the generation of an NMR signal which can reveal the polarization state of the ensemble of nuclei that constitute the sample.
3. The Fourier transform of the NMR signal in the time domain gives rise to an NMR spectrum in the frequency domain. Where the resolution of the spectrometer is sufficiently good, splitting and shifts of individual lines in this spectrum reveal the interactions between the nuclei.

2.2.1 Relaxation Times:-

When the magnetic field $\overline{B_0}$ is first applied, the nuclear spins do not instantaneously align parallel with the field. The polarization and magnetization take a finite time to reach thermal equilibrium and this is the process of ‘spin-lattice relaxation’. The time taken is characterized by the ‘spin-lattice relaxation time’, T_1 . This can be a relatively slow process because there must be an exchange of energy between the nuclear spin system and its environment, commonly referred to as the ‘lattice’.

A sample outside of a magnetic field has no Zeeman splitting and if this is for a spin-1/2 system, then the two energy levels have equal populations. When the magnetic field is applied and the levels split, then for an instant the system is characterized by an infinite temperature because the levels are equally populated, however, interactions mediated by time-dependent magnetic interactions give rise to transitions between the magnetic sub-levels and the Zeeman system cools. This longitudinal relaxation gives rise to a growth of magnetization and the process is invariably exponential in character as the system recovers towards its equilibrium configuration.

The rate of change of longitudinal magnetisation M_z is given by:

$$\left(\frac{dM_z}{dt} \right) = \frac{M_o - M_z}{T_1} \quad (4)$$

Since magnetization is a vector, there is also a relaxation process governing any transverse magnetization of the sample. The corresponding relaxation process is characterized by the ‘transverse’ or ‘spin-spin’ relaxation time T_2 so, given the equilibrium transverse polarization is zero, we may write,

$$\left(\frac{dM_{xy}}{dt} \right) = - \frac{M_{xy}}{T_2} \quad (5)$$

2.2.2 Spin-Lattice relaxometry:-

Stimulated absorption and emission mediates the spin-lattice relaxation between the various nuclear magnetic energy states. The process is driven by time-dependent magnetic interactions arising from the relative motion of atomic nuclei. Therefore, nuclear spin relaxation can provide a signature of the molecular dynamic processes in the material. Where quantum tunnelling processes are important it transpires that making magnetic field dependence studies of the relaxation and polarization of the sample has particular benefits. This is the general field of ‘spin-lattice relaxometry’ and in the experiments to be discussed in this thesis; the magnetic field dependence is determined by utilizing the technique of ‘magnetic field cycling NMR’.

An example of field cycling is shown in Fig 2.1, where the field is instantaneously switched on at time t_{on} . With these field conditions, the solution of the differential equation (4) may be written as:

$$M_z(t) = M_{eq}^{nuc} \left(1 - \exp - \frac{(t - t_{on})}{T_1} \right) \quad (6)$$

The exponential recovery towards equilibrium is shown in Fig 2.1. Therefore the spin-lattice (longitudinal) relaxation time may be determined by plotting the longitudinal magnetization as a function of time after a disturbance to the system away

from equilibrium. In Figure 2.2, the magnetization behaviour is shown when the magnetic field is abruptly switched off, with the following solution of the Bloch equation (4):

$$M_z(t) = M_{eq}^{nuc} \left(1 - \exp - \frac{(t - t_{off})}{T_1} \right) \quad (7)$$

The molecular motions and temperature determine the spin-lattice relaxation time and typically T_1 is of the order milliseconds to tens or hundreds of seconds, although at low temperature it can be a number of days or even months [16].

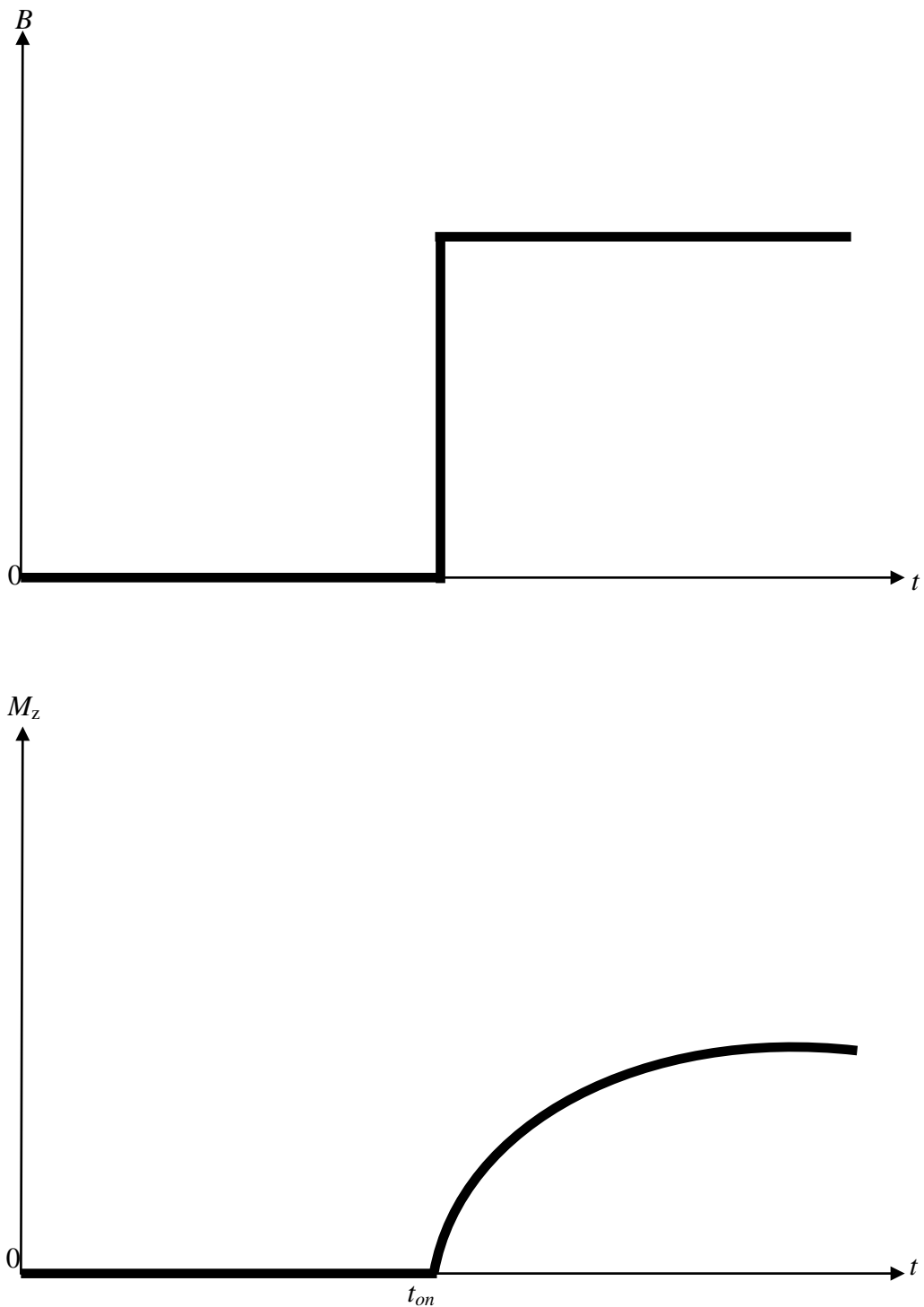


Figure 2.1: The gradual increase, subsequent to switching the magnetic region on, of longitudinal spin magnetization (for periods $t \geq t_{on}$).

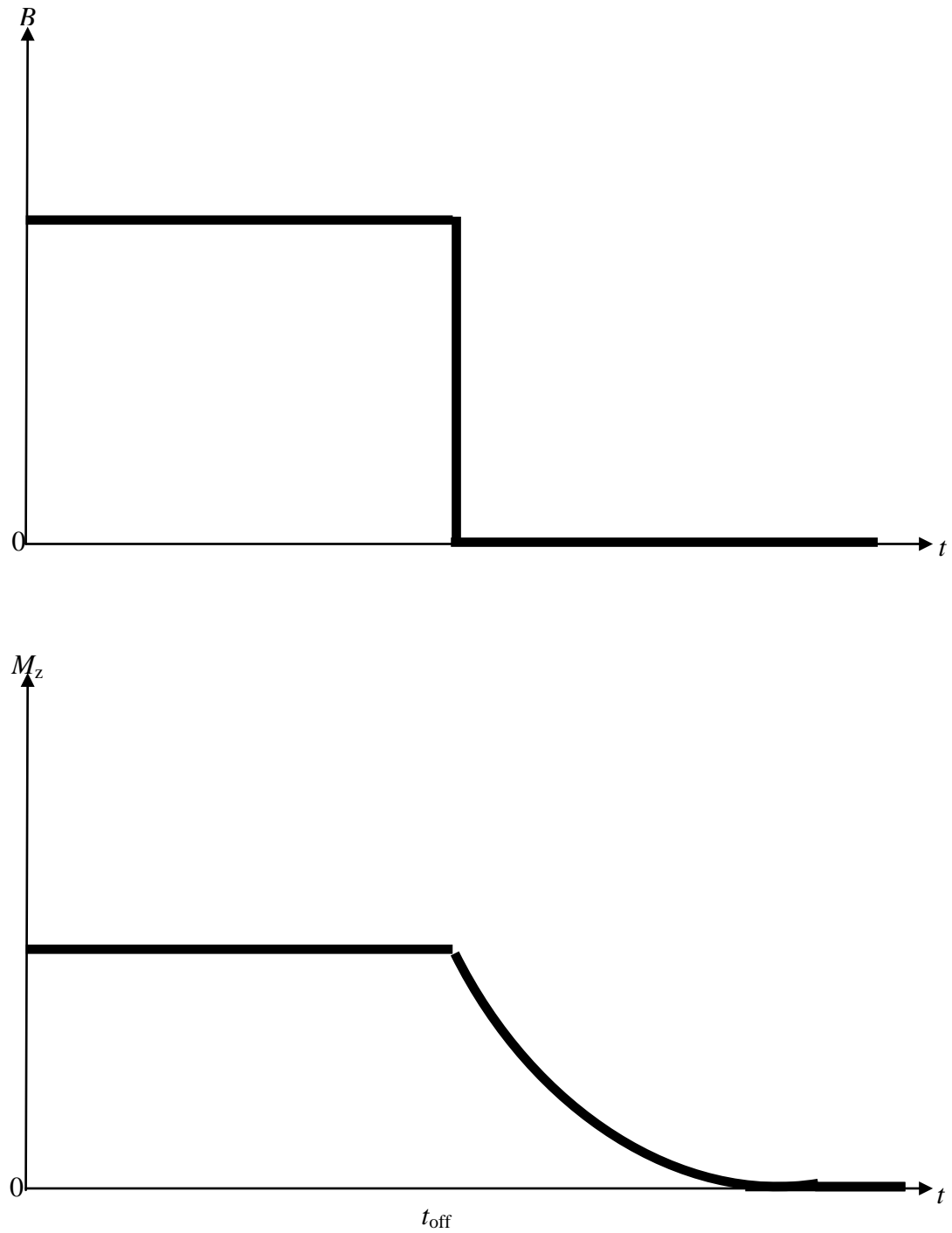


Figure 2.2: The gradual decrease, subsequent to switching the magnetic region off, of longitudinal spin magnetization (for periods $t \geq t_{off}$).

The spin-lattice relaxation process is driven by molecular motion, which induces a modulation in the magnetic interactions experienced by the nuclei. The inverse spin-lattice relaxation time for powdered samples containing homonuclear spins may

be modelled as a sum of two Lorentzian lines $L(\omega, \tau_c) = \tau_c/(1+\omega^2\tau_c^2)$ as in the following equation, [17,18]:

$$T_1^{-1} = C_D \frac{4a}{(1+a)^2} [L(\omega, \tau_c) + 4L(2\omega, \tau_c)] \quad (8)$$

Therefore, T_1 samples the spectral density at the Larmor frequency ω , and double this frequency where $a/(1+a)^2$ is a temperature dependent term and C_D is the dipolar constant.

2.2.3 Applications of measuring relaxation times:-

In a solid the molecular dynamics induce a relative motion between the nuclear spins which constitute the molecule. Therefore there is a modulation of the inter-molecular and intra-molecular dipolar interactions and this drives the spin-lattice relaxation.

Temperature and magnetic field dependence measurements of T_1 enable the molecular dynamics processes to be determined and the theoretical framework will be outlined.

2.3 Hydrogen bond quantum tunnelling:-

The dynamics of the hydrogen atoms in the hydrogen bond are characterized by an asymmetric double well potential where the energy asymmetry of the two wells is A as shown in Fig.1.1. While the displacement of a hydrogen atom from its equilibrium position must be accompanied by small displacements of the heavy atom framework, we shall assume that a single coordinate is sufficient to describe the molecular rearrangement between the two of tautomeric forms labelled 1 and 2. We will suppose that the motions at elevated temperatures are Arrhenius, according to Skinner and Trommsdorff [4], and that at low temperatures the dynamics are dominated by phonon assisted tunnelling [19].

2.3.1 NMR spin-lattice relaxometry (homonuclear case):-

Using the second order tensors $A^{(m)}$ and $F^{(m)}$ relating to the spin and spatial variables respectively, with m indicating the change in spin quantum number, we may write the dipolar Hamiltonian as:

$$H_{dd} = \sum_{m=-2}^{m=2} A^{(m)} F^{(m)} \quad (9)$$

The inverse spin-lattice relaxation time at the magnetic field B_o , between homonuclear spins of spin I is expressed in the weak collision regime where $\tau_c \ll T_2$ by the following

$$\frac{1}{T_1} = \frac{3}{2} \gamma^4 \hbar^2 I(I+1) [J^1(\omega_o) + J^2(2\omega_o)] \quad (10)$$

Where $\omega_o = \gamma B_o$ is the Larmor frequency of nuclei with magnetogyric ratio γ . The spectral density function $J^m(\omega)$ is the Fourier transform of the correlation function of the spatial part of the dipolar interaction.

$$J^m(\omega) = \int_{-\infty}^{\infty} \langle F^{(m)*}(t+\tau) F^m(t) \rangle \exp(i\omega\tau) d\tau \quad (11)$$

This represents the power available in the spectrum of random fluctuations to drive transitions in spin-state. In Eqn. 10, the single and double-spin spectral density terms arise from the one-spin and two-spin operators of H_{dd} , which are represented time dependent by the proton motion. Applying a two-site jump model p to a dipolar pair of hydrogen atoms, enables us to write the correlation function as a sum of four terms:

$$\langle F^{(m)*}(t+\tau) F^m(t) \rangle = \sum_{\alpha, \beta=L, R} \left[F_{\alpha}^{(m)*} F_{\beta}^{(m)} \right] X p(\alpha, t+\tau | \beta, t) p(\beta, t) \quad (12)$$

Where $F_{\alpha}^{(m)}$ is the spatial part of the dipolar interaction when the system occupies site α .

The following relation for the spectral density results when the correlation functions are assumed to be exponential decays:

$$J^m(\omega) = \frac{\alpha}{(1+\alpha)^2} \left\{ \left[F_L^{(m)*} F_L^{(m)} \right] - \left[F_L^{(m)*} F_R^{(m)} \right] + \left[F_R^{(m)*} F_R^{(m)} \right] - \left[F_R^{(m)*} F_L^{(m)} \right] \right\} \frac{2\tau_c}{1 + (\omega\tau_c)^2} \quad (13)$$

Here we draw special attention to several characteristics:

1. The random hopping mechanism leads to exponential correlation functions and as a result, Lorentzian line shapes $J^m(\omega)$ arise. The latter is a spectrum comprising a peak with half-width at half-maximum being equal to the inverse correlation time.
2. The amplitude of $J^m(\omega)$ has a temperature dependent term, $\frac{\alpha}{(1+\alpha)^2}$, which derives from the Boltzmann population parameters and the energy asymmetry.
3. The quantities in square brackets also determine the amplitude of the spectral density, describing the depth of modulation of the dipolar interaction arising from the proton dynamics which in turn is specified by the geometry of the interacting spins.

The following equation for the spin-lattice relaxation time of a powdered sample is obtained by replacing the calculated spectral density relations in Equation (13) into Equation (8):

$$T_1^{-1}(\omega) = C_D \frac{4\alpha}{(1+\alpha)^2} \left(\frac{\tau_c}{1 + (\omega\tau_c)^2} + \frac{4\tau_c}{1 + (2\omega\tau_c)^2} \right) \quad (14)$$

The dipolar constant, C_D , is determined by the molecular geometry and Equation (14) provides insight into the dynamical spectrum associated with the proton transfer in the hydrogen bonds [20].

2.3.2 NMR relaxometry:-

It is evident that Equation (8) provides a direct mapping between T_1^{-1} and the spectral density and, in more refined form, T_1^{-1} to the correlation period for proton transfer. So there are three strategies for analyzing T_1 and determining the proton transfer dynamics from it.

1. Model the temperature dependence of the correlation time in terms of a theoretical framework and then a best fit to the T_1 data by least squares adjustment of any parameters incorporated in the theory. The latter will describe the physical characteristics of the potential energy surface, the coupling to phonons and the magnetic interactions.
2. Numerical inversion of Equation (14) so that the correlation time may be concluded directly from a table of T_1 values as a function of temperature.
3. Plot the spectral density directly from the frequency or field dependence of T_1^{-1} , Equation (8) [20].

2.3.3 Models incorporating tunnelling:-

A characteristic of incoherent tunnelling is the appearance of a plateau region in the low temperature behaviour of the inverse correlation time. Non-Arrhenius behaviour is observed and at low temperature the dynamics are substantially faster than would be permitted by classical barrier hopping. In 1988 Skinner and Trommsdorff [4], developed a phenomenological theory describing the proton transfer dynamics across both quantum tunnelling and classical hopping regimes and the intermediate region in between. Here we will outline its essential features.

Proton transfer takes place in the asymmetric double well potential and finite tunnelling matrix elements provide a pathway for barrier crossing. Due to the energy asymmetry the process is incoherent and described by accidental hops. In the tunnelling regime we

identify proton transfer rates K_{LR} and K_{RL} describing left-to-right (or upward) motion and right-to-left (or downward) motion. The net correlation time is determined by a sum of the two rate constants:

$$\tau_c = (K_{LR} + K_{RL})^{-1} \quad (15)$$

The ‘up’ rate K_{LR} is mediated by one-phonon absorption while the ‘down’ rate K_{RL} arises from stimulated and spontaneous emission and is non-zero at 0 K. Detailed balance applies to the proton transfer process so that

$$\frac{K_{RL}}{K_{LR}} = \frac{P(L)}{P(R)} = \alpha \quad (16)$$

And Skinner and Trommsdorff derived the following for the low temperature phonon-assisted tunnelling rate:

$$(\tau_c^{-1})_L = K_o \coth\left(\frac{A}{2k_B T}\right) \quad (17)$$

Where K_o is the rate of single phonon emission at 0 K. It is given by:

$$K_o = \frac{3\pi}{2} \left(\frac{\kappa J}{\hbar \omega_D} \right) \frac{A}{\hbar} \quad (18)$$

This is valid when A is smaller than the Debye frequency (ω_D), The dimensionless constant, κ , describes the coupling to the phonons. Here J is the effective tunnelling matrix element.

Additional barrier crossing pathways become available at higher temperatures as excited states become populated. At sufficiently high temperature these combine to give an Arrhenius expression

$$(\tau_c^{-1})_H = \tau_o^{-1} \exp\left(\frac{-\Delta E_{act}}{k_B T}\right) \quad (19)$$

where ΔE_{act} is the activation energy and it is commonly observed that this is smaller than the barrier height since barrier penetration occurs via excited states and activation over the top of the barrier is not required.

To obtain the inverse correlation time for proton transfer Skinner and Trommsdorff combined the quantum tunnelling and Arrhenius mechanisms in low and high temperatures as follows:

$$\tau_c^{-1} = (\tau_c^{-1})_L + (\tau_c^{-1})_H \quad (20)$$

To model the intermediate regime between tunnelling and barrier hopping, Skinner and Trommsdorff [4] introduced an intermediate term to include excited state tunnelling explicitly, modifying the proton transfer rate to the following,

$$\tau_c^{-1} = K_o \coth\left(\frac{A}{2k_B T}\right) + \tau_{exc}^{-1} \exp\left(\frac{-\Delta E_{exc}}{k_B T}\right) + \tau_o^{-1} \exp\left(\frac{-\Delta E_{act}}{k_B T}\right) \quad (21)$$

Where τ_{exc}^{-1} is related to the permeability of the barrier in an excited state that has energy ΔE_{exc} .

2.4 Tunnelling properties associated with methyl group rotation:-

A methyl group experiences a three-fold symmetrical barrier to rotation. Within a single well the CH_3 group can undergo torsional oscillation and we identify a ladder of torsional states. For adjacent wells, wavefunction overlap of these torsional states gives rise to a doubling of those states and the splitting is a tunnelling splitting or exchange splitting which is quantum mechanical in origin with no classical analogue. The existence of this tunnelling splitting provides a mechanism for the methyl group to rotate through $2\pi/3$ even though it may have insufficient energy to overcome the potential barrier. In a particular torsional state the tunnel split levels are labelled A and E according to the irreducible representations of the C_3 symmetry group. Each

E-species is a pair of degenerate states labelled E_a and E_b . In the ground torsional state the state with *A*-symmetry is lowest in energy, but in the first excited state it is the *E*-state which is lowest in energy. The order of the *A* and *E* states alternates up the ladder of torsional levels and the tunnelling splitting becomes successively larger due to the barrier width declining with increasing energy.

The Pauli Exclusion Principle (PEP) must apply to the wavefunction of the methyl group, and since the three protons of CH_3 are all fermions with spin $1/2$ the complete wavefunction of the methyl group must be antisymmetrical with respect to exchange of two protons. The complete wavefunction can be written

$$\Psi = \psi_e \psi_{vib} \psi_R \psi_S$$

At the temperatures considered the electronic and vibrational wavefunctions ψ_e and ψ_{vib} are in their ground state and therefore have *A*-symmetry and need no longer be considered. Therefore, in considering the antisymmetry properties of the complete wavefunction we only need to consider the product of the rotational and spin wavefunctions, ψ_R and ψ_S . The nuclear spin and rotational properties of a methyl group are therefore mutually mixed together. This gives rise to nuclear spin isomerism and nuclear spin-symmetry species.

2.4.1 Spin-symmetry species:-

Applying the antisymmetry principle to the methyl group relating to an exchange of a pair of protons, it is concluded that the total wavefunction must have *A*-symmetry. The rotational wavefunction is concerned only with spatial variable whereas the spin wavefunction contains only spin variables. Therefore the product of space $|\psi_R\rangle$ and spin $|\psi_S\rangle$ wavefunctions must have an *A*-symmetry. Consequently the only allowed symmetry combinations turn out to be $|\psi_R^A\rangle|\psi_S^A\rangle$, $|\psi_R^{E_a}\rangle|\psi_S^{E_b}\rangle$ and $|\psi_R^{E_b}\rangle|\psi_S^{E_a}\rangle$. Closer

inspection of the spin states leads to the conclusion the A-species is a nuclear spin quartet of spin-3/2 while the E-species is a nuclear spin doublet of spin 1/2. See Figure 2.3 [12].

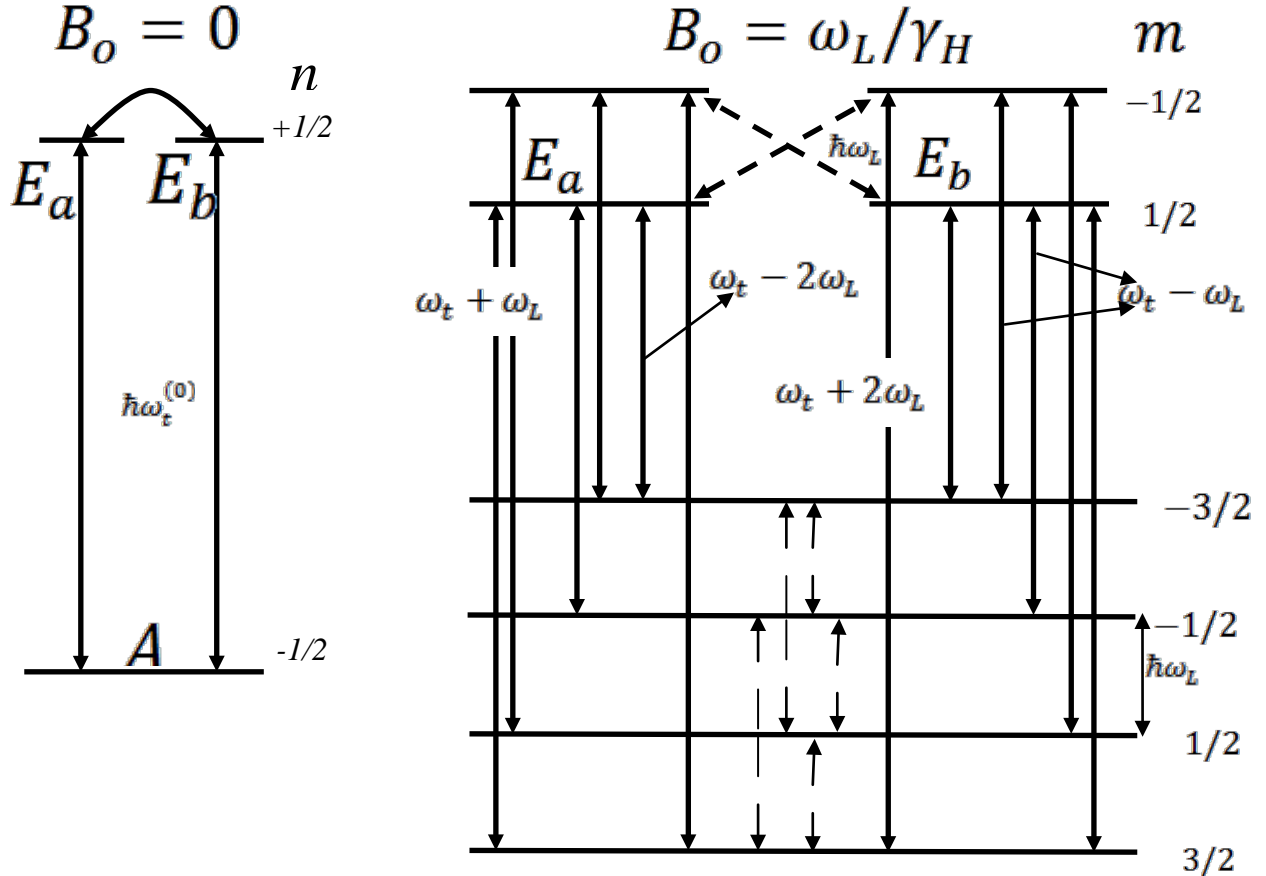


Figure 2.3: The effect of applied magnetic field B_o on the energy levels of the lowest energy torsional state of a methyl group showing the Zeeman and tunnelling states splitting of a methyl group. The nuclear spin E_a - and E_b - states are nuclear spin doublets with $m_l = 1/2$, and the A-types are nuclear spin quartets with $m_l = 3/2$. The non-zero matrix elements of the intra-molecular dipolar Hamiltonian and the corresponding frequencies are shown and the tunnelling sideband transitions are identified, where ω_L and ω_t are the ^1H Larmor and the methyl tunnelling frequencies respectively.

2.4.2 The thermodynamics of the methyl group:-

Depending on the barrier height, excitation energies between adjacent torsional states are of the order 10-30 meV. There is a fast phonon relaxation driven by the modulation

of the rotational potential amplitude within each manifold of *A or E* rotational states.

Consequently, torsional states are usually in thermal equilibrium with the lattice.

However, transitions between *A and E* states require a time-dependent magnetic interaction coupling space and spin variables and *A-E* conversion is spin-restricted. The probability of *A-E* transitions is considerably lower than *A-A and E-E* transitions. At low temperatures only the lowest energy torsional state is occupied, because $k_B T$ is small compared with the torsional splitting. The populations of the ground tunnelling states are slow to respond to changes in the lattice temperature, due to the inefficiency of *A-E* conversion. This means that the tunnelling energy reservoir can be thermally isolated from the lattice. It is characterized by a tunnelling temperature that is determined by the populations of the *A- and E-* states and by a characteristic frequency, the tunnelling frequency, which is determined by splitting of the ground torsional state. A reservoir model is useful to understanding the quantum dynamical behaviour of methyl groups. In Figure 2.4, we identify thermal energy reservoirs associated with tunnelling, Zeeman and dipolar energies. It can be useful in explaining the magnetic resonance behaviour of methyl groups. Due to the inefficiency of *A-E* conversion it is common for the tunnelling energy reservoir to have a temperature that is greater than the lattice. This means the tunnel reservoir can act as a source of monochromatic energy, $\hbar\omega_t$. In this thesis we shall explore some magnetic resonance experiments that give rise to some interesting spin polarization effects that exploit these quantum states [12].

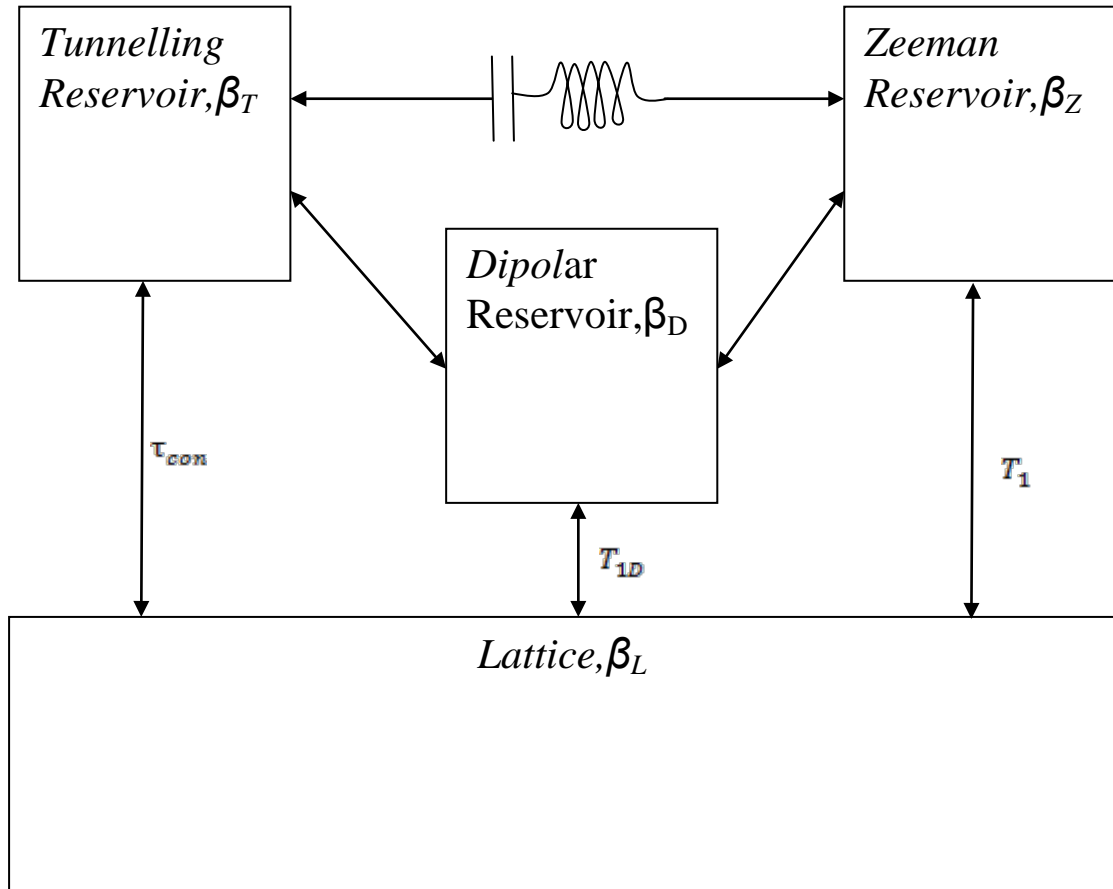


Figure 2.4: Using the thermal reservoirs model relating to the Zeeman, tunnelling and dipolar energies (with reciprocal temperature β), a range of NMR experiments on methyl groups may be explained. The tunnelling energy reservoir is only weakly coupled to the lattice and the $A-E$ conversion period, τ_{con} , can be very long at low temperature. Level crossings between Zeeman and tunnelling states can arise which permit a resonant transfer of energy leading to so-called ‘tunnel resonances’ in NMR.

2.4.3 Manifestations of methyl group reorientation in nuclear magnetic resonance:-

When the spin Hamiltonian has time-dependence, there will be an effect on both the nuclear magnetic resonance spectrum and the nuclear spin relaxation. In the solid state, it is the nuclear-nuclear dipole interaction that communicates the rotation of the CH_3 group. As the methyl group rotates, the nuclear-nuclear dipole-dipole interaction

between the protons of spins is modulated. The dipolar Hamiltonian has the following form

$$\widehat{H}_{dd} = \frac{\gamma_1 \gamma_2 \hbar^2}{r^3} \{A + B + C + D + E + F\} \left(\frac{\mu_0}{4\pi} \right) \quad (22)$$

Where the magnetogyric ratios of the two interacting nuclei are γ_1 and γ_2 .

Using the spherical polar coordinates (r, θ, ϕ) to describe the inter-nuclear vector, and if the supplied magnetic region is in the z-direction, then:

$$A = -I_z^{(1)} I_z^{(2)} (3\cos^2\theta - 1) \quad (23)$$

$$B = \frac{1}{4} [I_+^{(1)} I_-^{(2)} + I_-^{(1)} I_+^{(2)}] (3\cos^2\theta - 1) \quad (24)$$

$$C = -\frac{3}{2} [I_z^{(1)} I_+^{(2)} + I_+^{(1)} I_z^{(2)}] \sin\theta \cos\theta \exp(-i\phi) \quad (25)$$

$$D = -\frac{3}{2} [I_z^{(1)} I_-^{(2)} + I_-^{(1)} I_z^{(2)}] \sin\theta \cos\theta \exp(i\phi) \quad (26)$$

$$E = -\frac{3}{4} I_+^{(1)} I_+^{(2)} \sin^2\theta \exp(-2i\phi) \quad (27)$$

$$F = -\frac{3}{4} I_-^{(1)} I_-^{(2)} \sin^2\theta \exp(2i\phi) \quad (28)$$

Clearly the terms in this Hamiltonian are products of space and spin variables. Once provided time dependent by the CH_3 rotation, the various terms in Eqn. (22) have the ability to flip a nuclear spin at the same time as a change in tunnelling state. It is an efficient intermediary for reporting on the tunnelling dynamics of the methyl group, because \widehat{H}_{dd} may drive $A-E$ tunnelling transitions in addition to the $E-E$ rotational transitions. In methyl tunnelling investigations, experimental procedures can be devised to reveal the spectral characteristics associated with $A-E$ transitions, exploiting the dipole-dipole interaction. We identify inter-molecular and intra-molecular dipole-dipole interactions which have different effects. Intramolecular interactions occur between protons on the same CH_3 group whereas inter-molecular interactions are

between a methyl proton and another proton in a different part of the molecule or on an adjacent molecule. Non-zero matrix elements of the intra-molecular terms are illustrated by solid arrows in Fig. 2.3. These can involve transitions that interchange A and E. These have transition frequencies $|\omega_t \pm \omega_L|$; $|\omega_t \pm 2\omega_L|$, where $\omega_L = 2\pi\nu_L$ is the proton Larmor frequency. In contrast, illustrated with broken arrows in Figure 2.3 are non-zero matrix elements of the intermolecular interaction. These have frequencies, ω_L and $2\omega_L$.

Some practical methods exploit the existence of spectral features in the frequency response of nuclear magnetization, to show the tunnelling frequency and the quantum dynamics of methyl groups. At low temperature we find that in NMR spectra the coherent tunnelling dynamics of the methyl group gives rise to distinguishable tunnelling sidebands. These are symmetrically placed on either side of the $\Delta m = \pm 1$ and $\Delta m = \pm 2$ absorption lines, offset by the tunnelling frequency. These are A-E transitions that become weakly allowed due to mixing of the A and E states by the dipolar interactions.

Features associated with tunnelling also occur in the spin-lattice relaxation spectrum. The relaxation rate, T_1^{-1} , can be determined from an analysis of the various transition probabilities within the manifold of tunnelling-magnetic levels, Fig. 2.3. The following relation was acquired by Haupt:

$$T_1^{-1} = C_{AE} \sum_{n=1}^2 \left(\frac{n^2 \tau_c}{1 + (\omega_t + n\omega_L)^2 \tau_c^2} + \frac{n^2 \tau_c}{1 + (\omega_t - n\omega_L)^2 \tau_c^2} \right) + C_{EE} \sum_{n=1}^2 \frac{n^2 \tau_c}{1 + n\omega_L^2 \tau_c^2} \quad (29)$$

The first term on the right hand side of Equation (29), comes from the modulation of the intramolecular dipolar interaction, with dipolar constant C_{AE} . This term includes an A-E

change in the tunnelling state of the methyl group. Consequently, the tunnelling frequency is introduced into the spectral density. The second term on the right hand side is closely related to the conventional spectral density parameters that appear in the familiar BPP formalism [21]. This arises from the intermolecular dipolar interaction, with dipolar constant C_{EE} [21]. In deriving this formula, Equation (29), it was assumed that the incoherent rotational dynamics are modelled by stochastic hopping. This gives rise to Lorentzian lineshapes in the spectral density because the correlations functions are exponential decays with correlation time τ_c .

In designing magnetic resonance experiments to investigate tunnelling dynamics it is highly advantageous to develop techniques that enable the spectral density to be recorded as a function of frequency [12]. Invariably this requires some form of magnetic field cycling.

2.5-Methyl ethyl ketone and Acetophenone (low field experiments)

2.5.1. Transitions that involve an A to E change in rotational state: - These require a simultaneous flips in spatial and spin eigenfunctions, therefore to be observable they can only be mediated by interactions that connect space and spin variables. One such interaction is the nuclear-nuclear dipole-dipole interaction which induces a partial mixing of A and E states. As a result A to E transitions become weakly allowed and in favourable cases where the tunnelling frequency is small, give rise to weak tunnelling sidebands on the NMR spectrum. These are offset from the centre of the main NMR line by the tunnelling frequency and this is the situation at high field. However, at low magnetic field where the Zeeman splitting is comparable with the tunnelling splitting and the dipolar interaction then urge the appearing of the A-E sidebands with significantly greater intensity because it mixing A and E states. This may particularly be the case close to so-called ‘level-crossings’ where the applied magnetic field is chosen

such that *A and E* states have very similar energy and hence undergo significant mixing. These characteristics are exploited in the experiments conducted as part of this thesis. Field-cycling pulsed NMR experiments are devised to enable the tunnelling and Zeeman states to evolve in low magnetic field, giving rise to transfers in tunnelling and Zeeman polarization.

Methyl tunnelling transitions from one quantum state to another appear with angular frequencies of $(\omega_t + \omega_L)$, $(\omega_t - \omega_L)$, $(\omega_t + 2\omega_L)$ and $(\omega_t - 2\omega_L)$ (unbroken arrows in Fig.2.3). These are strongly enhanced when the tunnelling and Zeeman reservoirs are coupled in the presence of appropriate rf irradiation [22].

Low-field dipole-dipole driven NMR is an established technique for investigating *A-E* tunnelling transitions and there are several sideband peaks that reveal these tunnelling changes with splittings:- $\hbar(\omega_t + \omega_L)$, $\hbar(\omega_t - \omega_L)$, $\hbar(\omega_t + 2\omega_L)$ and $\hbar(\omega_t - 2\omega_L)$ as shown in (Fig.2.3). These are assigned the labels *a+*, *a-*, *b+* and *b-* respectively.

Previous work has shown that the transition probability is not the only issue when considering the strength of a tunnelling sideband. Sometimes the intensity of a sideband is very small because the populations of the states connected by the transition are easily saturated; meaning any changes in Zeeman or tunnelling polarization can be very small [22]. Therefore it is appropriate to review the changes in populations of the Zeeman-tunnelling manifold of levels in the presence of resonant rf irradiation, as originally shown by Clough et al [9].

Populations of the *A and E* states ($P(A)$ and $P(E)$) are characterized by the tunnelling temperature $\theta_t = \hbar/(k_B\beta_t)$ [22],

$$\frac{P(E)}{P(A)} = \exp(-\beta_t \omega_t) \approx (1 - \beta_t \omega_t) \quad (30)$$

A quantum number defining the tunnelling states can be assigned as follows: $n=1/2$ for the E states and $n=-1/2$ for the A states. Therefore Eqn.30 can be expressed, after eliminating constants, as [22]:

$$P_n = -n\beta_t \omega_t \quad (31)$$

Similarly the populations of the Zeeman states is given by [22],

$$P_m = -m_l \beta_z \omega_z \quad (32)$$

where the nuclear spin magnetic number is m_l , the Larmor frequency is ω_z and the Zeeman temperature is θ_z , so that $\beta_z = h/k_B \theta_z$. The populations in the model are calculated, by supposing the quantum number $m_l = \pm(1/2)$ and $\pm(3/2)$ for the A species and $m_l = \pm(1/2)$ for the E species, so that:

$$P_{nm} = -n\beta_t \omega_t - m_l \beta_z \omega_z \quad (33)$$

For instance, the population (P_{nm}) of the state with E species $n=+1/2$ and a Zeeman state ($m_l=+1/2$) is $P_{+1/2+1/2}$ [22]. So β_z and β_t can be written as,

$$\beta_z = -\frac{\sum_{n,m_l} m_l P_{nm}}{\omega_z \sum_m m_l^2} \quad (34)$$

$$\beta_t = -\frac{\sum_{n,m_l} n P_{nm}}{\omega_t \sum_n n^2} \quad (35)$$

If a particular transition from one quantum state (n, m_l) to another (n', m'_l) is driven, the populations of the two states will change until they are equal. This is the state of saturation given by,

$$P_{nm} = P_{n'm'} \quad (36)$$

We get by substituting Equation 33 in Equation 36,

$$\frac{\beta_z}{\beta_t} = -\frac{\omega_t \Delta n}{\omega_z \Delta m} \quad (37)$$

where

$$\Delta n = n - \dot{n} \text{ and } \Delta m = m_l - \dot{m}_l \quad [22].$$

The four solid lines show the saturation conditions for the four sideband transitions like:

$$(\omega_t + \omega_L), (\omega_t - \omega_L), (\omega_t + 2\omega_L) \text{ and } (\omega_t - 2\omega_L).$$

Additionally, the saturation condition for the $A-E$ transitions with $\Delta n = 1$ and $\Delta m = 0$ is shown with the broken line coincident with the y -axis. This is forbidden at high field but may be allowed at low field. The evolution of the system under rf irradiation may be described by the point (β_t, β_z) in the $\beta_t - \beta_z$ plane and the direction of movement is determined by the derivative $(d\beta_z/d\beta_t)$ [22].

Consequently, the net change in populations should be zero for the transition from one quantum state (n, m_l) to another (\tilde{n}, \tilde{m}_l) ,

$$\Delta P_{nm} = -\Delta P_{\tilde{n}\tilde{m}} \quad (38)$$

We get by substituting Equation 38 in Equations 34 and 35,

$$\Delta \beta_z = -\frac{\Delta m \Delta P_{nm}}{\omega_z \sum_{m_l} m_l^2} \quad (39)$$

$$\Delta \beta_t = -\frac{\Delta n \Delta P_{nm}}{\omega_t \sum_n n^2} \quad (40)$$

Hence in the $\beta_t - \beta_z$ plane, the derivative is given by,

$$\frac{d\beta_z}{d\beta_t} = \frac{\omega_t \Delta m \sum_n n^2}{\omega_z \Delta n \sum_{m_l} m_l^2} \quad (41)$$

The trajectory in the $\beta_t - \beta_z$ plane is obtained by finding the integral of Equation 41,

$$\frac{\beta_z}{\beta_t} = \frac{\omega_t \Delta m \sum_n n^2}{\omega_z \Delta n \sum_{m_l} m_l^2} + \text{Const.} \quad (42)$$

The evolution of the system involves the exponential approach of the point (β_t, β_z) towards the saturation conditions [22].

The trajectory of the point (β_t, β_z) can be controlled by applying rf irradiation with different frequencies. This was the so-called ‘stir-and-scan’ technique where the saturation conditions can be avoided by irradiating different sidebands alternately. This

leads to enhanced changes in nuclear polarization and hence larger sideband features in an NMR experiment. An example is illustrated in Fig 2.5.

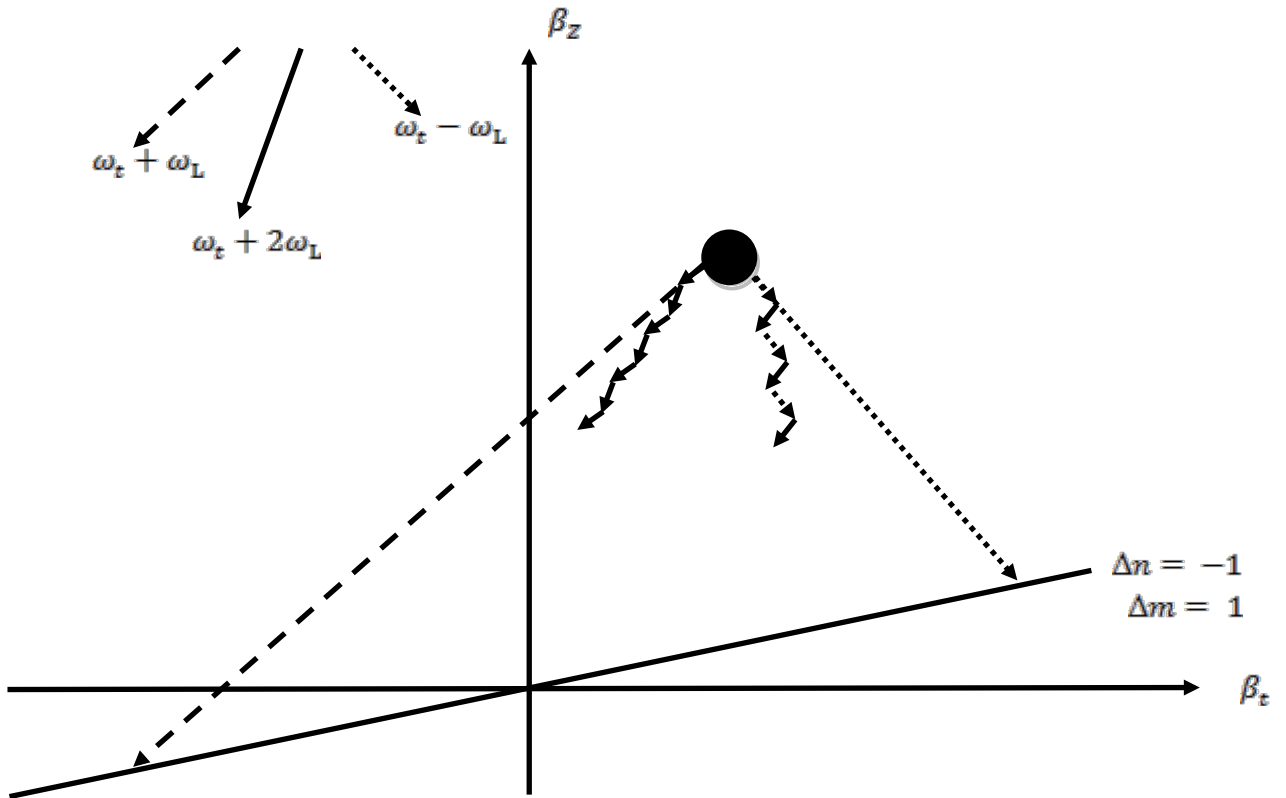


Figure 2.5: Sketch of the population evolution of the Zeeman and tunnelling energy reservoirs when different tunnelling sidebands are irradiated. The saturation conditions can be avoided by a ‘stir-and-scan’ technique involving alternate irradiation of different tunnelling sidebands.

2.5.2. Heat capacities of Zeeman and tunnelling reservoirs:-

We model the system as a couple of thermal energy reservoirs, which relate to the nuclear Zeeman and methyl tunnelling systems. The relative heat capacities of these Zeeman and tunnelling reservoirs are given by,

$$C_z = \hbar \omega_o \left[2 \left(\frac{3}{2} \right)^2 + 6 \left(\frac{1}{2} \right)^2 \right] \quad (43)$$

$$C_t = \hbar \omega_t \left[8 \left(\frac{1}{2} \right)^2 \right] \quad (44)$$

From these equations we conclude:

$$\frac{C_t}{C_z} = \frac{2}{3} \quad (45)$$

At the level crossing where ($2\omega_o = \omega_t$) and:

$$\frac{C_t}{C_z} = \frac{1}{3} \quad (46)$$

at the level crossing where ($\omega_o = \omega_t$). At a level crossing there is efficient thermal equilibration and the two energy reservoirs instantly attain a common inverse temperature $\beta = (C_z\beta_z + C_t\beta_t)/(C_z + C_t)$, for the condition ($\omega_o = \omega_t$) [23].

2.5.3. Methyl ethyl ketone:-

A standard low-field ($B_{low} = 0.018$ T) NMR spectrum was recorded on MEK and is shown in Figure 5.1. Six peaks, assigned (A, B, C, (a+) and (b±)) are observed. The peaks with $\omega_L = \omega_{rf}^A = 715 \pm 1$ kHz and $2\omega_L = \omega_{rf}^B = 1430 \pm 1$ kHz are assigned to the (A) and (B) transitions being the Larmor and twice the Larmor frequencies respectively. The tunnelling frequency $\omega_t = 494 \pm 1$ kHz is, identified by the peak assigned (C), which arises from the pure $\Delta m = 0$ tunnelling. The presence at low field of the pure tunnelling peak (C) shows an important change in the selection rules; at high fields, greater than the dipolar and rf fields, this (A-E) transition involving no net change in spin is forbidden [22].

The frequencies: - $\omega^{a+} = 1.21 \pm 0.001$ MHz, $\omega^{b-} = 0.945 \pm 0.001$ MHz and $\omega^{b+} = 1.92 \pm 0.001$ MHz identifies the peaks (a+) and (b±); these involve, simultaneous transitions in tunnelling and spin states as follows; $\omega_t + \omega_L$, $\omega_t - 2\omega_L$, $\omega_t + 2\omega_L$. The peak (b-) has lower amplitude than the peaks (a+) and (b+), which become more intense with increasing irradiation time. This suggests that the (b-) transition comes near to its saturated situation even at shorter irradiation times, whereas the saturated state of the a+ and b+ transitions only occurs for longer irradiation times [22].

The methyl ethyl ketone molecule ($\text{CH}_3\text{COCH}_2\text{CH}_3$) (2-butanone) has three degrees of freedom with reference to internal rotations: the vibrations of different pairs of methyl groups are twisted and the vibration of the framework in connection to the intermediate (C-C) chain is rounded, as illustrated in Figure 2.6 [24].

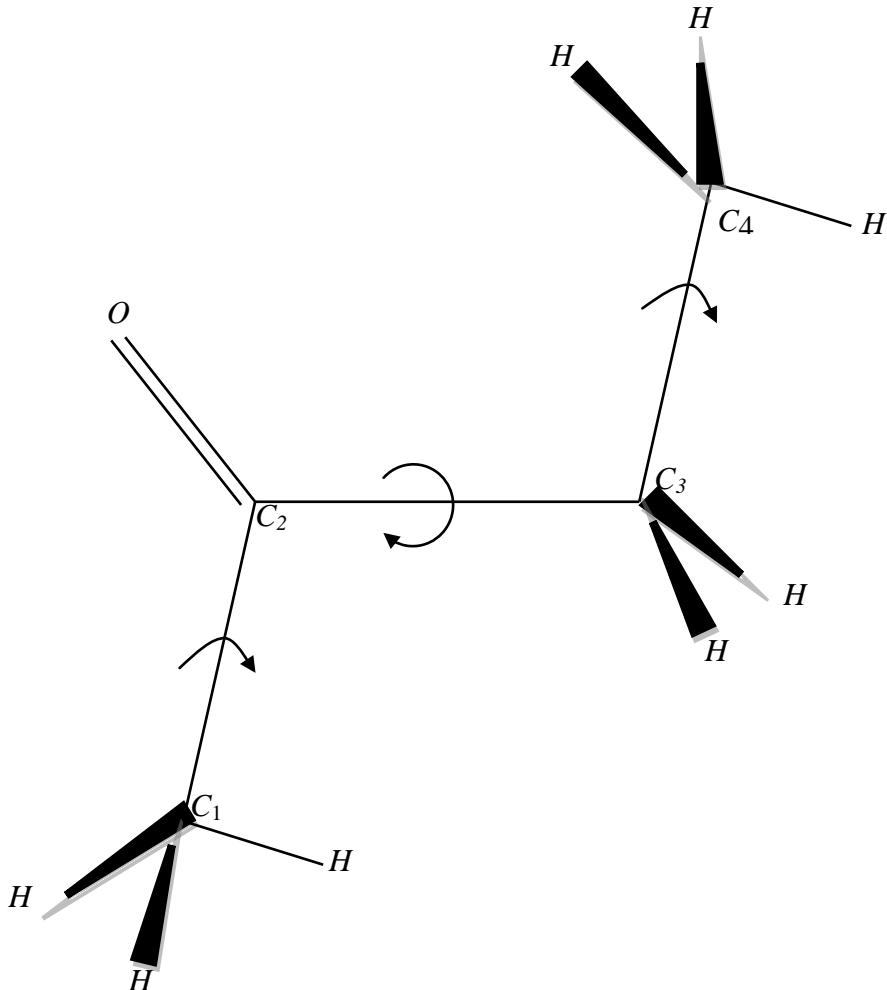


Figure 2.6: The spatial arrangements of the methyl ethyl ketone molecule.

-Internal rotation of the methyl groups:

The tunnelling frequencies of methyl groups have been accurately determined in a couple of samples, i.e. $\omega_t=494\pm1\text{kHz}$ for methyl ethyl ketone and $\omega_t=70\pm1\text{kHz}$ for methylmalonic acid. This technique relies on the breaking of the selection rules at low field [22].

2.5.4. Acetophenone :-

The methyl group reorientation in acetophenone (which is liquid at room temperature, (C_8H_8O)) is known to be hindered by a high potential barrier. This is concluded from the dipole-dipole driven low-field NMR measurements of the proton spin-lattice relaxation time and of the methyl tunnelling frequency ($\omega_t = 1.435$ MHz) [25]. Employing the method of dipole-dipole driven nuclear magnetic resonance, Clough et al. [25] record a study of methyl tunnelling in acetophenone. The NMR tunnelling sidebands are observed to be more intense when the experiment is conducted in the vicinity of a level crossing between the tunnelling and Zeeman sub-levels.

-Tunnelling sideband intensities:-

Experimentally, the intensities of the tunnelling sideband peaks in the low-field NMR spectrum are observed to become enhanced in the vicinity of a level crossing. A theoretical attempt has been made to model the behaviour of the sideband intensities. For a methyl group comprising an equilateral triangle of protons the spin Hamiltonian is given by:

$$H_s = H_z + H_d + H_t \quad (47)$$

where the Zeeman interaction of the proton spins with the applied magnetic field is H_z ,

$$H_z = -\hbar\gamma B_z \sum_{j=1}^3 I_{jz} \quad (48)$$

H_d , represents the methyl tunnelling with an exchange term. The energy shifts that arise from tunnelling are included using the equivalent spin operator;

$$H_t = -2J \sum_{j>k} I_j \cdot I_k \quad (49)$$

The dipole-dipole interaction among the three proton spins is represented by H_d . This is written as multiplication scalar product of two second-rank tensors for the spin and spatial parts:

$$H_d = \sum_{j>k} \sum_{q=-2}^{+2} A_{jk}^{(q)} \cdot A_{jk}^{(q)} \quad (50)$$

Using the simple basis $|m_I^{(1)} m_I^{(2)} m_I^{(3)}\rangle$ the spin-Hamiltonian matrix is defined and may be diagonalised to provide the energy levels and eigenfunctions of the manifold of Zeeman-tunnelling states [25].

2.6 Fundamental theoretical principles for dynamic tunnelling polarization (DTP) experiments:-

2.6.1-Collection of Non -Interacting Spins: - Bulk Magnetization

The sample of hydrogenous molecules contains a collection of 1H nuclei with spin $I = \frac{1}{2}$ [12]. Its nuclear paramagnetic behaviour is determined by the collective properties of many individual nuclear spins. As a result, the sample possesses macroscopic magnetic properties, often termed as the bulk magnetization. For simplicity we assume the spins are non-interacting. Each 1H spin can exist in one of two eigenstates, $|\alpha\rangle$, with $m_I = +\frac{1}{2}$ and $|\beta\rangle$, with $m_I = -\frac{1}{2}$. With spins in thermal equilibrium the populations of these states, in the presence of a static magnetic field B_z are expressed by Boltzmann statistics, as follows.

$$\frac{N_\beta}{N_\alpha} = \exp\left(\frac{-\Delta E}{k_B T}\right) \quad \text{Where } \Delta E = \hbar\gamma B_z \quad (51)$$

The total magnetization is the vector sum of the magnetic moments of the individual nuclei and hence is proportional to the population difference $n = N_\alpha - N_\beta$. The

exponential expansion to the first term in the high temperature approximation

where $k_B T \gg \Delta E$ is: -

$$\exp\left(\frac{-\hbar\gamma B_z}{k_B T}\right) \approx 1 - \frac{\hbar\gamma B_z}{k_B T} \quad (52)$$

This is valid down to milliKelvin temperatures since the Zeeman splitting, is $\hbar\gamma B_z$ so small.

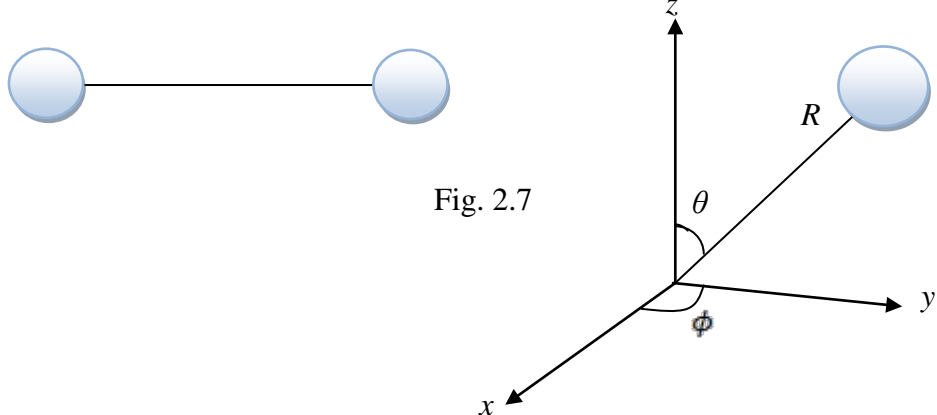
2.6.1.1-Rotational Tunnelling: -

At low temperature, the rotations of hindered symmetrical groups such as H_2 , CH_3 and CH_4 , are described by coherent tunnelling with a characteristic frequency, ω_r . Due to the symmetry of the molecular rotor, the hindering potential energy surface experienced by the rotating group has wells with similar energy.

The effect of particle indistinguishability and the exclusion principle: -

The two protons of the hydrogen molecule rotor are indistinguishable Fermions. Since they are quantum particles, the Pauli Exclusion Principle applies and the total wavefunction for the molecule must be antisymmetric upon exchange of the two 1H nuclei. The system is described as a whole comprising two indistinguishable Fermions and is in sharp contrast with the classical view that makes it possible to follow the trajectories of the individual particles making up the system. The total wavefunction is represented as the product $\Psi = \varphi_{vib}\varphi_{rot}\varphi_{el}\varphi_{nuc}$, where the vibrational wavefunction, φ_{vib} , is solely a function of internuclear distance and under nuclear exchange, it will be always symmetric. The same symmetry applies to the electronic wavefunction, φ_{el} , in the ground state. Hence only the product of rotational and nuclear wavefunctions $\varphi_{rot}\varphi_{nuc}$ determines the symmetry aspects of the molecule under exchange.

Considering the diatomic rotor, altering θ to $(\pi - \theta)$ and ϕ to $(\phi + \pi)$ is corresponding to exchanging the protons of the hydrogen molecule, see Fig. 2.7.



According to the spherical harmonics which define the rotational eigenstates φ_{rot} we find that the eigenfunctions with even values of J ($J = 0, 2, 4, 6, \dots$) are symmetric whereas those with odd values of J ($J = 1, 3, 5, \dots$) are antisymmetric. The nuclear spin quantum number has two values ($m_l = +\frac{1}{2}, -\frac{1}{2}$) and combining these vectorially we find there are three symmetric combinations (Eq.53) (with total nuclear spin $I = 1$) and one antisymmetric combination (Eq.54) (with total nuclear spin $I = 0$). Explicitly the corresponding nuclear spin wavefunction, φ_{nuc} are,

$$\begin{aligned}\varphi_{nuc}^{I=1, m_l=+1} &= \varphi_+(a)\varphi_+(b) \\ \varphi_{nuc}^{I=1, m_l=0} &= \frac{1}{\sqrt{2}}(\varphi_+(a)\varphi_-(b) + \varphi_-(a)\varphi_+(b)) \\ \varphi_{nuc}^{I=1, m_l=-1} &= \varphi_-(a)\varphi_-(b)\end{aligned}\quad (53)$$

$$\varphi_{nuc}^{S=0, m_S=0} = \frac{1}{\sqrt{2}}(\varphi_+(a)\varphi_-(b) - \varphi_-(a)\varphi_+(b)) \quad (54)$$

Since the total wavefunction must be antisymmetric, there are only two allowed combinations, namely 1) the rotational wavefunction is symmetric and the nuclear wavefunction is antisymmetric, $\varphi_{rot}^S \varphi_{nuc}^A$, or 2) the rotational wavefunction is antisymmetric and the nuclear wavefunction is symmetric, $\varphi_{rot}^A \varphi_{nuc}^S$. Case 1) is

para-hydrogen which has total nuclear spin $I = 0$ and hence is invisible to NMR. Case 2) is *ortho*-hydrogen which has nuclear spin $I = 1$ and is defined by states with odd J . This has an NMR signal since the total nuclear spin is non-zero. *Para*- and *ortho*-hydrogen are distinct species called ‘nuclear spin isomers’.

To interchange *para*- and *ortho*-hydrogen requires simultaneous changes in rotational state and nuclear spin state. Therefore, magnetic interactions are required to mediate transitions which interchange nuclear spin isomers.

2.6.1.2-The Methyl Rotor, CH_3 :-

Like the hydrogen molecule, the methyl group, CH_3 , is a quantum rotor which has distinct nuclear spin isomers. In this case the total wavefunction must satisfy the antisymmetry principle under pairwise exchange of two indistinguishable ^1H nuclei.

Similar to H_2 , the Pauli Exclusion Principle applies and only certain symmetry combinations of rotational and nuclear spin wavefunctions are allowed. Many organic molecules contain a methyl group; the latter is a rigid rotor with three-fold axis since it consists of a carbon atom bound tetrahedrally with three hydrogen atoms and the rotational degree of freedom is restricted to a plane. Hence its rotations can be described by a single angle ϕ . The hydrogen atoms of the methyl group undergo non-bonding electrostatic interactions with other atoms nearby, both intermolecular and intramolecular. Therefore during rotation about the three-fold axis there is a periodic change in the potential energy. Thus we can define a hindering potential, $V(\phi)$. The three-fold symmetry exists even if rotation distorts the tetrahedral arrangement of hydrogen atoms. The potential will consist of three wells each of which defines a favoured orientation of the methyl group. The amplitude of the

hindering barrier is typically in the range 0- $\sim 20 \text{ kJ mol}^{-1}$, depending on the sample.

The rotational eigenvalue equation can be expressed as,

$$\frac{-\hbar^2}{2I} \frac{\partial^2 \varphi}{\partial \phi^2} + V(\phi) \varphi = E \varphi \quad (55)$$

With a Fourier series representing the potential of three-fold and higher harmonic parameters

$$V(\phi) = \sum_n \frac{V_{3n}}{2} (1 - \cos(3n(\phi + \vartheta_{3n}))) \quad (56)$$

Where the small offsets in the orientation of these harmonics are defined by the phase angles ϑ . The methyl group with ideal structure has a moment of inertia $I = 5.31 \times 10^{-47} \text{ kg m}^2$.

2.6.1.3-The Exclusion Principle applied to CH_3 : -

The interchanging of any single pair of protons requires that their eigenfunctions be antisymmetric according to the Exclusion Principle. Consider the interchange of positions $\chi_{i=1, 2, 3}$ for protons a, b, c :

$$\chi_1(a)\chi_2(b)\chi_3(c) \rightarrow \chi_1(b)\chi_2(a)\chi_3(c)$$

Incorporating this in a wavefunction,

$$\varphi_n^{(1)} = C' [\chi_1(a)\chi_2(b)\chi_3(c) - \chi_1(b)\chi_2(a)\chi_3(c)]$$

It becomes clear this involves a breaking of two covalent C-H bonds, therefore it is not considered to correspond to any allowable rotation that is consistent with the rotations of a rigid group.

There must be a two pair interchanges to get an allowable rotation of a methyl group,

$$\chi_1(a)\chi_2(b)\chi_3(c) \rightarrow \chi_1(b)\chi_2(c)\chi_3(a)$$

Applying this principle we are able to define wavefunctions that are consistent both with the Exclusion Principle and with the allowable rotations of a rigid methyl group that involves no breaking of C-H bonds.

This provides a framework for describing the allowable states of the CH₃ group.

Analogous to the previous analysis of the hydrogen rotor the complete wavefunction of the CH₃ system, Ψ , including all degrees of freedom, $\Psi = \varphi_{vib}\varphi_{rot}\varphi_{el}\varphi_{nuc}$, must be antisymmetric with respect to two pair exchange. Similar to H₂, the product of rotational and spin functions determine the properties of the methyl group since the vibrational and electronic wavefunctions are symmetrical.

The symmetries are determined by the irreducible representations of the three-fold symmetry group, C₃. For a methyl group there are two A-symmetry possibilities for nuclear spin states α, β; which are:-

$$\psi_{I=3/2} = \alpha(a)\alpha(b)\alpha(c) \quad \psi_{I=-3/2} = \beta(a)\beta(b)\beta(c)$$

The remaining spin functions can be written

$$\psi_I = \frac{1}{\sqrt{3}}(\alpha(a)\alpha(b)\beta(c) + \lambda_r\beta(c)\alpha(a)\alpha(b) + \lambda_r\alpha(b)\beta(c)\alpha(a))$$

$$\psi_I = \frac{1}{\sqrt{3}}(\beta(a)\beta(b)\alpha(c) + \lambda_r\alpha(c)\beta(a)\beta(b) + \lambda_r\beta(b)\alpha(c)\beta(a))$$

Where there are A-symmetry combinations ($\lambda_r = 1$), E_a symmetry combinations ($\lambda_r = \varepsilon$) and E_b symmetry combinations ($\lambda_r = \varepsilon^*$). As a result there are eight spin states; four with A-symmetry representing the nuclear spin quartet of spin 3/2; and a pair of spin doublets with total nuclear spin 1/2 represents the E symmetry states.

These symmetry adapted spin functions must be combined with symmetry adapted rotational functions to form the total wavefunctions of the CH₃ group. The allowable combinations consistent with the Exclusion Principle are the three products [12];

$$A^{(\text{rotor})} A^{(\text{spin})} ; E_a^{(\text{rotor})} E_b^{(\text{spin})} ; E_b^{(\text{rotor})} E_a^{(\text{spin})} \quad (57)$$

2.6.2- Dipolar and Zeeman orders: - Investigating the meaning of [26] dipolar and Zeeman orders is essential to this thesis which is concerned with methyl tunnelling. The dipolar interactions are important in studying the NMR of all solids, while the Zeeman interaction characterizes the magnetization state that exists when the specimen, including nuclear spins, is placed in an external magnetic field B_o . The magnetization of a particular nuclear species is parallel to the external field, representing the vector sum of the magnetic moments associated with all spins. For spin-1/2 there are two energy states corresponding to ‘spin-up’ and ‘spin-down’ configurations with respect to the applied external field. At equilibrium, the Boltzmann population difference determines the magnitude of the magnetisation. If the system is not in equilibrium then the period required by the magnetization M to reach $1-1/e$ of its equilibrium magnetization (M_o) is the spin-lattice relaxation time T_1 as shown in Fig. 2.8.

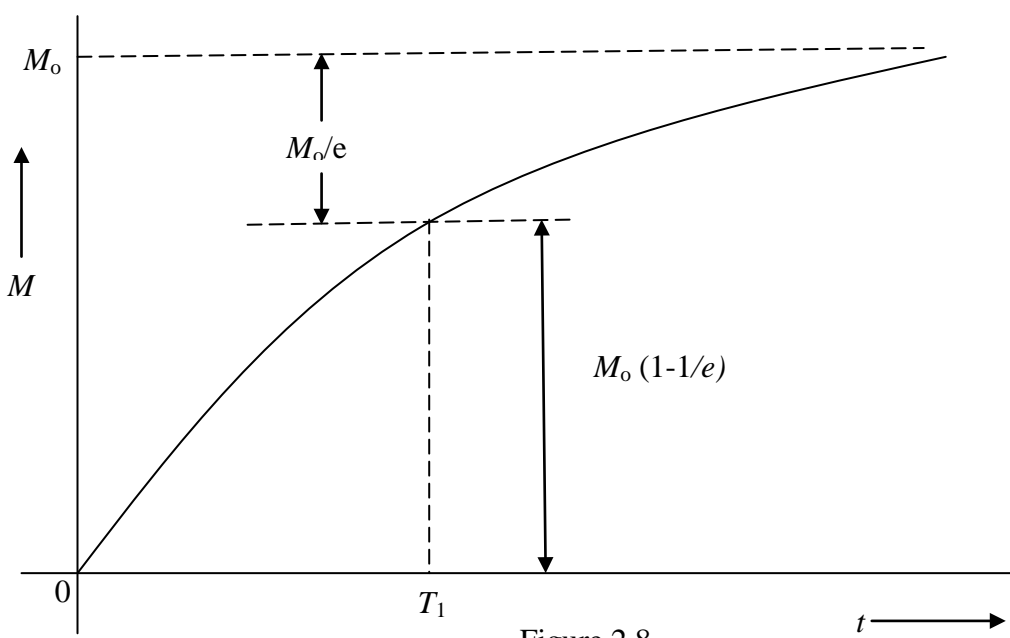


Figure 2.8

- Zeeman Energy Eigenfunctions: - A static magnetic field [27] is applied to a nucleus with a magnetic moment μ , and by definition the induction of the field B_o coincides with the z -axis. Thus the interaction between a nuclear magnetic moment μ and a magnetic field will yield the following scalar vector product as a definition of energy

$$E = -\mu \cdot B_o = -B_o \mu_z = -B_o \gamma \hbar I_z \quad (58)$$

The operator of energy (the Hamiltonian) of this classical definition is achieved by handling the spin coordinate I_z as an operator

$$\mathcal{H}_z = -\mu \cdot B_o = -B_o \cdot I_z \hbar \quad (59)$$

Recalling that B_o is aligned along the z -axis, where $\omega_o = -\gamma B_o$

$$\mathcal{H}_z = -B_o \gamma \hbar I_z = \hbar \omega_o I_z \quad (60)$$

This is called the "Zeeman Hamiltonian" which defines the splitting of the energy levels in the Zeeman Effect. Consequently \mathcal{H}_z has the following eigenfunctions in the magnetic field B_o

$$E(m) = -B_o \gamma \hbar m \quad (61)$$

This represents the permitted $(2I+1)$ "Zeeman levels" for a free nucleus (with spin quantum number I and gyromagnetic ratio γ). This energy results from the interaction of a spin with the static external magnetic field. The "spin" term represents a nucleus with non-zero spin and its magnetic moment. There will be a similar energy difference separating levels that have sequential quantities of m which vary by 1. In a quantum model consisting of non-interacting N spins that interact with the applied magnetic field B_o , this Zeeman splitting is

$$\Delta E = E(m) - E(m-1) = -\gamma \hbar B_o \quad (62)$$

The [28] spin momentum I refers to the particle's intrinsic angular momentum when it rotates with respect to its centre of mass and consequently there will be a magnetic moment μ collinear with I , as follows:

$$\mu = \gamma \hbar I \quad (63)$$

Where γ is the gyromagnetic ratio with different constant values for each isotope, and for a proton (1H) is equal to $26.75 \times 10^7 \text{ rad T}^{-1} \text{ s}^{-1}$; \hbar , is the Planck constant divided by 2π ($\hbar = 1.055 \times 10^{-34} \text{ Js}$).

- Nuclear Zeeman splitting: - Employing NMR is useful in studying the spectroscopy of the nuclear Zeeman sublevels which are separated by a nuclear Zeeman splitting [16]. This effect of the applied magnetic field on the nuclear Zeeman levels of a 1H nucleus is illustrated in figure 2.9.

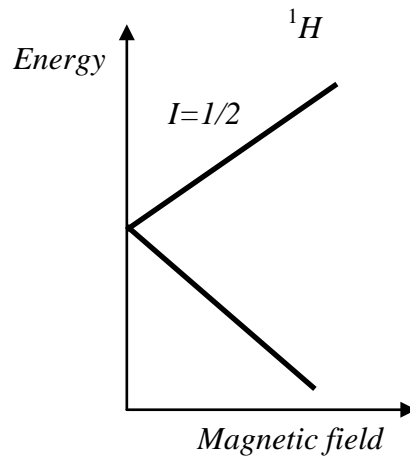


Figure 2.9: - The 1H nuclear ground states with its Nuclear Zeeman sublevels.

Two sublevels result from applying the static magnetic field to the 1H nuclear spin-1/2, corresponding to $m_I = +\frac{1}{2}$ and $m_I = -\frac{1}{2}$.

The classification of molecular dynamics that characterise the sample [16] on a specific time-range will be assigned to either *intramolecular* or *intermolecular* spin interactions. This is a useful concept when representing the motionally averaged spin Hamiltonian. These spin interactions parameters are affected by the diffusion of particles that maybe on the same molecule (intramolecular) or different molecules (intermolecular). Both intramolecular and intermolecular combinations shown in the following figure (2.10) are occurring during internal spin interactions.

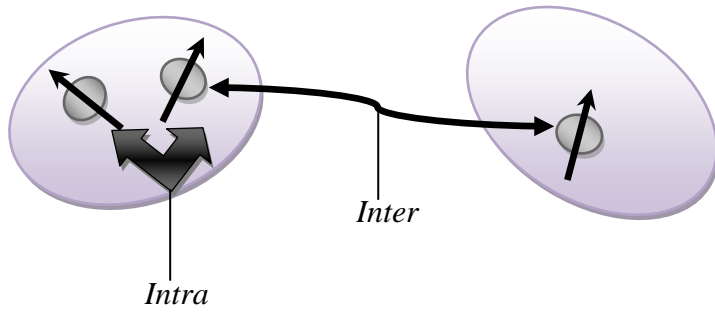


Figure 2.10: - *Intramolecular* and *intermolecular* dipole-dipole combinations.

The mathematical analysis of intrinsic spin angular momentum physics has concluded that particles possessing a spin value $I = 1/2$, will have degeneracy $2I+1$. Hence there are two possible magnetic states defined by quantum number $m_I = +1/2, -1/2$.

- The resonance consequence of the Zeeman Effect (the instinctive approximation): -

If an electromagnetic wave with an energy difference that matches the relationship

$\Delta E = \hbar v$ is supplied to the Zeeman manifold, a transition is driven between nuclear spin states. This is the basis of nuclear magnetic resonance (Figure 2.11) [28].

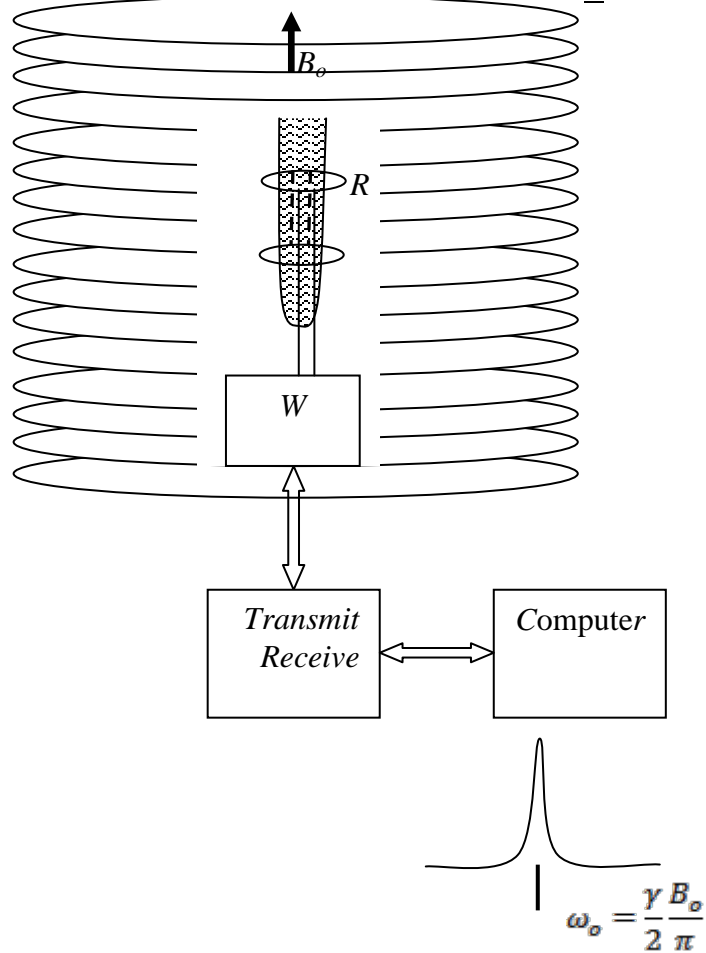


Figure 2.11 The spins inside the sample situated at the centre of the magnet experiences a Zeeman splitting in its energy levels. The stable high magnetic field B_o is supplied by current in a superconducting coil R while the transverse Helmholtz coil R which is tuned at the Larmor frequency ω_o in the circuit W has two intentions:

- The activation of the transition among two levels by producing a time dependent rf magnetic field perpendicular to B_o (transmit function);
- As a receive function to record the NMR signal.

The transition or resonance (Larmor) frequency $\omega_o = \gamma B_o / 2\pi$ depends on the value of the applied field. Practically there will be an observable equilibrium nuclear magnetization M aligned parallel to B_o (longitudinal magnetization). At equilibrium the transverse magnetization is zero. However, following a resonant rf pulse, the system is disturbed away from equilibrium and acquires a component of magnetization transverse to the applied field. This exhibits Larmor precessional motion around B_o , and proceeds at a

frequency exactly equal to ω_o (Figure 2.12). Finally detection of this precession occurs when \bar{M} will be in a plane that contain the coil (Figure 2.11) and perpendicular to B_o , this arrangement generates an electromotive force (emf) across the coil with amplitude that is proportional to \bar{M} while its frequency produce ω_o ; this emf is the NMR signal.

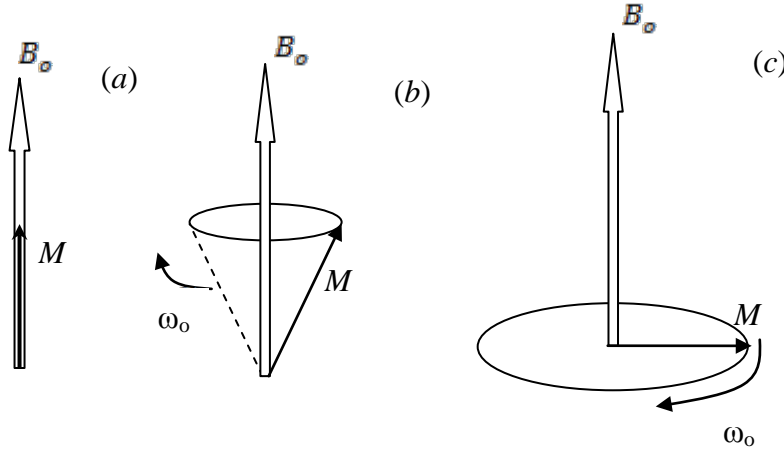


Figure 2.12 (a) the nuclear magnetization \bar{M} aligned parallel to the applied field B_o at thermal equilibrium. (b) the position of \bar{M} is rotated in response to an rf pulse. Subsequently the magnetization which is transverse to the field, exhibits a precessional motion around B_o at the Larmor frequency ω_o . (c) this motion activates a voltage in the coil R (Figure 2.11) which is in a plane perpendicular to B_o .

A concept that changed the initial idea of magnetic resonance is double resonance [29] in which one resonant transition of a system is synchronized by simultaneously driving a different transition. Reviewing the initial double resonance experiments conveys the essential idea leading to the subject of dynamic nuclear polarization within the Overhauser-Pound family of Double Resonance. The Overhauser effect, in its original form was applied to the interaction between two spins, however, as we shall see, it is applicable in the experiments recorded in this thesis to the interaction between a spin system and a tunnelling system.

In the Overhauser effect, transitions between energy levels of a system (under an external static magnetic field B_o) in the presence of electron-nuclear coupling are best

described by the Hamiltonian of this system which contains of a nucleus (n) with spin $I=1/2$ coupled to an electrons (e) of spin $S=1/2$, as

$$\mathcal{H} = \gamma_e \hbar B_o S_z + A_s^n I \cdot S - \gamma_n \hbar B_o I_z \quad (64)$$

where A_s^n represent the size of the electron-nuclear coupling.

2.6.3- Polarization by forbidden transitions: - The Overhauser effect can occur if there is a restriction on the nuclear relaxation pathway, such as the transition probabilities per unit time W_{13} , W_{24} . Then pumping a transition in which both electron and nuclear spins flip (like W_{23} or W_{14}) can then lead to strong changes in the relative populations of the nuclear spin levels and hence to the nuclear spin polarization [29]. Strongly non-equilibrium Electron spin-flip operations (like W_{12} , W_{34}) are the more efficient $W_{ij}s$ since nuclei interact less strongly with the lattice than does the electron. Reaching a proton polarization state of over 70% may occur as a result of pumping a forbidden transition. In Figs. 2.13 and 2.14 there are illustrations of two forbidden transition schemes.

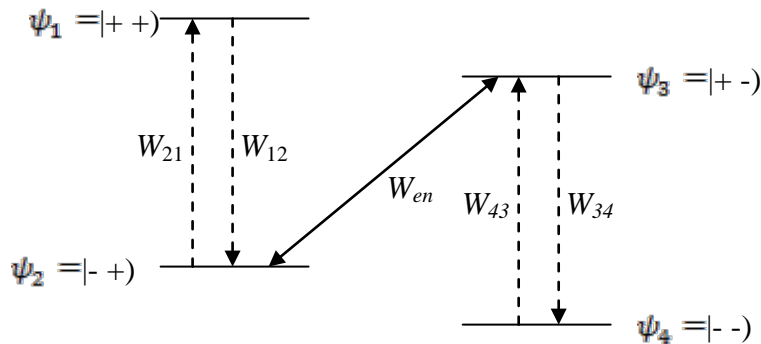


Fig. 2.13. The generation of nuclear polarization by a prohibited transition, W_{en} , that connects levels 2 and 3 and flips both the electron and nuclear spins.

While the transition of Fig. 2.13 can be activated by time-dependent rf field parallel to the static field, the transitions of both Figs. 2.13 and 2.14 can be activated by time-dependent rf fields which are perpendicular to B_o .

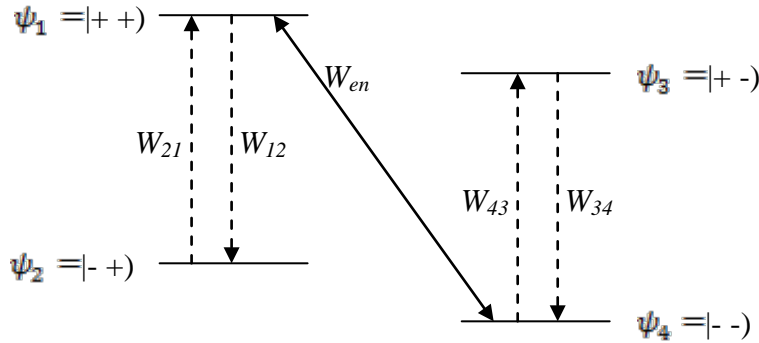


Fig. 2.14. The generation of nuclear polarization with opposite sign to that of Fig.2.13 by the forbidden transition connecting levels 1 and 4.

The transition matrix elements in Fig. 2.13 and 2.14 which involve the dipole-dipole coupling between a nucleus at distance r from the electron is of order $\gamma_e \hbar / r^3 B_o$ times the matrix parameter in which solely an electron is flipped. This ratio is affected by the angle the static field makes with the axis connecting the nucleus and the electron. Strong pumping with an rf field of the forbidden transition overcomes the effects of the thermal transition rates W_{ij} . Supposing that the effective transitions $B_{i,j}$ are solely those illustrated in Fig.2.14 in which the transition among states 1 [$\psi_1 = |++\rangle$] and 4 [$\psi_4 = |--\rangle$] is saturated, we directly conclude that

$$p_1 = p_4 \quad (65)$$

$$p_2 = p_1 B_{12} \quad (66)$$

$$p_3 = p_4 B_{43} \quad (67)$$

so that

$$p_1 = p_4 = \frac{1}{2 + B_{12} + B_{43}} \quad (68)$$

$$p_2 = \frac{B_{12}}{2 + B_{12} + B_{43}} \quad (69)$$

$$p_3 = \frac{B_{43}}{2 + B_{12} + B_{43}} \quad (70)$$

The collective effect will be,

$$\begin{aligned} \langle I_z \rangle &= \frac{1}{2} (p_1 + p_2 - p_3 - p_4) \quad (71) \\ &= \frac{1}{2} \frac{B_{12} - B_{43}}{2 + B_{12} + B_{43}}. \end{aligned}$$

Comparing the latter with the high temperature limit

$$\langle I_z \rangle = \frac{1}{2} \frac{\gamma_e \hbar B_o}{2 k_B T} \quad (72)$$

Hence the improvement over the equilibrium polarization constitutes the Overhauser effect.

$$\frac{\langle I_z \rangle}{\langle I_z \rangle_{therm}} = \frac{\gamma_e}{\gamma_n}, \quad (73)$$

2.6.4-Adiabatic field changes

When the magnetic field is switched in a field-cycling experiment, the spacing of the energy levels changes but the populations of the energy levels remain unchanged; the field switches are adiabatic [12]. Therefore, the temperature of the Zeeman reservoir changes in response to B -field. Since the Zeeman populations are proportional to inverse temperature and applied field $p \propto B_z \beta_z$, then β_z simply scales with B_z . Switching between fields B_{z1} and B_{z2} changes the inverse Zeeman temperature as follows,

$$\beta_{z2} = \frac{B_{z1}}{B_{z2}} \beta_{z1}$$

2.6.5- The investigation of Methyl tunnelling spectra: - The scale of barrier heights experienced by methyl groups in various molecules spans a range of approximately two orders of magnitude [12]. Due to the exponential dependence this will cause the scale of methyl tunnelling frequency to span a range of six or seven orders of magnitude. Hence

for strongly hindered methyl rotors, $\omega_t^{(0)}$ can be very small in some kHz value while for weakly hindered rotors, $\omega_t^{(0)}$ will be in order of 100 GHz. Therefore a variety of magnetic resonance methods have been developed to measure the tunnelling frequencies, each suitable for a different range in the frequency spectrum.

2.6.5.1-The investigation of tunnel resonance through the level crossing technique: -

Under appropriate conditions strong changes in the nuclear spin-lattice relaxation rate, T_1^{-1} can be used to reveal the methyl tunnelling frequency. These conditions occur when the magnetic field is tuned so that the Larmor frequency of a nuclear or electron spin is brought into resonance with the tunnelling frequency. To give access to such ‘tunnel resonances’ a variable field NMR spectrometer is required, employing field-cycling in the NMR pulse sequences. Typical procedures are as follows:

- (a) Supply a train of resonant rf pulses to saturate the proton spins at field B_{nmr} .
- (b) Switch the magnetic field rapidly to B_r .
- (c) Allow the magnetization to evolve in the field B_r for time τ_{rec} .
- (d) Return to NMR resonance at B_{nmr} through a fast field switch.
- (e) Apply a resonant rf pulse to determine the proton magnetization M_z .

This field-cycling procedure can be employed to determine the magnetic field dependence of the proton spin-lattice relaxation rate by systematically increasing B_r . With the initial saturation of the proton Zeeman energy reservoir the tunnel resonances are revealed by plotting the longitudinal magnetization that evolved during the constant time $\tau_{rec} < T_1$. Since at low temperature in ordered crystalline solids the proton spin-lattice relaxation time is long in comparison with the magnetic field switching time, the field-cycling experiment is able to perform well.

2.6.5.2-The investigation of NMR tunnel resonance spectra: - The first ‘tunnel resonance’ experiment was reported by Van Hecke and Janssens on the tunnelling

manifold of a tetrahedral rotor SiH_4 [12]. The technique has since been extended to methyl rotors and Fig 2.15 shows the magnetic field dependence of the methyl tunnelling levels and the level crossings that occur at $\omega_L = \omega_t$ and $\omega_L = \omega_r/2$ (In reality the energy levels invariably ‘anti-cross’, corresponding to ‘avoided level-crossings’ since there are often additional magnetic interactions connecting the A and E states). $A_{-3/2}$

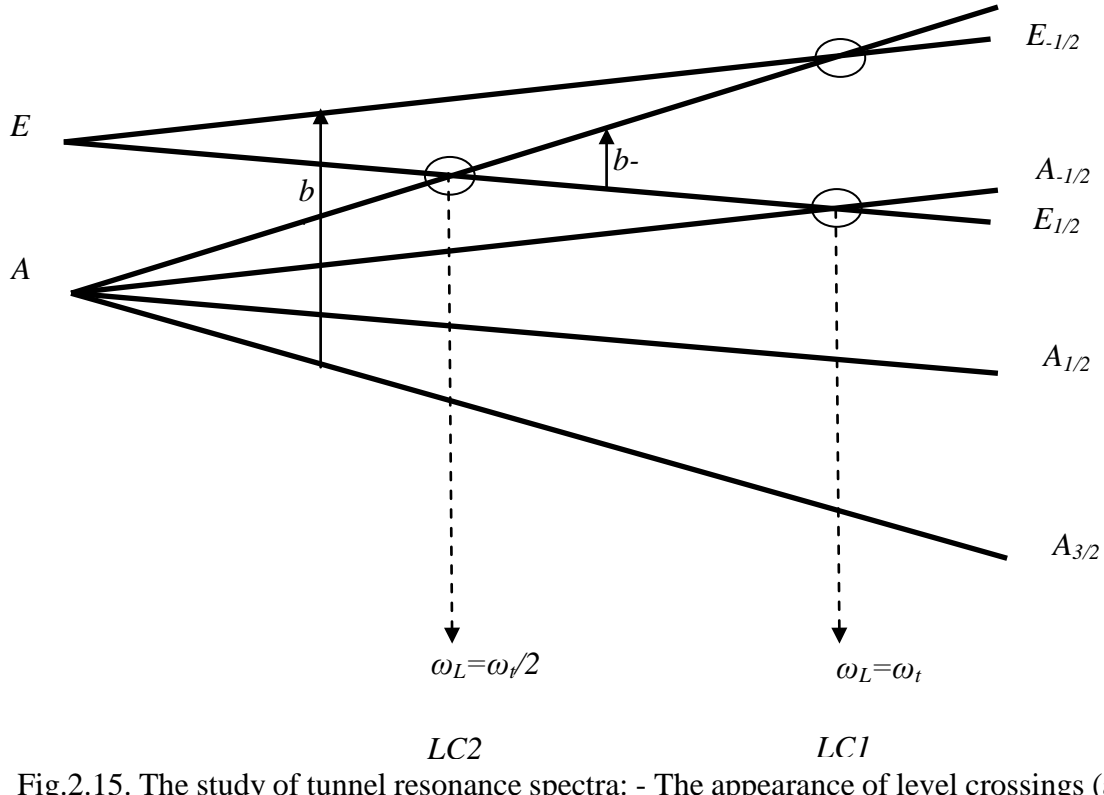


Fig.2.15. The study of tunnel resonance spectra: - The appearance of level crossings (at $\omega_L = \omega_t$ and $\omega_L = \omega_r/2$ which are 340 G and 170 G respectively in the case of acetophenone) revealed due to the A and E energy levels dependence on the applied magnetic field, with the opposite transitions of the $b+$ and $b-$ peaks.

The achievement of these tunnel resonance criteria at the level-crossings gives rise to strong relaxation between the tunnelling and Zeeman reservoirs, mediated by the dipolar interactions. This cross-relaxation will induce the equilibration to be a non-exponential process. A model describing the system as two resonantly coupled energy reservoirs is found to be effective in interpreting these experiments [12].

A common feature of tunnel resonance experiments is hysteresis; because the tunnel reservoir has limited heat capacity and is isolated from the lattice, the outcome of a particular magnetization measurement will depend on previous measurements. This means it is necessary to devise careful pulse sequence procedures to ensure that systematic data will result. This usually involves ensuring the Zeeman and tunnelling temperatures have as close to reproducible values as possible before each cycle in the pulse sequence.

- Experimental determination of the Longitudinal (spin-lattice) Relaxation time: - The first step in measuring the spin-lattice relaxation time requires the Zeeman system to be disturbed away from equilibrium [28]. This can be achieved by applying resonant rf pulses. The subsequent recovery of the magnetization is then monitored by allowing the Zeeman system to evolve in a specified magnetic field. The final measurement of the magnetization is achieved with a single resonant rf pulse. The maximum disturbance away from equilibrium is an essential condition for making an accurate measurement of the relaxation time. Commonly this involves either completely saturating the magnetization with a train of 90 degree pulses, or inverting the magnetization with a single 180 degree pulse. This experimental procedure is illustrated in Figure 2.16 where initially a full inversion is achieved by an 180° r.f. pulse and after a relaxation period a 90° pulse is used to measure the longitudinal magnetization by transforming it to a measurable transverse magnetization.

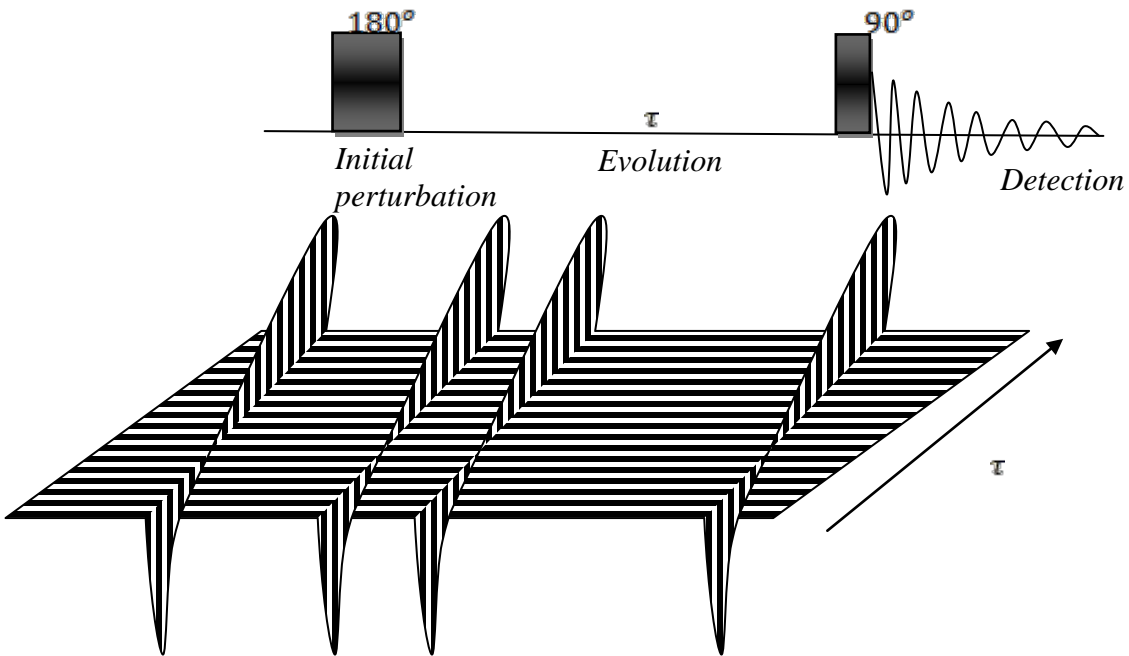


Figure 2.16 The development of longitudinal relaxation time using the inversion recovery sequence. The 90 degree pulse produces a free induction decay which is Fourier transformed to provide the NMR spectrum. The inversion-recovery sequence is used to build a magnetization-recovery curve by recording the NMR spectra as a function of recovery time. The estimation of these specific T_1 proximate values from left to right are: 20.5s, 19.8s, 23.3s and 19.3s [28].

The longitudinal nuclear magnetization evolves according to the following Bloch equation

$$\frac{dM_z}{dt} = -\frac{M_z - M_o}{T_1} \quad (74)$$

By solving the first order differential equation we get:

$$M_z(\tau) = M_o + [M_z(0) - M_o] \exp(-\tau/T_1) \quad (75)$$

The value of $M_z(0)$ depends on the initial conditions. For inversion recovery ($M_z(0) = -M_o$) and (75) becomes

$$M_z(\tau) = M_o [1 - 2 \exp(-\tau/T_1)] \quad (76)$$

Chapter 3 Experimental

3.1 Introduction to pulsed NMR spectroscopy:-

The specimen in a pulsed nuclear magnetic resonance (NMR) experiment is exposed to a strong rf pulse with a maximum $\overline{B_1}$ greater than that employed in CW scientific procedures. At resonance (where $\overline{B_n} = \overline{B_1}$) the nuclear magnetization rotates around $\overline{B_1}$, with the angular frequency $\gamma\overline{B_1}$, i.e. in the y - z plane when the rf is polarized along the x -axis. At resonance this is illustrated in Figure 3.1, where the $\overline{B_1}$ pulse is on for period τ ; this will induce the magnetization vector to move in a circle around an axis by an angle $\gamma\overline{B_1}\tau$. A 90° (or a $\pi/2$) pulse will be generated when the product $\overline{B_1}\tau$ is exactly $\pi/2$, so at the end of the pulse the magnetization is perpendicular to the applied static B -field.

In the case shown, after a 90° pulse the magnetization will be pointing along the y -axis in the rotating frame. With time, the magnetisation returns to thermal equilibrium. There are longitudinal and transverse components to this process. The transverse magnetization systematically decays towards zero as the individual spins lose their phase coherence with each other. This loss of phase coherence comes about due to spin-spin interactions and due to inhomogeneity of the applied magnetic field.

The magnetization will produce by induction across the coil in which the sample is contained, a decaying alternating electromotive force (emf). This is the origin of the NMR signal, or free-induction decay (FID). The FID is an oscillating and decaying sine wave diminishing as $\exp(-\frac{t}{T_2^*})$, with time constant T_2^* .

Meanwhile, the longitudinal magnetization steadily regrows towards its equilibrium magnetisation with time constant, T_1 , which is the spin-lattice time, T_1 . This growth is described as $M_z(t) = M_o(1 - e^{-\frac{t}{T_1}})$. This is illustrated in Figure 3.2, where the time

constant for transverse magnetization, T_2 , is usually shorter than that of the longitudinal magnetization, T_1 .

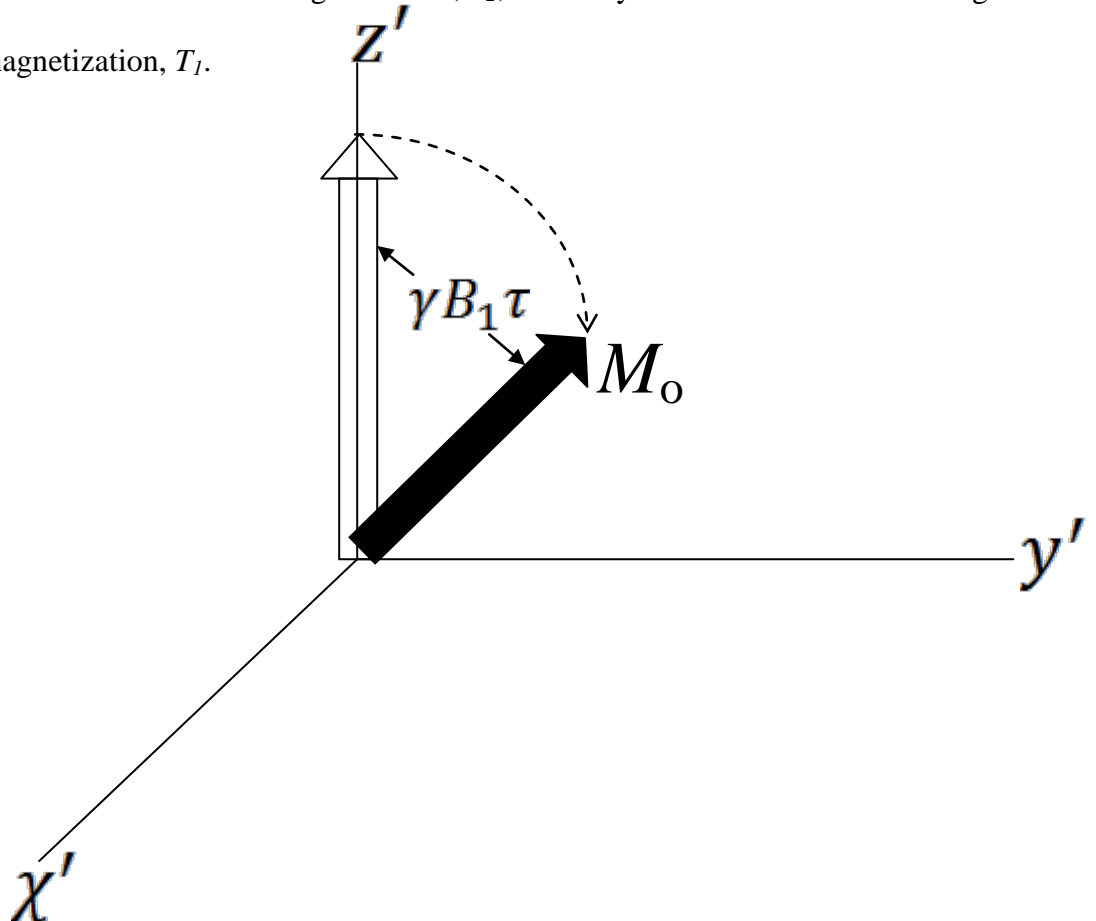
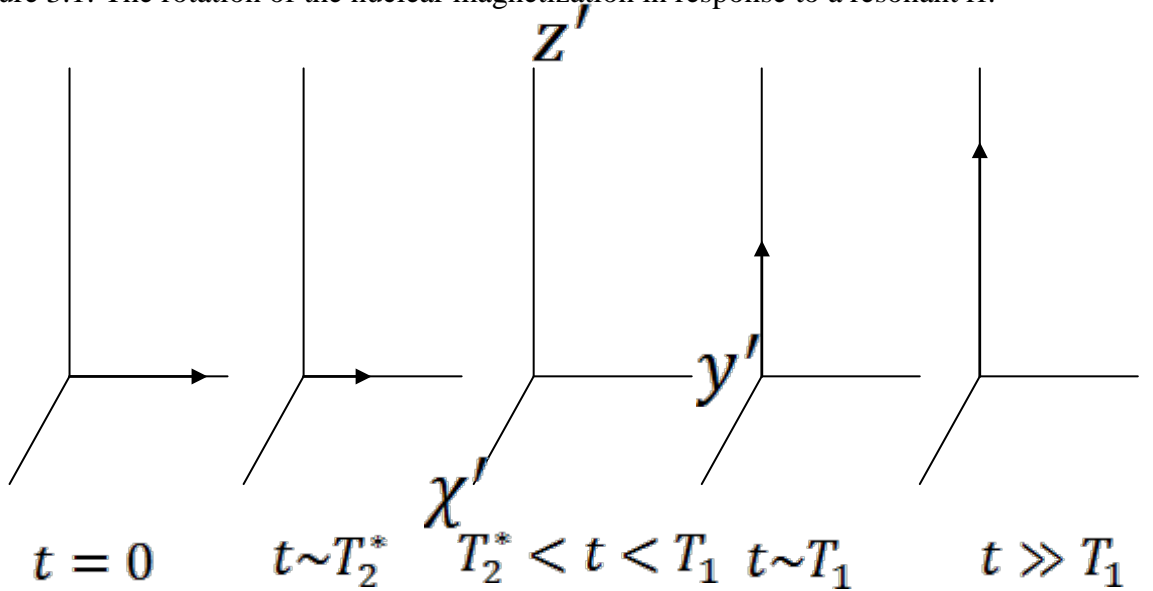


Figure 3.1: The rotation of the nuclear magnetization in response to a resonant rf.



Decaying Signal

Figure 3.2: The decay of the transverse magnetization as it returns to thermal equilibrium.

equilibrium.

-Spin-lattice relaxation calculations in the rotating shape:

Initially the realizing of the measurement practical procedure is necessary to realize the spin-lattice relaxation calculations in the rotating shape which is achieved by the next resemble method.

When the sample is placed for a period of many T_1 s in a region of high magnetic field, $\overline{B_o}$, a magnetization $\overline{M_o}$ will exist in the direction of $\overline{B_o}$ (as illustrated in Fig.3.3).

Following a 90° pulse about the x' axis in the rotating frame, the magnetization will be rotated in the $-z$ plane so that the magnetization is aligned along the y' –axis in the rotating frame, where it precesses with the Larmor frequency. When the rf is supplied on resonance in the rotating frame, the magnetization encounters solely the B_I region and not the B_o region, since the magnetization and the B_I field circulate in the x-y plane.

A similarity appears consequently between the B_I field in the rotating frame and the B_o field in the laboratory frame and the magnetization is said to be spin-locked to $\overline{B_I}$.

Given that C is the Curie constant and T_L is the lattice temperature, the magnetization $\overline{M_o}$ (which has magnitude $M_o = CB_o/T_L$) is polarized because of the phase change in the direction of a very less than average region $\overline{B_I}$ in the rotating frame and, consequently, it will restore equilibrium with a mathematical expression containing an exponent period fixed number $T_{I\rho}$ to a smaller equilibrium quantity M , with magnitude

$$M = CB_I/T_L$$

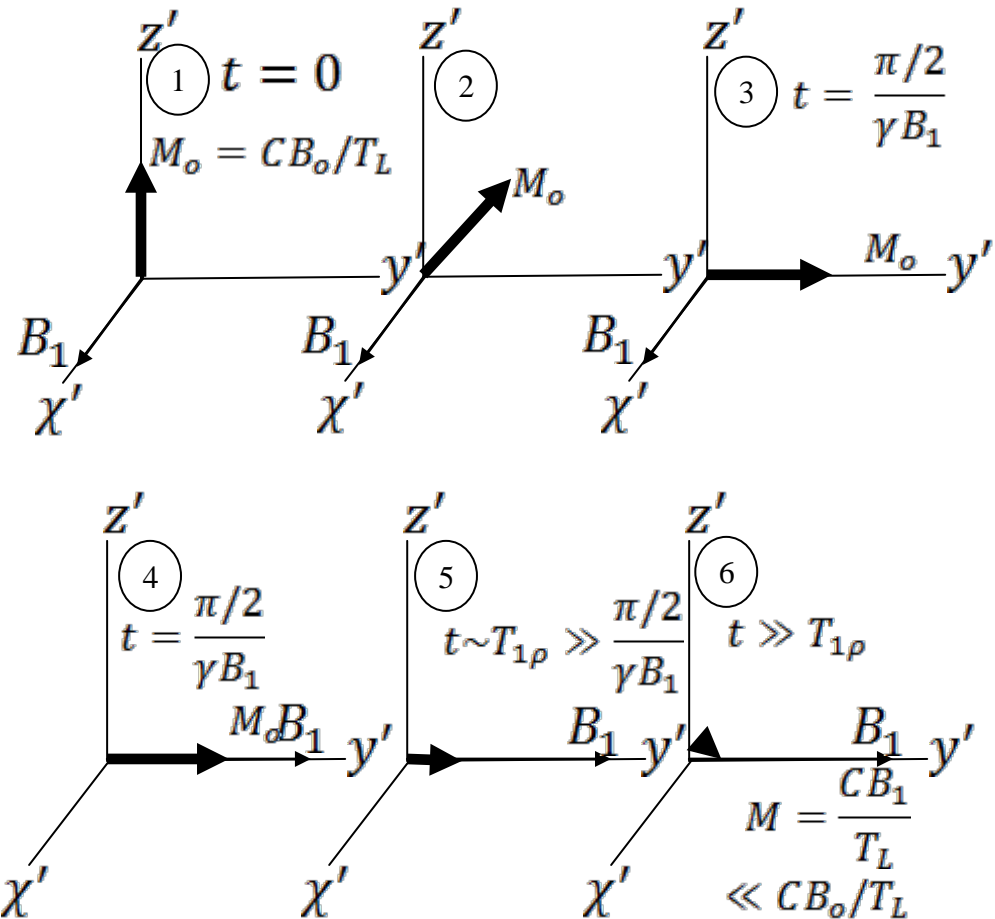


Figure 3.3: The spin-lattice relaxation process in the rotating frame.

3.2 NMR pulse sequences:-

A very close reliance on the motional operations characterized the spin-lattice relaxation time T_1 that exists in every part of a specimen. The set of answers explaining the basic features relating to molecules dynamic that occur is concluded from an exact action of measuring T_1 as a function of temperature and magnetic field [30].

3.2.1 Saturation-recovery pulse sequence:-

Spin-lattice relaxation may be described (supposing the static magnetic B field is directed along the z axis) by the following expression (1):

$$\frac{dI_z}{dt} = \frac{I_o - I_z}{T_1} \quad (1)$$

Where I_o relates to the equilibrium nuclear polarization and I_z is the z component of the bulk polarization. The evolution of I_z towards thermal equilibrium is found from the

solutions of this differential equation which represent an exponential recovery towards I_0 as follows:

$$I_z(t) = I_o \left(1 - e^{-\frac{t}{T_1}} \right) \quad (2)$$

To determine T_1 experimentally, we used a field-cycling adaptation of the standard saturation-recovery pulse sequence, Fig 3.4. Following one another at short intervals, a burst of $\pi/2$ impulses, which define a "comb" or saturation pulse "train", are supplied to the sample, setting the longitudinal magnetization to zero. The sample is permitted to recover towards equilibrium for a period τ_{rec} , followed by the application of a $\pi/2$ measurement pulse. A recovery curve, obtained by repeating this sequence for a range of τ_{rec} values (at the minimum 20). The recovery of the polarization was monitored by making measurements with increments in the logarithm of time. With the purpose of identifying T_1 , the polarization recovery curve may be fitted by equation (2). The satisfactory determination of the "baseline" (appropriate at small τ_{rec}) and the equilibrium plateau (appropriate at large τ_{rec}) is of great significance to make consistent, reliable evaluations of T_1 . With the purpose of specifying the temperatures existing at the T_1 minima for every specimen, at a constant region ($Br = B_{NMR}$), T_1 was ascertained above a number of temperatures (impulse particular order as illustrated in plot. 3.4) [30].

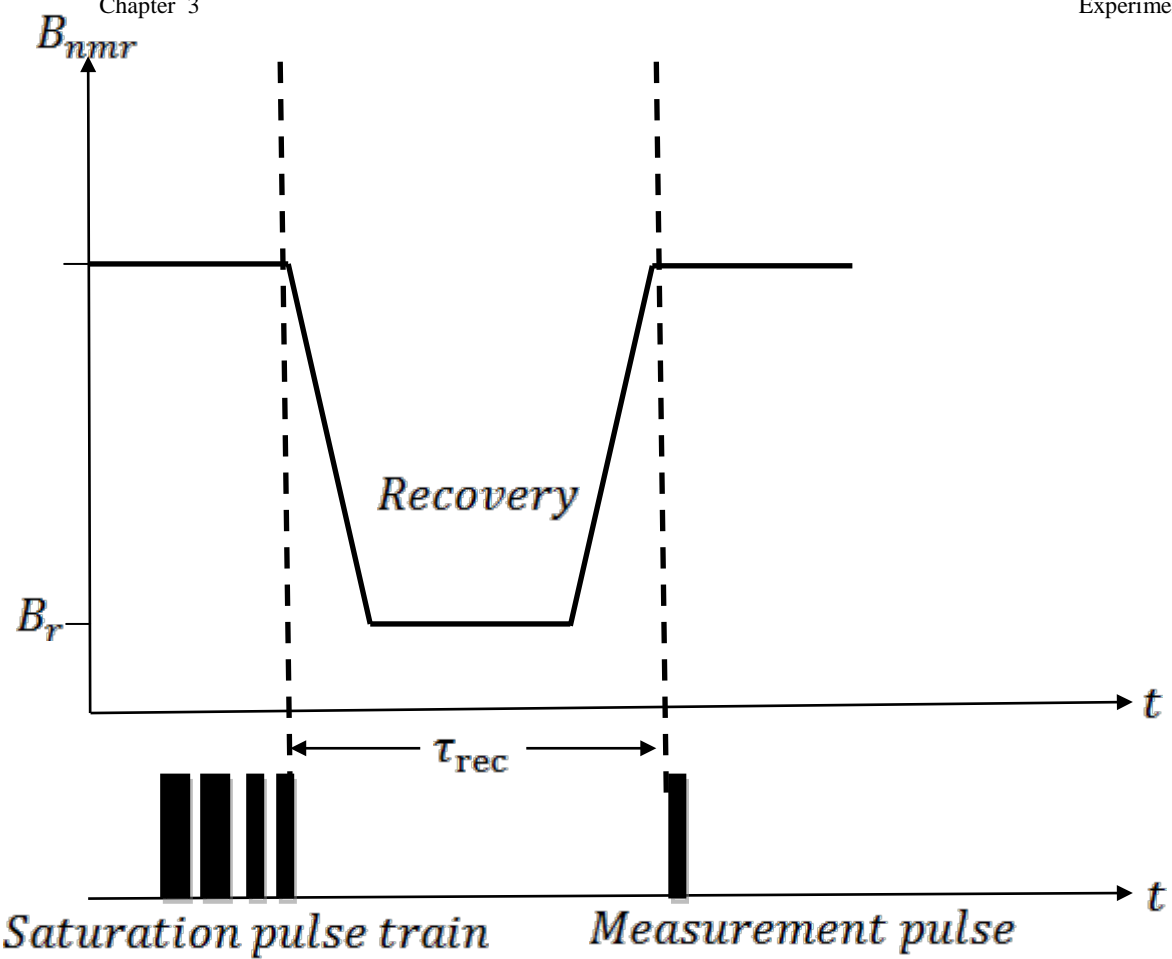


Figure 3.4: The saturation-recovery field-cycling NMR pulse sequence enabling T_1 to be measured as a function of field, B_r .

3.2.2 Curve fitting:-

-Spin-Lattice relaxation:-

In section (3.2.1) we show, by using a standard $(\pi/2)_x - \tau - (\pi/2)_x$ pulse sequence, that the magnetization recovery follows the successive solution [31] of the Bloch equation(3),

$$I_z(t) = I_o \left(1 - e^{-\frac{t}{T_1}} \right) \quad (3)$$

For a recovery field $B_r = 0.682$ T and at various temperatures, the characteristic magnetization recovery curve for the saturation – recovery pulse sequence is illustrated in sections 4.7 and 5.4 and will be regularly fitted to relation (4) to permit for magnetization – recovery throughout the duration of the field switches.

$$I_z(t) = I_o \left(1 - e^{-\frac{t}{T_1}} \right) + C \quad (4)$$

where C is a constant. The spin-relaxation time is obtained from fitting the magnetization ascertained at various recovery times [32].

3.3 The NMR spectrometer:-

The recording and measurement of spectra was carried out using a custom built field-cycling NMR spectrometer. The rf circuitry is based around a TecMag Apollo NMR console, a MITEQ low noise pre-amplifier and an AMT 1kW rf broadband pulse amplifier. The magnetic field is provided by a low-inductance superconducting solenoid coil with an inductance of 23 mH. This is cooled to liquid helium temperatures in a bath cryostat. The magnet system contains an integrated low temperature sample cryostat insert where sample cooling is provided by liquid helium supplied from the main helium Dewar through a needle valve and a capillary. The superconducting solenoid is connected permanently to a 15 VDC power supply with a maximum current of 160 A; this defines the maximum available magnetic field at the sample of 2.5 T. The instantaneous field is directly proportional to the instantaneous current and when the current is ramped at the maximum rated level, the field switching rate is 10 Ts^{-1} .

The probe is designed around a series resonant rf tank circuit adjusted to the selected NMR measurement frequency (36.8 MHz); this includes a cylindrical rf coil and series capacitor. A Cernox temperature sensor, whose resistance is effectively independent of field, is used in conjunction with a Lakeshore 331 temperature controller to measure the sample temperatures over the range 4.2 to 300 K with a stability of 0.05 K. Samples were usually studied in powder form and were sealed in glass 5mm NMR tubes for investigation.

In the low field dipole-dipole driven NMR experiments [22] and the dynamic tunnelling polarization experiments, a secondary broadband rf circuit was used to irradiate the sample. In the low field NMR pulse sequence, methyl tunnelling sidebands of the NMR spectrum were irradiated with this secondary rf. (Fig.3.5). In some variants of the experiment, the sample was irradiated with multiple frequencies in turn, designated stir and scan ω_{stir} and ω_{irrad} respectively.

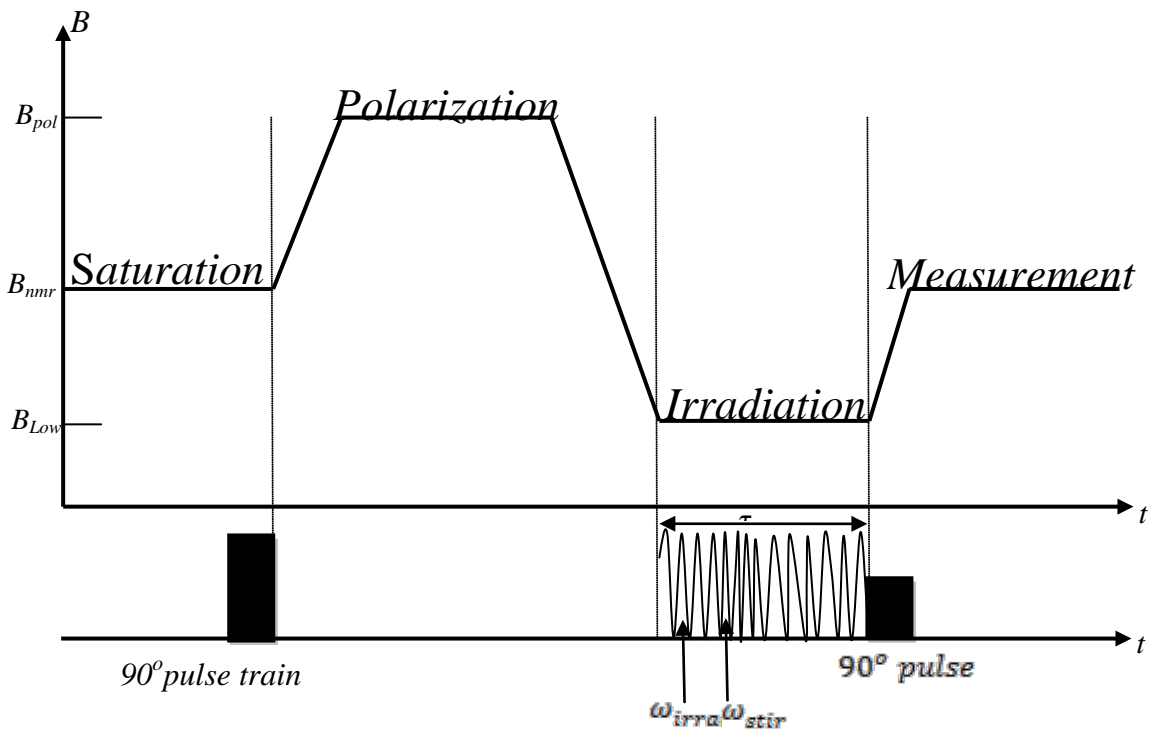


Figure 3.5: The low-field NMR pulse sequence uses secondary rf irradiation at low magnetic field B_{low} .

In the low field experiments the secondary rf irradiation circuit was centred on a broadband Helmholtz pair of coils surrounding the sample. This was in series with a 50 ohm high power resistor providing a broadband circuit with frequency range 0-5 MHz. A series relay connected at the top of the probe gave noise immunity during the NMR measurement phase. The circuit was powered by a secondary broadband 100W amplifier. The characteristic impedance of the complete circuit exhibited a plateau up to approximately 4 MHz, after which the impedance increased rapidly.

The NMR console supplied the rf signals for the primary NMR and secondary rf channels, as shown in Figure 3.6. It also supplied the 0 – 10 V DC signal that was used to control the main magnetic field via its power supply. The coil current and the supplied magnetic field were accurately proportional to this control voltage.

Spectrometry

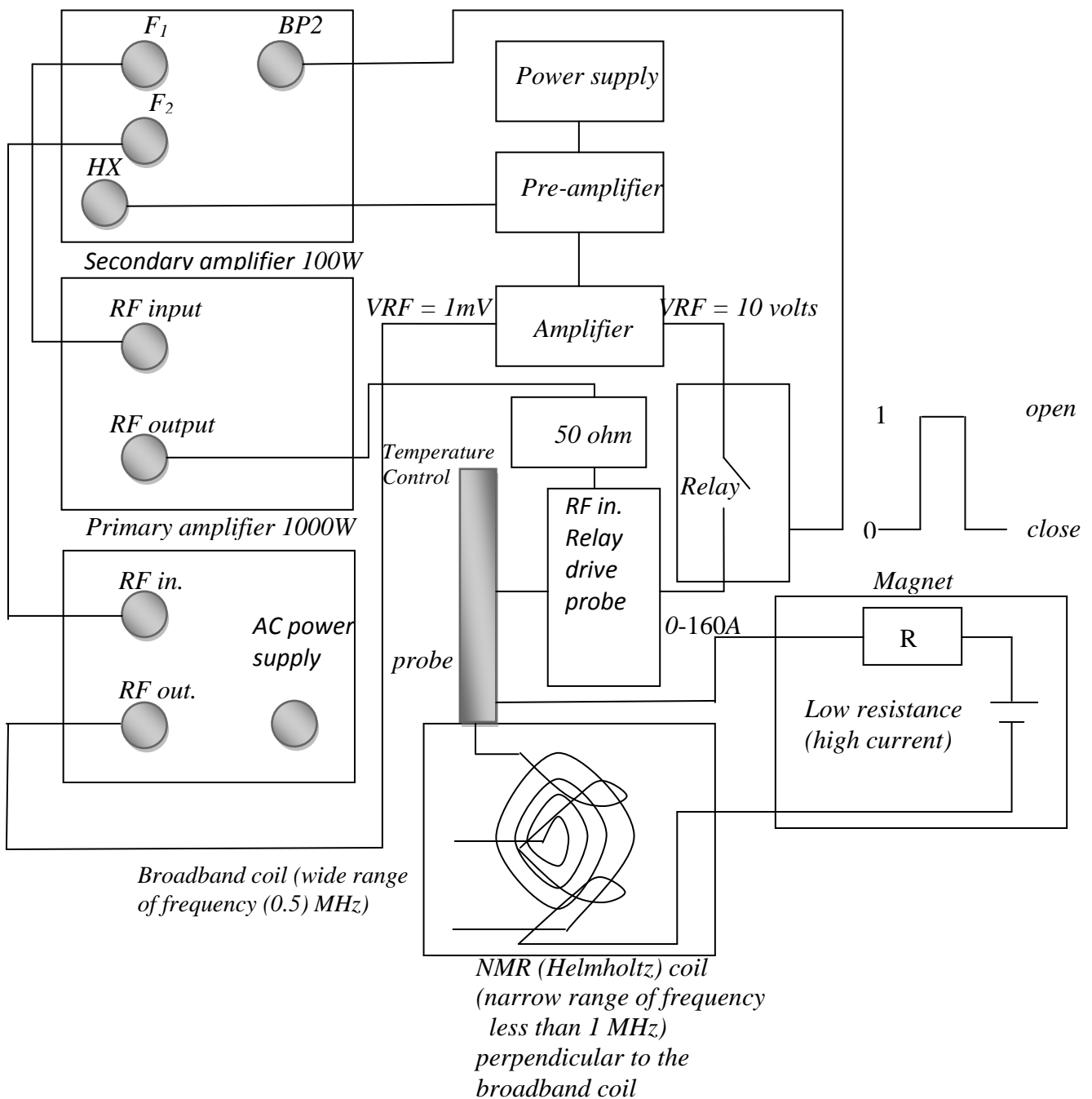


Figure 3.6: The NMR spectrometer.

3.4 Methods in data treatment: -

In our experimental low-field work we made a variety of data processing as it is summarised in the following treatments:-

1. In the DTP measurements pumping the tunnelling sideband transitions can lead to significant cooling of the tunnelling reservoir as well as heating, to the extent that a population inversion of the tunnelling reservoir is obtained. When tunnelling inversion occurs, the 1H magnetization measured in the final stage of the sequence will also be inverted. We can detect inverted Zeeman populations through the phase shift made after Fourier transformation of the FID. An 180° phase shift relative to the reference phase shift indicates the presence of population inversion. In Figs. 3.7 and 3.8 the point is illustrated for the $a+$ DTP sideband of 2-butanone (MEK).

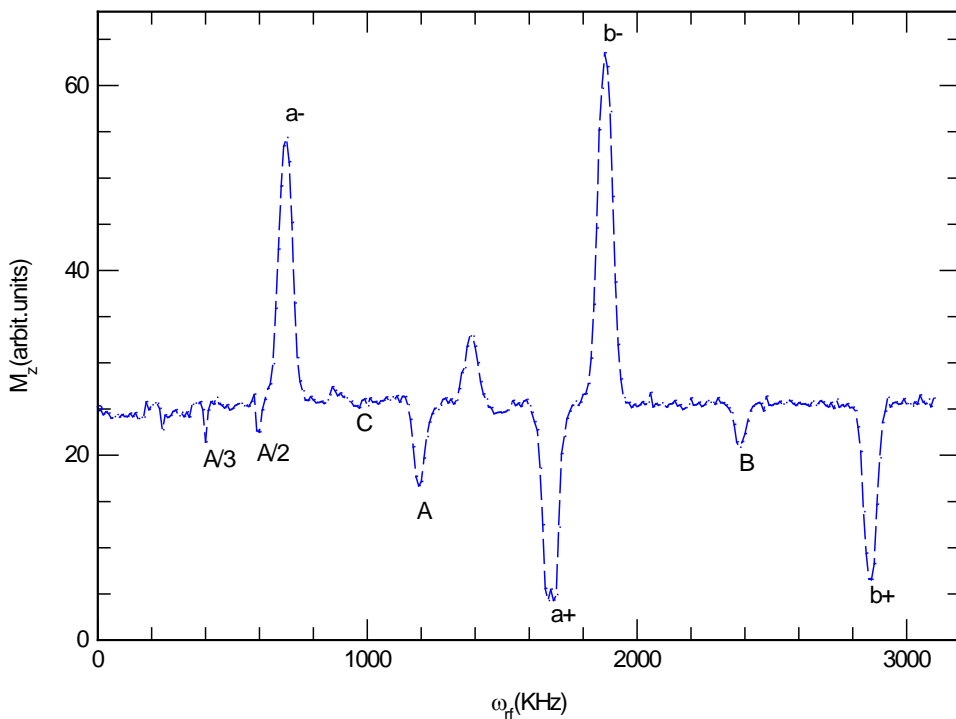


Figure 3.7: The new irradiation and level crossing fields DTP scan for MEK with polarization at 1 T for 270 s, irradiation at 290 G for 5 s and level crossing at 125 G for 2 s, with a group of an odd points at $a+$ which are phase shifted.

Fig 3.8 records the phase shift required to generate a pure absorption line shape and we notice that the phase changes systematically in the channel numbers 1670, 1680 and 1690. The phase shift is of the order 180° . Therefore, in the experiments to be described in chapters 4 and 5 the phase is monitored and where such abrupt phase shifts were observed, the 1H magnetization was multiplied by -1. The effect on the data is well illustrated for the $a+$ sideband in Fig. 3.9.

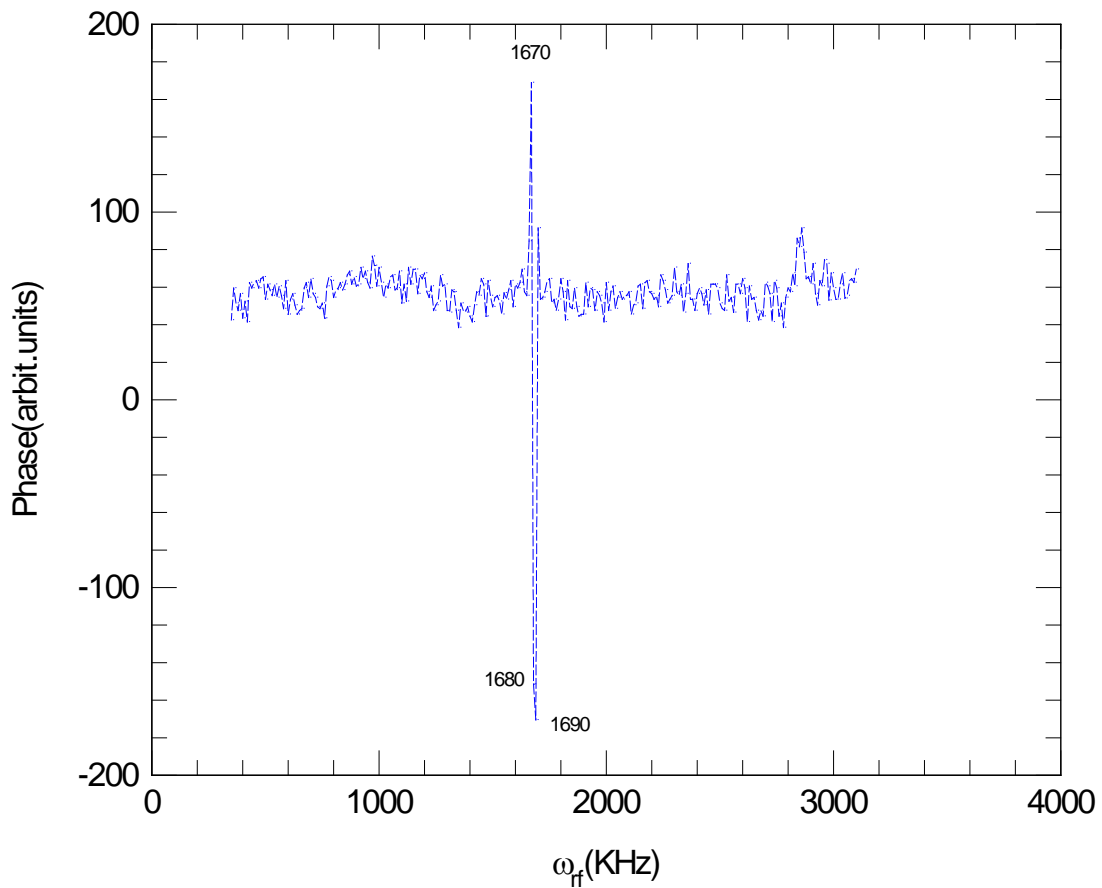


Figure 3.8: The phase of the NMR signal recorded in a DTP spectrum, showing the abrupt change in phase of approximately 180° degrees for three data points in the region of the $b+$ sideband.

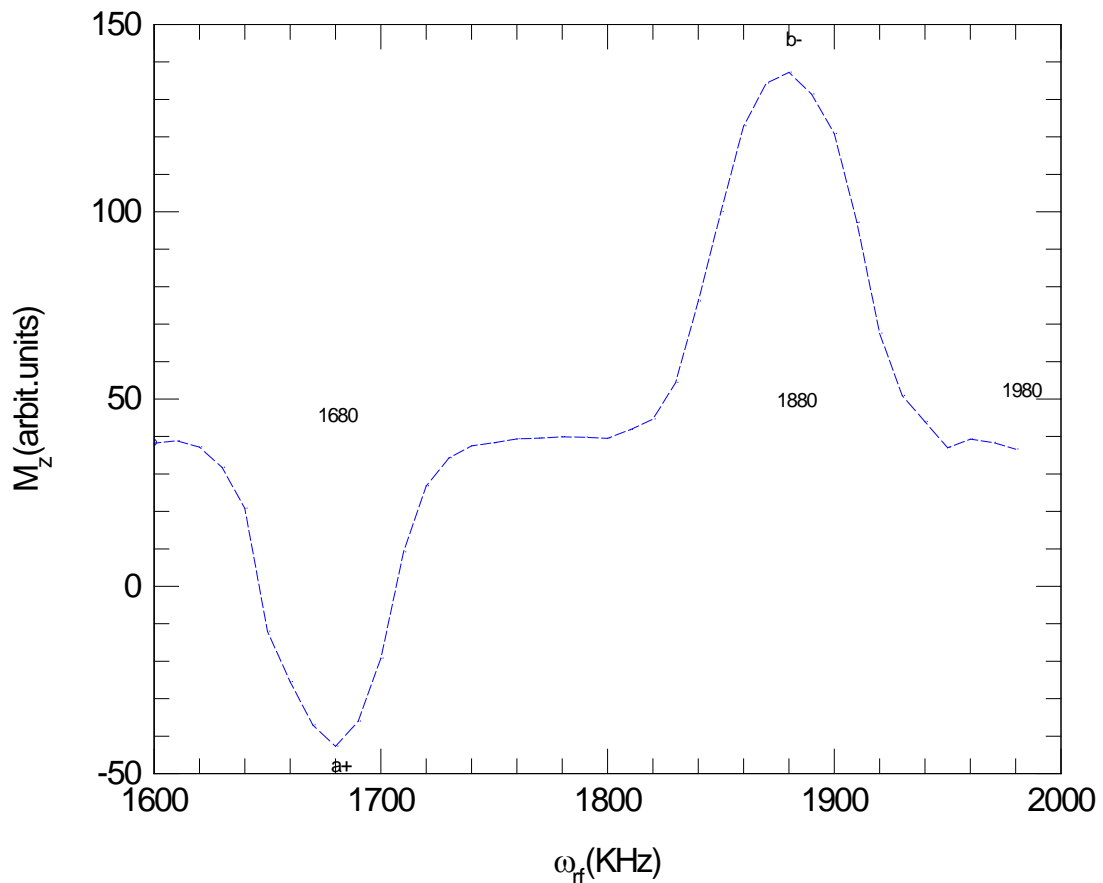


Figure 3.9: A phase adjusted DTP spectrum showing inverted polarization arising from inverted populations.

Notice also in the DTP spectrum of Fig. 3.9 how the baseline is not zero, despite the saturation of the 1H a short time before the final 1H magnetization measurement. This arises due to the finite switching time of the field-cycling magnet; there is spin-lattice relaxation during the time taken to switch the field during the final few steps in the sequence. Some baseline contributions were also observed to arise when the irradiation field was close to the level crossing region. Evidently here, due to the coupling between the Zeeman and tunnelling reservoirs, a small proportion of polarization is generally transferred to the Zeeman reservoir contributing to the background level.

2. A number of experiments were designed to measure the amplitude of a DTP sideband peak as a function of one of the experimental parameters, for example the Zeeman

polarization time or the rf irradiation time. For these experiments it would be too time-consuming to record the whole spectrum, therefore the DTP peak was sampled at the centre of the DTP peak and at two points either side of the DTP peak. An example is the DTP peak amplitude which is determined by taking the difference between the peak and the average of the baseline on either side. However, in this particular case shown, which monitors the $a+$ sideband, there is population inversion which appears in the corresponding phase shifts required to give a pure absorption line in the Fourier transformation. Making the appropriate sign corrections we arrive at the correctly behaviour of the $a+$ peak. Finally in Fig. 3.10 the amplitude of the $a+$ peak determined from this data is plotted as a function of the irradiation time, providing data on the transition probability.

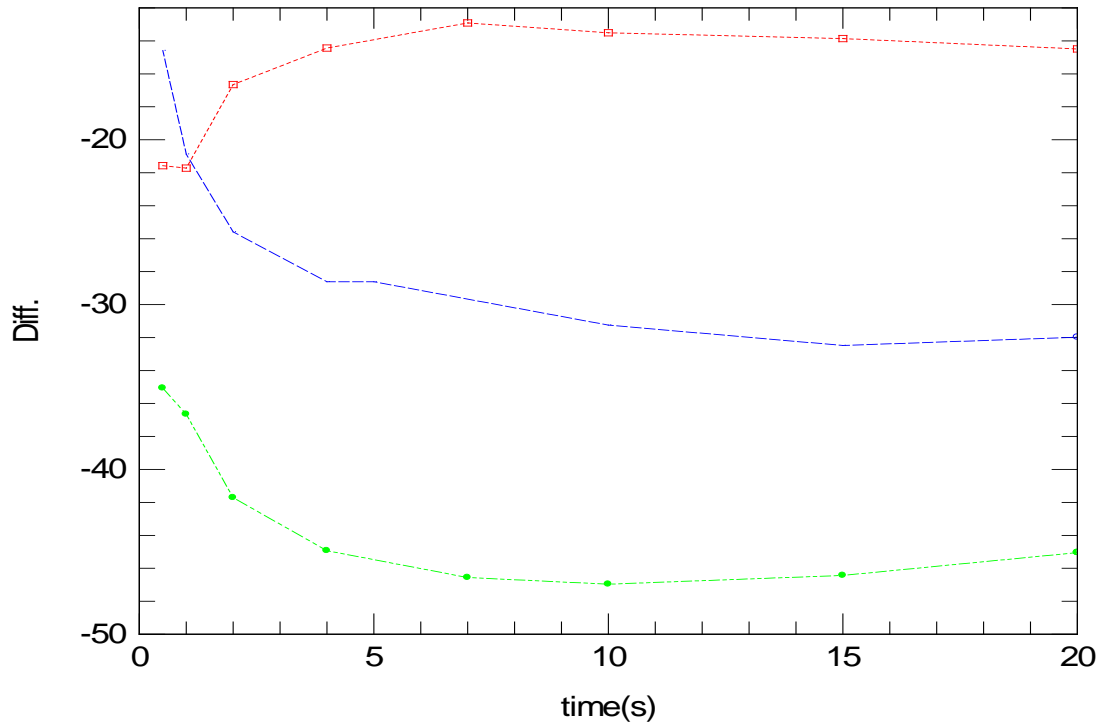


Figure 3.10: The difference between the peak and the average of the baseline for the curves which represent the changing of the irradiation time for the $a+$ peak at the 290 G irradiation field versus irradiation time, (before (□) and after (●) the phase correction), comparing it with the first 180 G scan for the $a+$,(○).

The NMR signal is proportional to the polarization and the magnetization; equivalently it is proportional to the inverse temperature T_z of the Zeeman reservoir and the applied field B .

$$\text{Polarization} \propto \frac{B}{T_z} \quad (4)$$

Following hardware processing in the NMR spectrometer, the NMR signal has arbitrary units. However, to gain a quantitative understanding of the DTP experiments there was a need to calibrate the NMR signal to enable it to be recorded as either a polarization or in units of inverse temperature (see equation above). The calibration could be determined by measuring the NMR at thermal equilibrium as will be illustrated in section 5.4. Since, under these conditions, the NMR signal is very large, steps had to be taken to avoid saturation of the pre-amplifier at the NMR probe head. A high-performance attenuator was inserted between the NMR probe and the pre-amplifier and the equilibrium NMR signals were recorded for a number of applied fields and attenuator values in the range 0 to 30 dB. The linearity of the attenuator and the attenuation setting was also checked with low level signals. Using this procedure a robust calibration of the NMR signal was obtained, enabling NMR signals in arbitrary units to be converted to inverse temperature units or polarization.

3. The RF coil calibration:-

There was a further calibration procedure required in order to obtain an accurate determination of the polarization from the raw NMR signals. The basic idea here is to correct the data for fluctuations in the measurement field. Due to the coil resonance characteristics, the amplitude of the NMR signal we observe is dependent on the field at which it is measured. To correct the data for field fluctuations we need to measure the coil resonance curve. Using the sample of acetophenone a polarization-recovery

experiment was conducted, where the sample is polarized for 30s at 1 T before the signal is measured as a function of an offset from the resonance field of 8495 G. The NMR absorption line was recorded as a function of field offset from -50 to +60 G in steps of approximately 5 G.

The experiment was repeated three times and the NMR signal amplitude was determined by integrating the NMR absorption line. The data is shown in Fig.3.11 where the *x*-axis represents the channel number (proportional to the NMR frequency in the rotation frame) and the *y*-axis represents the NMR signal amplitude.

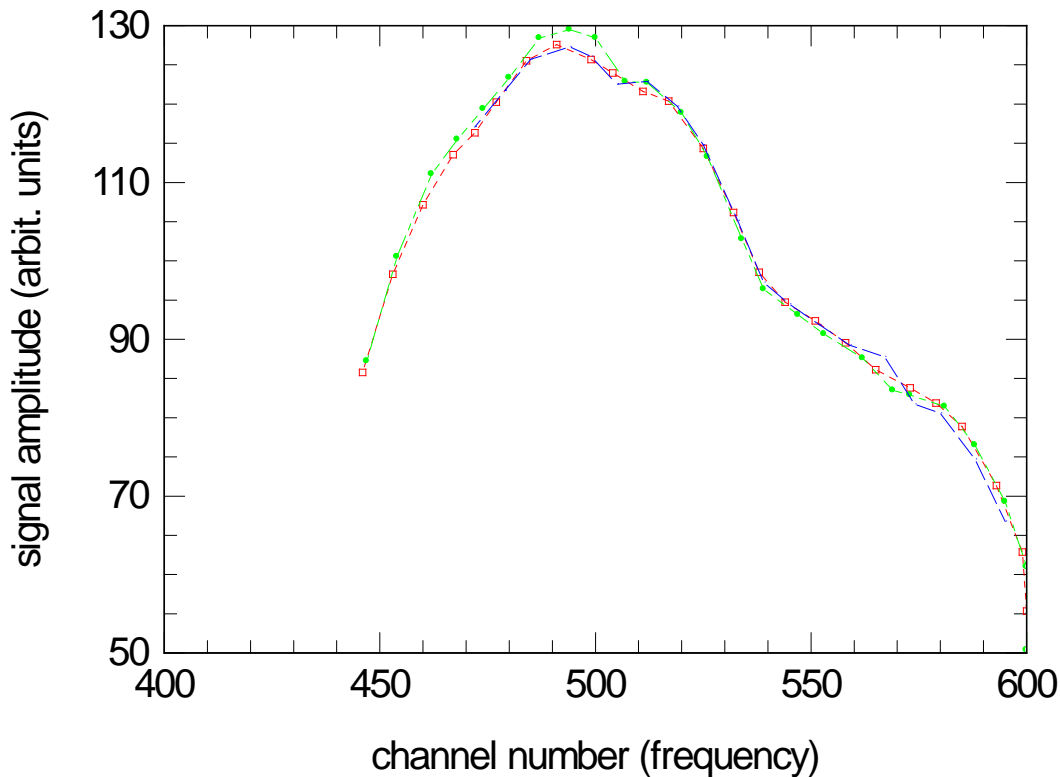


Figure 3.11: The rf coil calibration recorded on acetophenone with a polarization at 1T for 30 s and for three times, (1)(□), (2)(○), (3)(●).

Since the DTP experiments on 2-butanone and acetophenone were conducted at time intervals amounting to some months, and spectrometer functions were not necessarily stable over such time intervals, an rf coil calibration had to be recorded all at once.

Therefore, Fig. 3.12 shows the calibration for MEK.

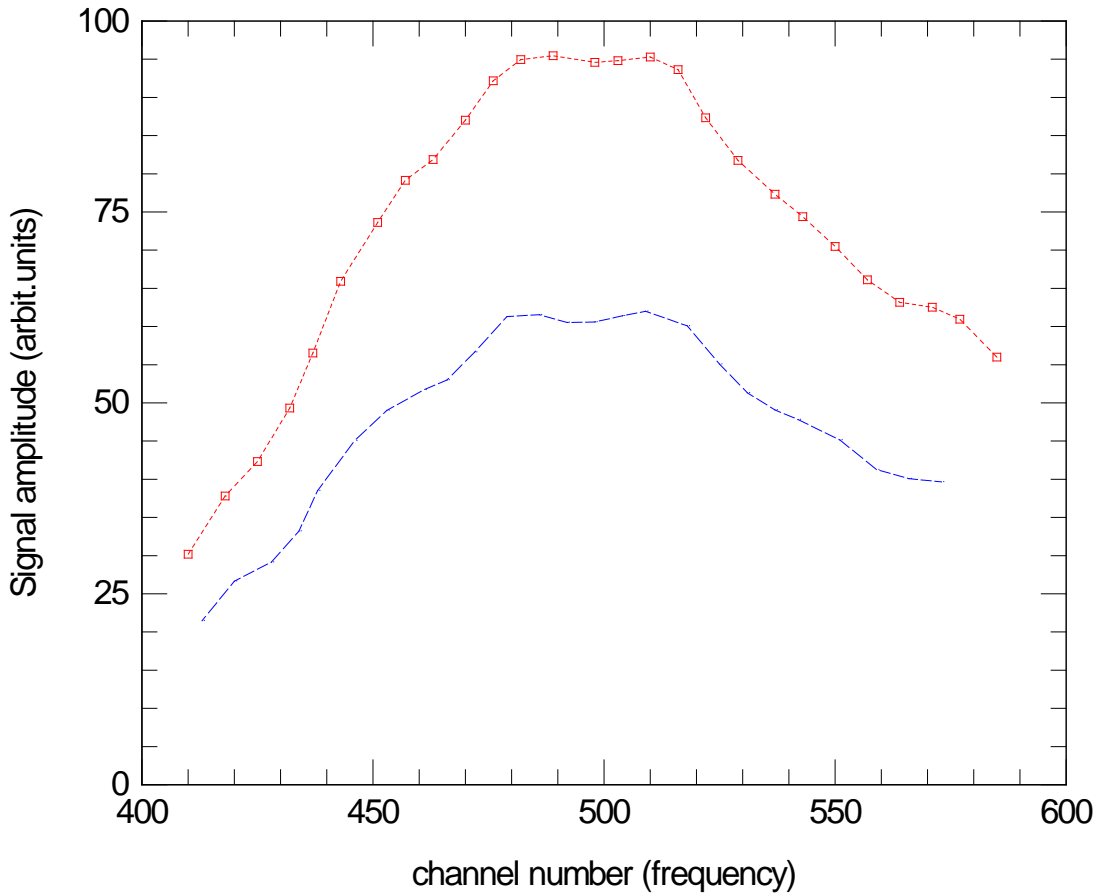


Figure 3.12: The rf coil calibration (MEK) with a polarization at 1 T for 10 s (□) and 5 s (○), where we notice that the signal does not change around a flat region at (500).

The rf coil calibration clearly shows the measuring apparatus is sensitive to the actual field at which the signal is recorded which appear on the NTNMR screen accompanied to the real part of the Fourier transform. In a field-cycling experiment this may vary by as much as 10 Gauss during an experimental run of many hours. The rf coil calibration curve is hence used to correct the NMR signal amplitudes measured. The shape of the calibration curve is determined by two factors, firstly the bandwidth of resonance curve that characterizes the rf tank circuit that includes the rf coil. Secondly, the rf pulse length imposes another bandwidth contribution to the curve – the Fourier transform of a pulse being a sine function determined by the inverse pulse width. Conveniently we notice that the signal amplitude does not change a lot around the region of 500 channel

number and it appears flat. Therefore, if the field is set to and stable in this region the field fluctuations do not require large calibration shifts.

In the field-cycling experiments the frequency of the centre of the NMR absorption line is routinely recorded as well as the integral of the NMR peak. Therefore, this data was used in the correction of the NMR signals for field-cycling induced drifts in measurement field, using the rf coil calibrations shown above. As an example, spectra which have been had systematic corrections applied for field fluctuations are shown in Fig. 3.13; a significant benefit of the procedure is the reduction in random scatter in the data points.

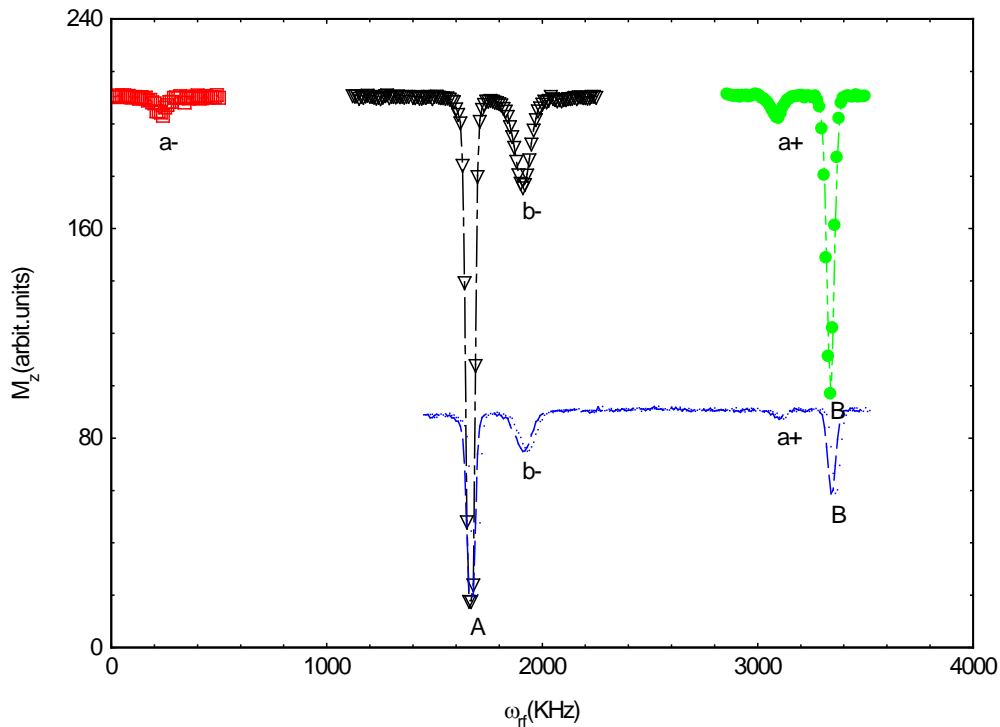


Figure 3.13: The conventional low field scans corrected for measurement field fluctuations that will be noticed in Figure. 4.2.

Chapter 4 Dynamic Tunnelling Polarization: Acetophenone

In this chapter we shall describe novel experimental techniques for enabling the tunnelling polarization to be determined. These have been developed for the first time as part of this thesis. The new experiment sequences rely on two concepts; a) to drive with low frequency rf irradiation at low applied magnetic field, ‘forbidden’ transitions that involve changes in tunnelling state, b) to transfer the tunnelling polarization that is created to 1H Zeeman polarization at a level crossing. The latter arise at specific B -field values in the manifold of tunnelling-nuclear magnetic energy levels.

4.1 The conventional low field scan and Dynamic Tunnelling Polarization

4.1.1 Conventional low field scan:-

The first dipole-dipole driven low-field NMR experiments used in the study of methyl tunnelling were reported by Clough *et al* in reference [23] in 1985. A typical pulsed NMR sequence is shown in Fig. 4.1 and following initial saturation of the 1H spins, begins with preparation at high field, B_{pol} , where the 1H Zeeman system is polarised during a time interval, τ_{pol} . The applied field is then ramped to a low value, B_{low} , whereupon the sample is irradiated with rf of frequency ω_{rf} . During this period τ_{low} any transitions that are resonant with ω_{rf} are driven, changing the populations of the tunnelling-Zeeman manifold and hence the tunnelling and Zeeman polarizations. The sequence concludes with a field ramp to the NMR resonant field where the 1H magnetisation is measured with a 90° pulse.

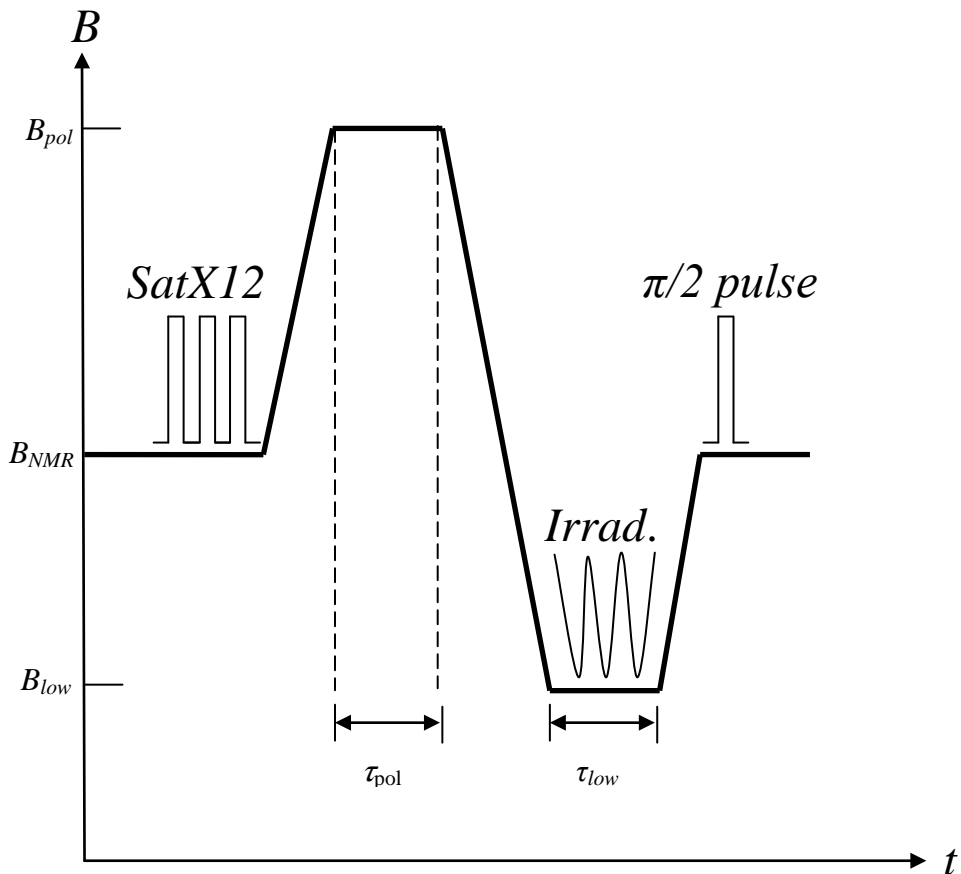


Figure 4.1 A pulsed NMR sequence for dipole-dipole driven low-field NMR.

In this experiment, tunnelling sideband transitions are observed in addition to pure $\Delta m = \pm 1$ and $\Delta m = \pm 2$ NMR lines. The tunnelling sidebands are labelled and appear with frequencies as follows: (a₊ and a₋: $\omega_t \pm \omega_L$); (b₊ and b₋: $\omega_t \pm 2\omega_L$). Sometimes a sideband of $\Delta m = 0$ appears at ω_t ; this is labelled C, as shown in the energy level diagram Fig.2.3.

These transitions appear as inverted peaks because the ¹H polarization created at high field is partially destroyed by the rf irradiation when it is resonant with an NMR lines (A,B) or a tunnelling sidebands (a-, a+, b-, b+).

A spectrum recorded on a sample of acetophenone is shown in Fig. 4.2. This data was recorded with a temperature of $T=4.2\text{K}$ and with the applied field $B_{NMR} = 0.8495\text{T}$. The tunnelling sideband and NMR transitions are identified, where two spectra are shown at first we make the scan to show the (A, b-, a+, B) peaks for a polarization time

of 30 s and then we make a full scan (a -), A , b -), $a+$, B) but at a higher polarization time 120 s, where we notice the difference of increasing the Zeeman magnetization for a higher polarization time. This spectrum repeats published data on acetophenone [22] and from the sideband frequencies we confirm that the specific tunnelling frequency is $\omega_t = 1.424 \pm 0.002$ MHz.

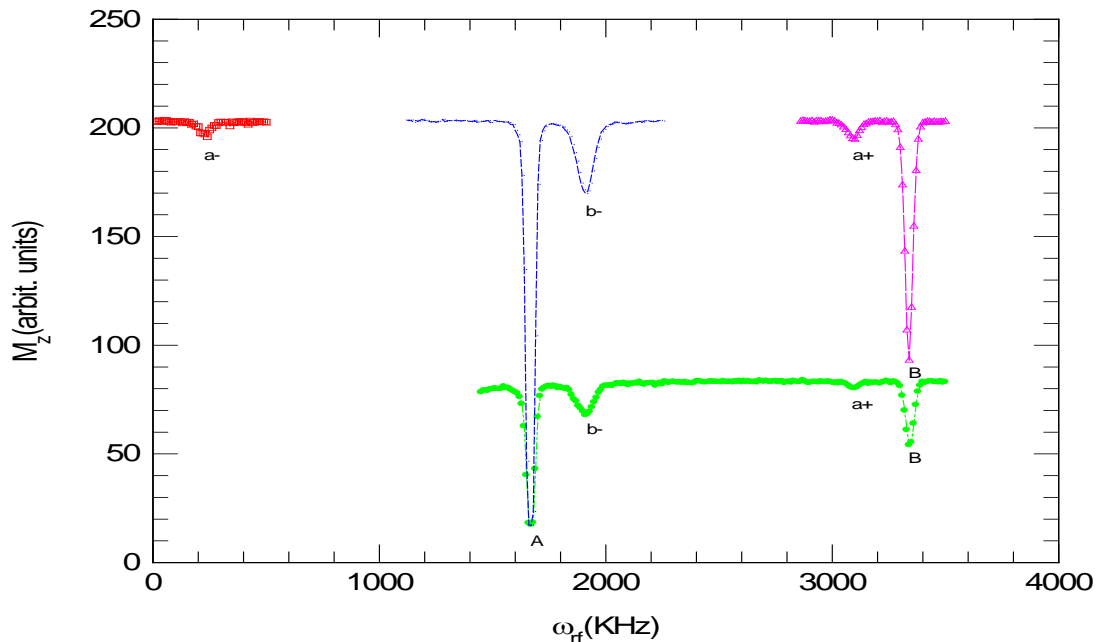


Figure 4.2 Conventional low field NMR scans on acetophenone, recorded with $T=4.2$

K and applied field $B_{NMR} = 0.8495$ T. The initial polarization was carried out at

$B_{pol} = 1$ T for $\tau_{pol} = 30$ (●), 120 s (□, ○, △). The rf irradiation time is $\tau_{low} = 5$ s at

$$B_{low} = 180$$
 G.

4.1.2 Dynamic Tunnelling Polarization:-

According to elementary modelling, the ($A \rightarrow E$) and ($E \rightarrow A$) transitions give rise to positive and negative changes in the temperature of the tunnelling reservoir respectively. However to observe these changes we have devised a step in the low field pulse sequence to make contact with the saturated Zeeman reservoir at a level crossing. In this way we can use a measurement of the proton 1H magnetization to record the tunnelling polarization produced by rf irradiation.

4.1.2.a The revised pulse sequence is shown in Figure 4.3, where, as with conventional low-field NMR, this sequence begins with polarization of the 1H system after the saturation step at high field to get a large magnetization of the spins. This is followed by rf irradiation of the tunnelling sidebands which has the effect of transferring polarization from the Zeeman reservoir to the tunnelling reservoir. We then saturate the 1H system so that when we reach the level crossing and we bring the Zeeman and tunnelling reservoirs into contact, the polarization of the tunnelling reservoir is transferred to the Zeeman reservoir. At the end it is measured by a measurement pulse as in Fig.4.3; i.e. we measure the tunnelling polarization through the Zeeman polarization. This gives us an insight and a good view of how the reservoirs inside the system behave and how the energy transfers between them so we can control and manage these processes. It also facilitates a full understanding of the structure and the existence of the energy reservoirs in these materials.

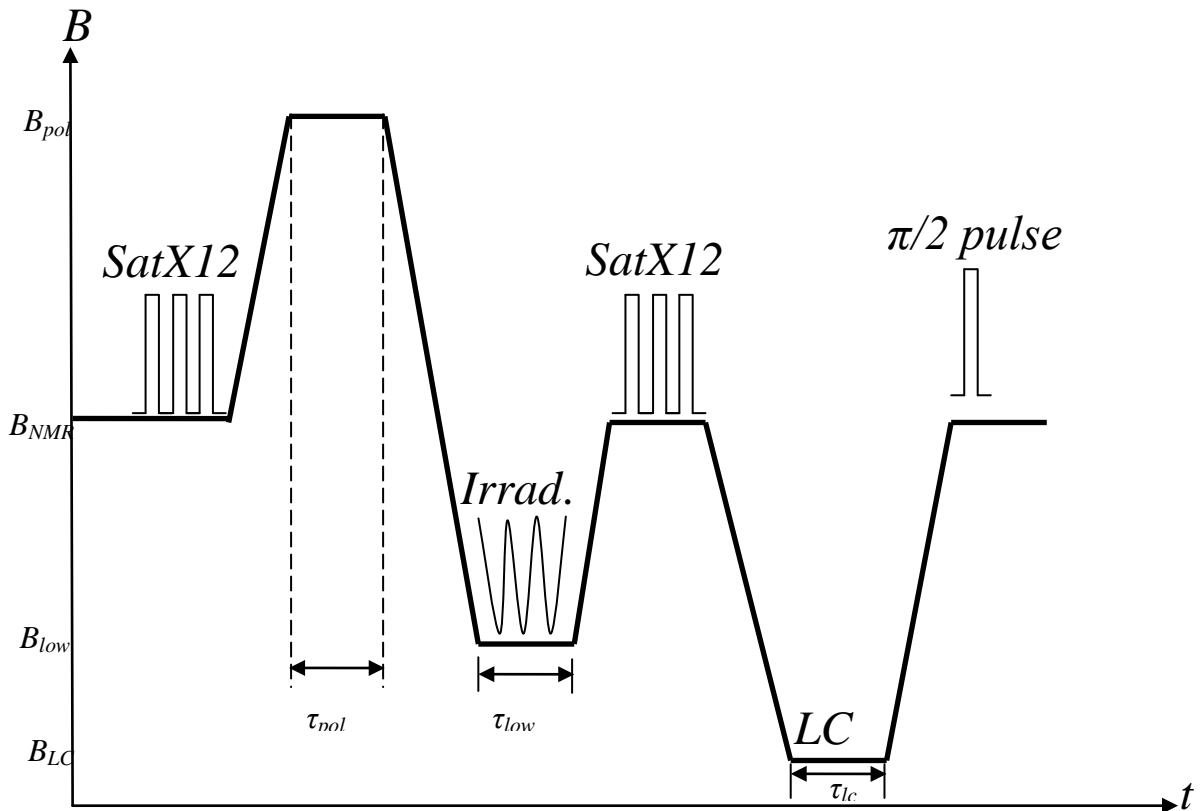


Figure 4.3: The tunnelling polarization pulse sequence

Applying this new sequence to acetophenone only to the region of the *b*- peak for a polarization time of 30 s the spectrum in Fig.4.4 was recorded. This was the first observation of the effect. A conventional low-field dipole-dipole driven spectrum of the *b*- peak is shown for comparison (polarization time 30 s). More significant scans will be discussed with our work progression in the next sections.

The y -axis is the ^1H magnetization but because it was created by bringing the saturated ^1H spins into level crossing contact with the tunnelling reservoir, it is a direct measure of the tunnelling polarization. In Fig 4.5, DTP spectra are shown for acetophenone. Both positive and negative peaks are observed. The rf irradiation of the *a*- and *b*- sidebands give rise to a net $E \rightarrow A$ conversion and hence reveals a cooling of the tunnel reservoir. The rf irradiation of the *a*+ and *b*+ sidebands gives rise to a net $A \rightarrow E$ conversion and hence a heating of the tunnel reservoir. In fact the latter also demonstrates that the populations of the *A* and *E* tunnelling levels have been inverted so that the tunnelling system is characterized by a negative tunnelling temperature. We

shall later describe how the y-axis can be calibrated in units of inverse temperature but firstly we shall investigate how the spectrum responds to changes in the experimental variables. Before doing so however, note the $b+$ sideband is not clearly recorded in the experimental spectrum although it is expected this should appear as a negative peak; its absence is explained because the bandwidth of the secondary irradiation coils is insufficiently broad and the circuit impedance is increasing significantly at rf frequencies above approximately 3.5 MHz.

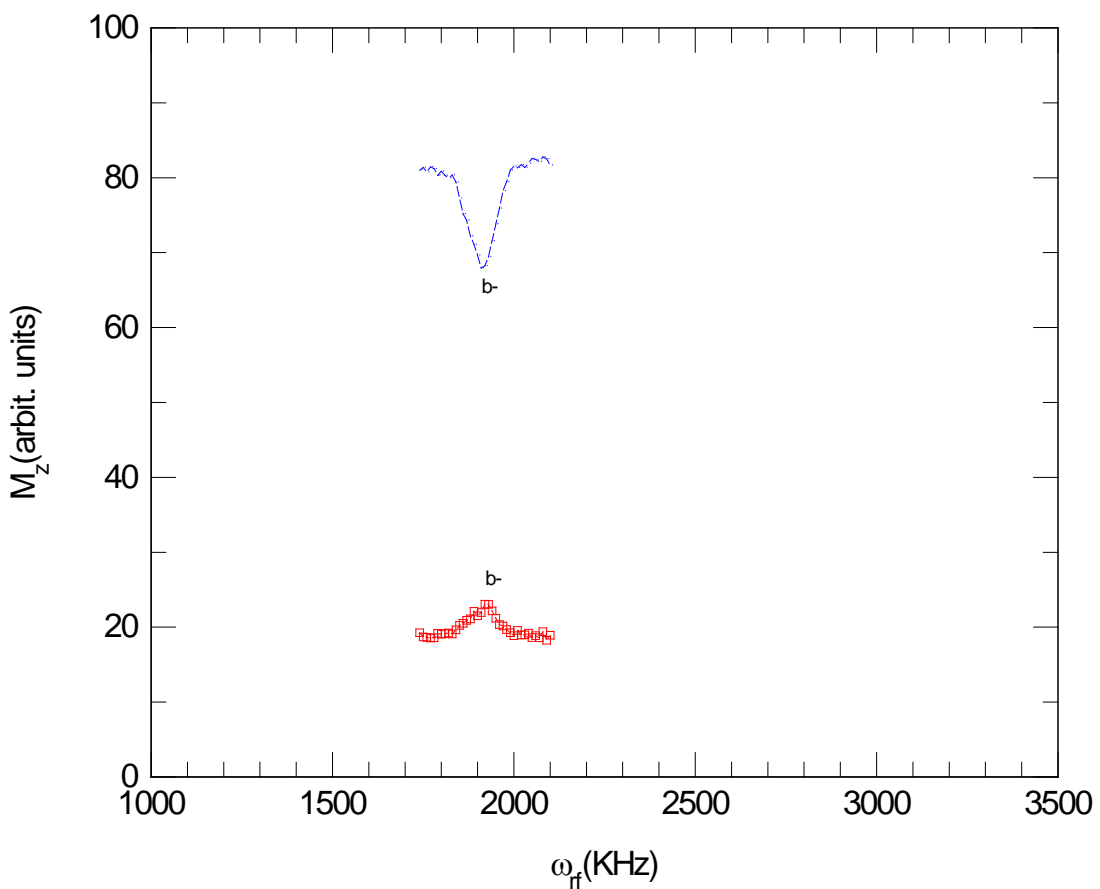


Figure 4.4: The conventional low field (○) and Dynamic Tunnelling Polarization (□).

4.1.2.b Using the dynamic tunnelling polarization pulse sequence, we studied the effect of increasing the polarization time from 30 to 60 s and larger values where we get a high magnetization M_z as shown in Fig.4.6, where we also notice that there is no significant appearance of the ($b+$) peak which is expected in the region $\omega_{rf} = 4.77$ MHz.

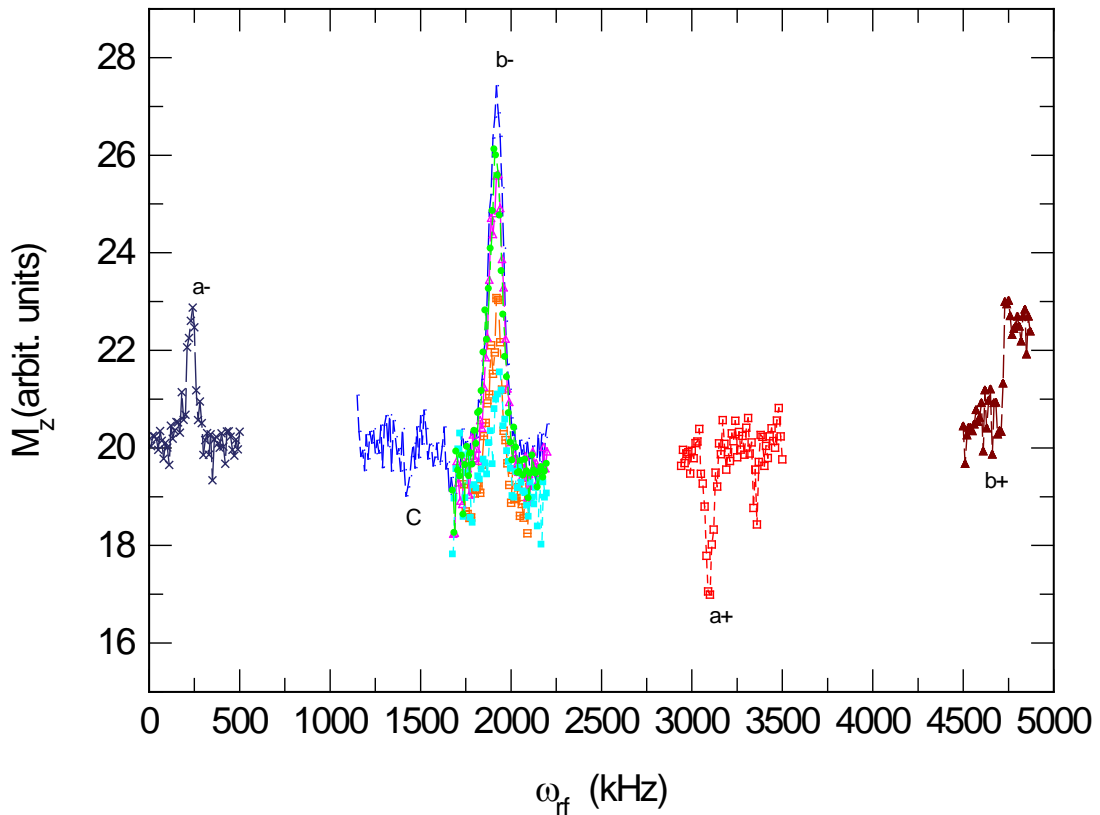


Figure 4.5: The effect of increasing the polarization time from 30 (\square) to 60 s (\blacktriangle , \square , \circ , \times) at 1 T with irradiation for 5s and changing of the level crossing field values (170, 340, 350, 380) G (\blacktriangle , \bullet , \blacksquare) for 2s.

And we studied the effect of changing the level crossing field for the b- region from 340 G to 350 and 170 G where we notice that it has approximately the same magnetization value as in Fig.4.5, while at 380 G we see in the same figure a big decrease in the magnetization value.

This fact gives us a hint that the level crossing does not happen at a specific field value and we must investigate how the level crossing field values change the amount of magnetization that we obtain.

4.1.2.c Also changing the polarization time from 60 to 120 s, employing the dynamic tunnelling polarization pulse sequence, to study the big effect on increasing the depth of

the peaks, but this effect does not help to solve the problem of the lack of good appearance of the $b+$ peak which still continues in this scan as in Fig.4.6.

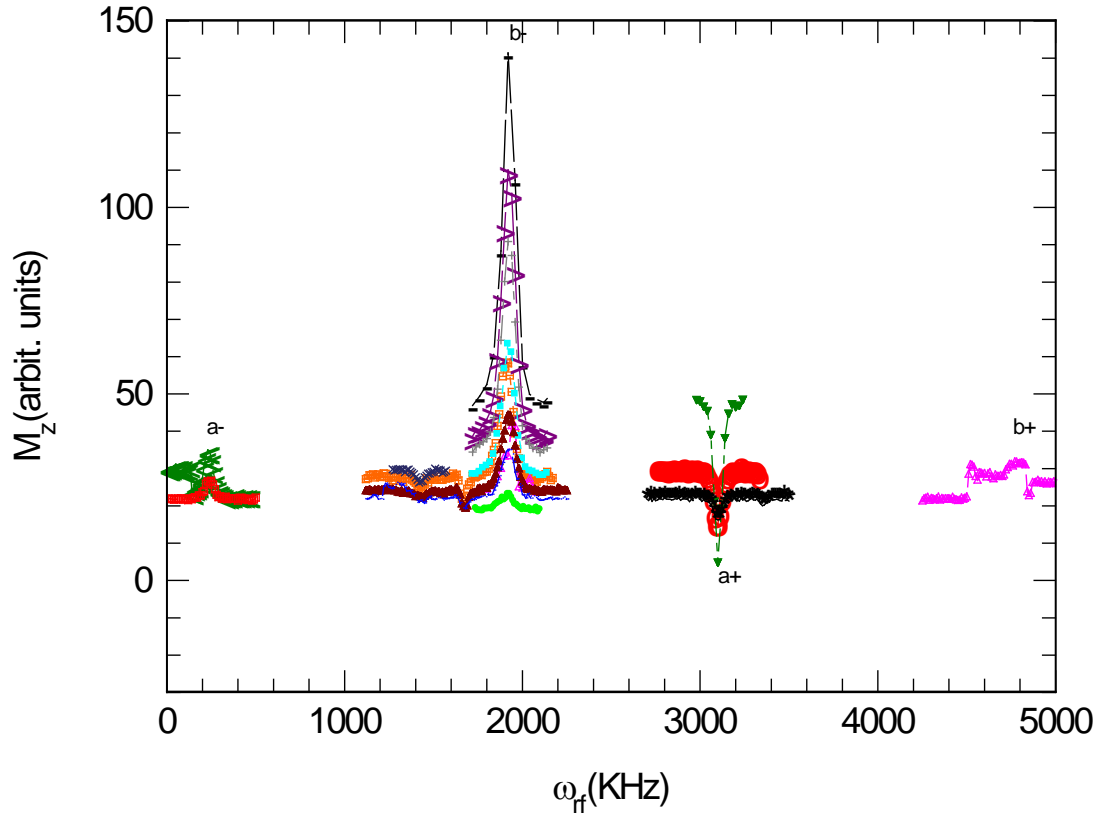


Figure 4.6: The effect of increasing the polarization time at 1 T in the steps of 30 s (●), 120 s (○, □, *, △), 200 s (▲), 400 s (■, ○, ×, □, <), 800 s (+), 1200 s (>) and 2400 s (-, ▼). In the same figure we see how the increase of the polarization time (200, 400, 800, 1200, 2400) s for the $b-$ peak has a good effect of increasing the magnetization value also for the $a+$ peak for a polarization time 2400 s.

Finally we repeat the same scan we made for the $b-$ at 400 s but for the entire spectrum including two separate scans, one for the $b-$ and C and the other for the C peak, only to comparing this to the first 30 s scan as shown in Fig.4.6, using the dynamic tunnelling polarization pulse sequence.

Where we notice an increase in the magnetization and a very good appearance of the peaks .

Relating the DTP peak amplitude of the *b*- peak at different polarization times we get

Fig.4.7.

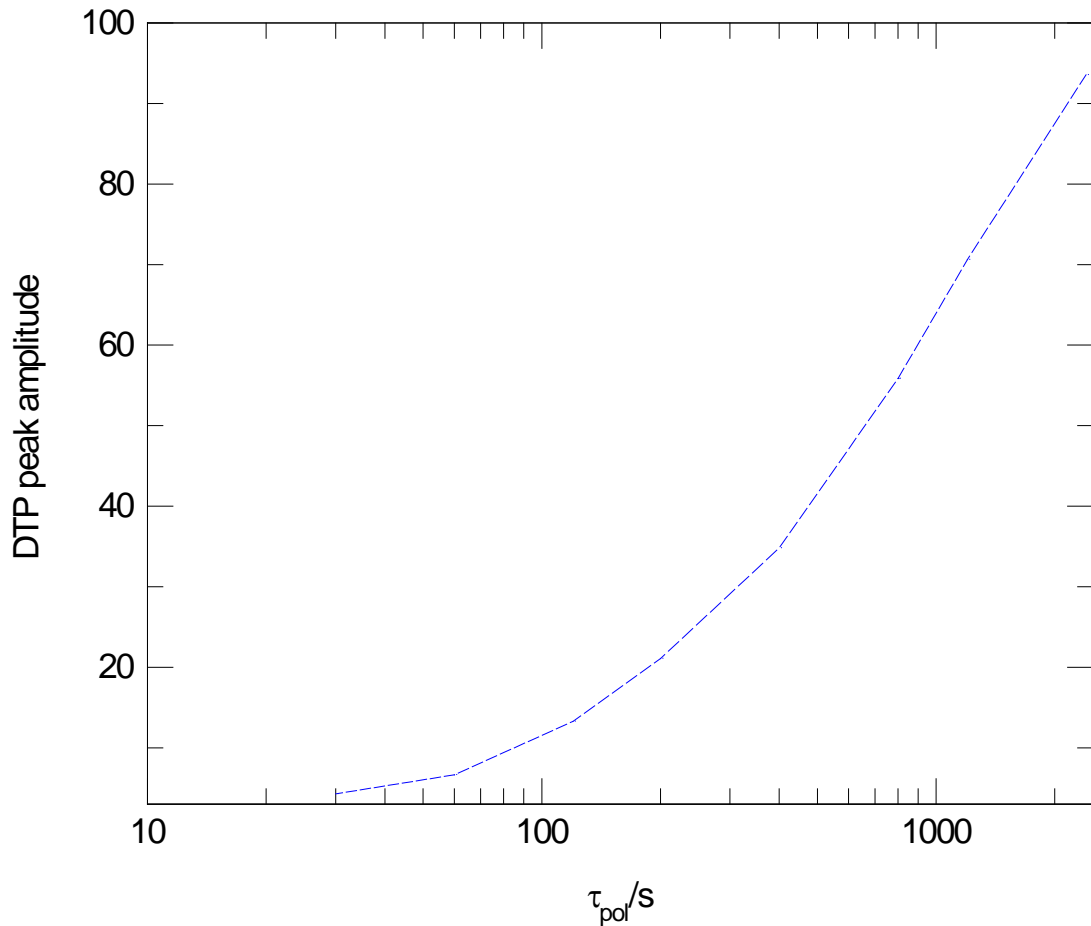


Figure 4.7: The effect of increasing the polarization time on the DTP amplitude of the *b*- peak.

We notice that the DTP magnetization amplitude of the *b*- peak increases with polarization time increasing.

4.1.2.d For the *a+* baseline we make an experiment to make sure we had saturated the proton 1H reservoir, using the dynamic tunnelling polarization pulse sequence, of increasing the number of saturation pulses to 30, as in Fig.4.8, compared with what we obtained previously for 12 pulses in Fig.4.6.

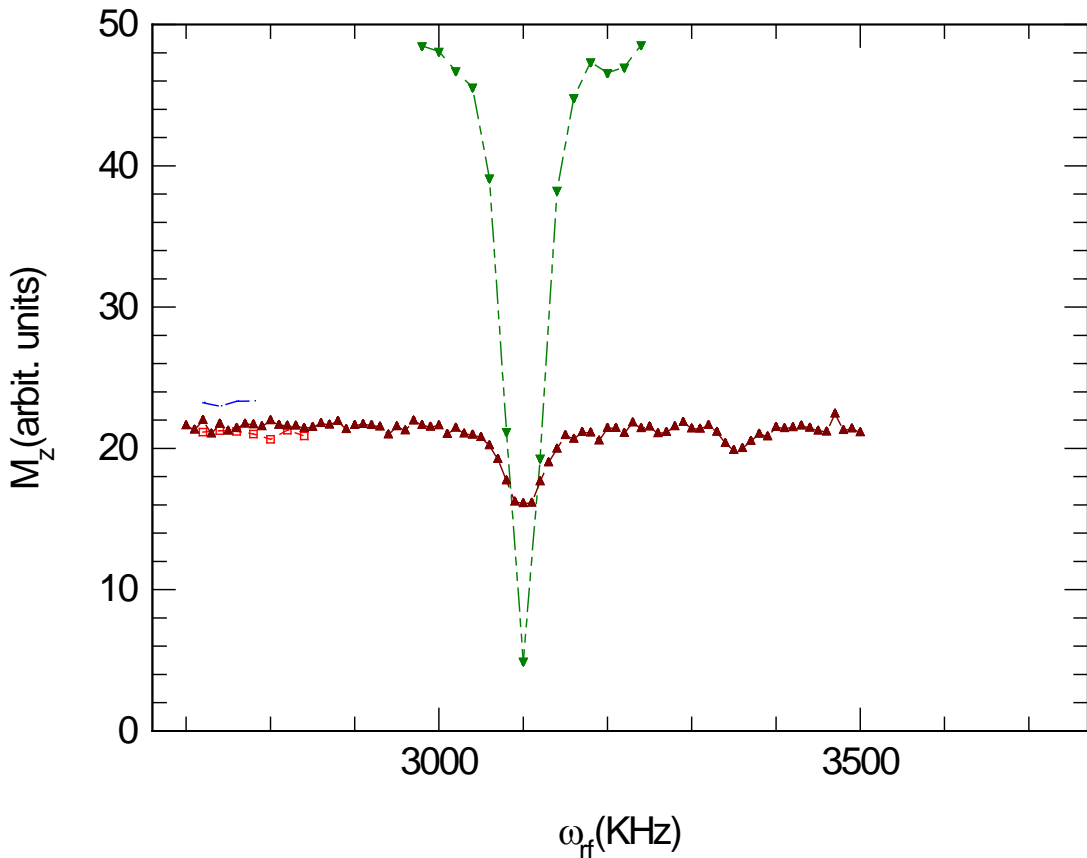


Figure 4.8: The effect of increasing the number of saturation pulses from 12 (\blacktriangle , \blacktriangledown) to 30 (\square , \circ) for $a+$ peak polarized at 1 T for the times (120, 2000) s (\square , \blacktriangle , \circ) comparing it with (2400) s (\blacktriangledown).

Where we discover that there is no difference, and by increasing the polarization time to 200 s for 30 s saturation pulses we notice an increase in the magnetization which is a result of increasing the polarization time and not to increase the number of the saturation pulses.

4.2 The effect of changing the irradiation time in the b -region:-

All the experiments we did in section 4.1 were at a 5 s irradiation time, but now we will try to investigate the effect on the magnetization of changing the irradiation time in the b -region. Polarization times of 120, and 200 s were employed within the dynamic tunnelling polarization pulse sequence. This experiment gives us the potential to measure the transition probability of the b -sideband.

1. Firstly we changed the irradiation time to the following values (0.1, 0.5, 1, 2, 5, 10, 20) s with a 120 s polarization time.
2. Secondly we changed the irradiation time to the following values (0.1, 0.5, 1, 2, 5, 10, 20) s with a 200 s polarization time.
3. Finally in order to obtain a measurement of the DTP peak amplitude the difference between the peak and the baseline average was calculated. The data are shown in figure 4.9.

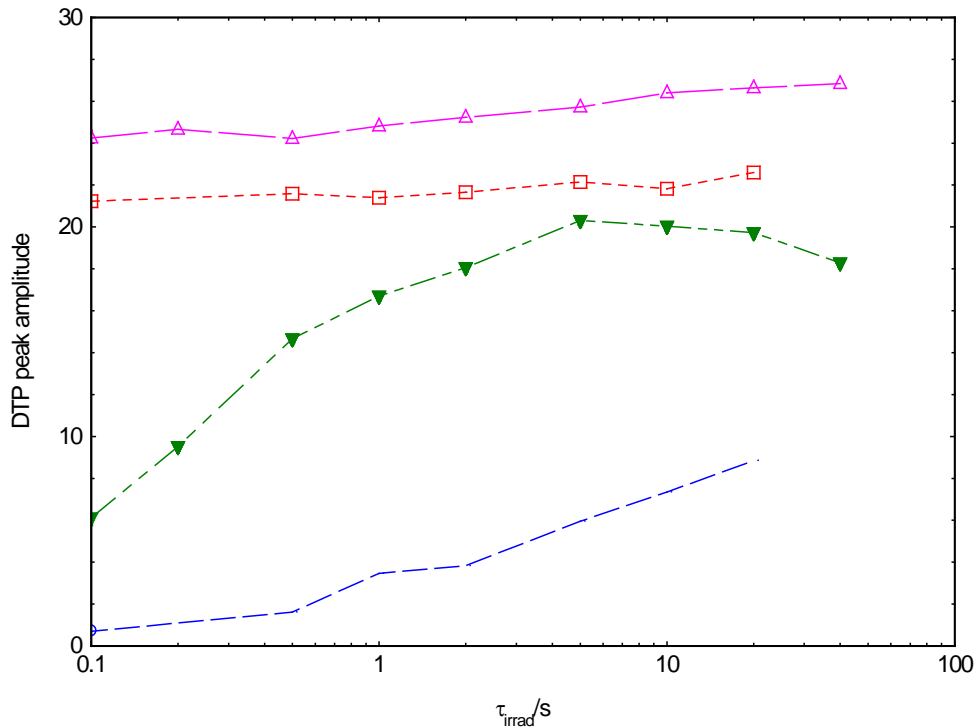


Figure 4.9: The DTP peak amplitude (\circ , \blacktriangledown) with baseline average (\square , Δ) as a function of the irradiation time in the b -region. Polarization times are 120 and 200 s respectively. We notice for both of them that the difference increases as the time increases as a result of increasing the magnetization. Also we have a constant value for the baseline magnetization as we increase the irradiation time, as shown in Fig.4.9.

4.3 The effect of changing the level crossing delay time in the b- region:-

In this series of experiments we wanted to find out how quickly the tunnelling and Zeeman reservoirs equilibrated at the level crossing, i.e. the speed and efficiency of the coupling between the Zeeman and tunnelling reservoirs at a level crossing. The sample was first polarized at 1 T for 200 s, then the field was switched to low field 400 G where rf irradiation with frequency ω_{rf} was applied for 5 s to drive the changes in tunnelling and Zeeman polarization. Following saturation of the Zeeman system the level-crossing contact was made. The DTP peak amplitude was studied as a function of time spent at the level crossing with values (0.1, 0.5, 1, and 2) s.

The difference between the peak and the average of the baseline is plotted as a function of time spent at the level-crossing in Fig. 4.10. We notice an increase in magnetization from 0.1 to 0.5 to 1 s and then this saturates at the 2 s measurement.

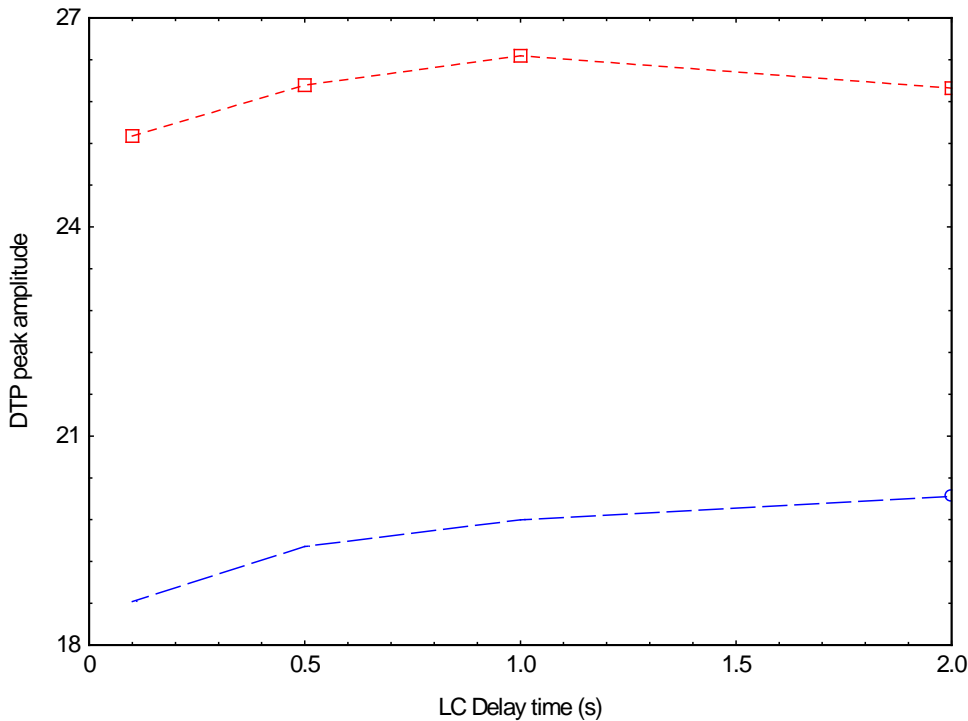


Figure 4.10: The DTP peak amplitude (difference) (○) and baseline average (□) versus the level crossing delay times (0.1, 0.5, 1, 2) s.

This means that the process of level crossing which has the goal of bringing the Zeeman tunnelling reservoirs into contact is effective and has fully equilibrated after 1 s. The main conclusion from Fig.4.10 is that the reservoirs equilibrate quickly, on a timescale faster than we can switch the B -field. Hence we conclude from Fig.4.10 that a 2 s contact time is more than enough to fully equilibrate the two reservoirs.

4.4 The level crossing spectrum

As we mention in Sec 4.1.2, especially in item b the study of the level crossing is important since the value of the magnetization we get depends on what level crossing field we use. In this section we investigated the spectrum of the level crossing region. To achieve this, a series of experiments were made of the b - DTP peak amplitude as a function of the level crossing field, which was varied in the range from 40 to 400 G. For all experiments the polarization field was 1 T and the polarization time 600 sec. The rf irradiation time is 5 s at the low field 405G which drives the b - sideband. Saturation of Zeeman magnetization and measurements of Zeeman polarization were conducted at the resonance field of 8600 G. We notice from these figures that by changing the level crossing field there is no big drop when changing the field either side of the level-crossing condition which means that there is a connection between the Zeeman and tunnelling reservoirs even if we are away from the exact level crossing field value. Therefore the interaction region is broadened. The level-crossing spectrum is plotted by taking the difference between the peak and the average of the baseline as in Fig.4.11.

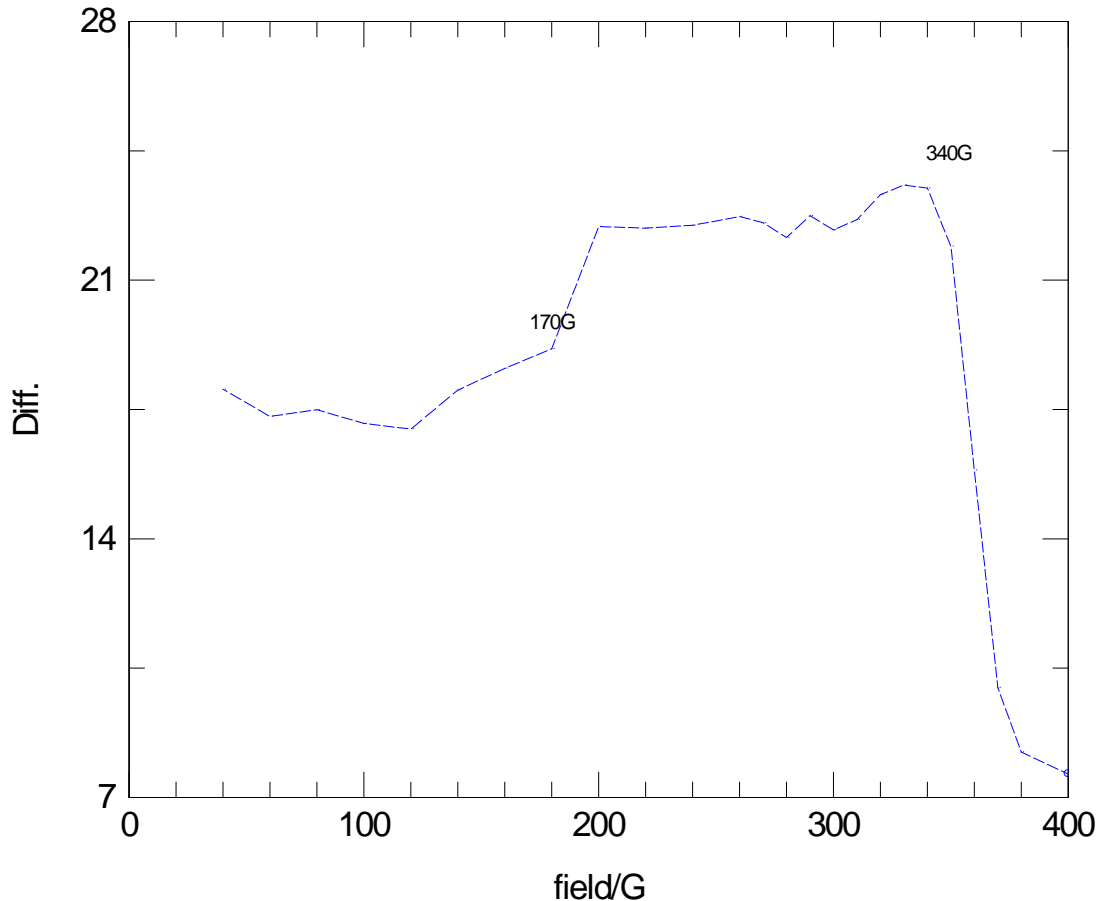


Figure 4.11: The difference between the peak and the average of the baseline versus the level crossing field value in the b -region.

With tunnel frequency 1.424 MHz, the level crossing at $\omega_t = \omega_L$ is expected when the applied field is 340 G. What we notice is that there are two level crossing peaks at ($\omega_t = 0.712 \text{ MHz} = 167 \text{ G} \approx 170 \text{ G}$, $\omega_t = 1.424 \text{ MHz} = 334 \text{ G} \approx 340 \text{ G}$), where the second is double the first, and also there is a stable region between them, so to go from 340 to 170 G you must pass through this stable region.

What we observe in Fig.4.11 is a big step as we approach the level crossing from the high field direction, then we see a plateau and it does not change much until 170 G. The reason for this plateau is clear; we have to pass through the first level crossing at 340 G to get to the lower fields. The equilibration of the reservoirs is so efficient so we will always see a large signal, even when the set LC field is lower. There is a step down in

signal at 170 G and this may arise because the relative heat capacities of the Zeeman and tunnel reservoirs are different at the lower field, affecting the temperature to which they come to equilibrium.

To explain this we must refer to the theoretical fact that since we have one methyl group we expect to get two level crossing peaks resulting from the transition between A and E energy levels ($A_{-3/2}$ to $E_{+1/2}$) and ($A_{+3/2}$ to $E_{-1/2}$) as shown in Fig.2.3 which represent the ($\omega_L = \omega_r/2 = 170\text{G}$) case as shown in Fig.2.15. The other set of transitions is (($A_{-3/2}$ to $E_{-1/2}$) and ($A_{-1/2}$ to $E_{+1/2}$), ($A_{+3/2}$ to $E_{+1/2}$) and ($A_{+1/2}$ to $E_{-1/2}$)) as shown in Fig. 2.3 which represents the ($\omega_L = \omega_t = 340\text{ G}$) case as shown in Fig. 2.15.

So the peak at 340 G appears because we have at 340 G a transfer of energy from tunnel to Zeeman reservoirs until the system reaches the equilibrium state when both of the reservoirs have the same energy, which appears as a stable region in Fig.4.11, and this continues until 170 G where a transfer of energy from the Zeeman to tunnel reservoirs happens which causes the drop in level of the plateau and the appearance of the 170 G peak. We notice that we observe the baseline signal even when we have only just a second or two earlier saturated the magnetization. This is because we irradiating with rf outside the level crossing region, but close to it. It must be close enough to a level crossing such that there is still some weak overlap of the levels so that irradiation changes weakly the A and E populations. This is not a resonance effect, so it is independent of rf frequency and we get a level baseline that is higher than zero.

4.5 The tunnelling relaxation time

Here, and differently from what we did in a previous section, we try to make a determination of the exact value of the field that will bring the tunnelling reservoir into equilibrium, and we achieve this by disturbing the tunnel resonance away from equilibrium, and observing its recovery. This can be achieved by inserting a 'relaxation

time' interval between rf irradiation at low field and saturation using a new pulse sequence as shown in Fig. 4.12.

1. We start by trying 8 kG as the tunnel relaxation field value [step(1)],

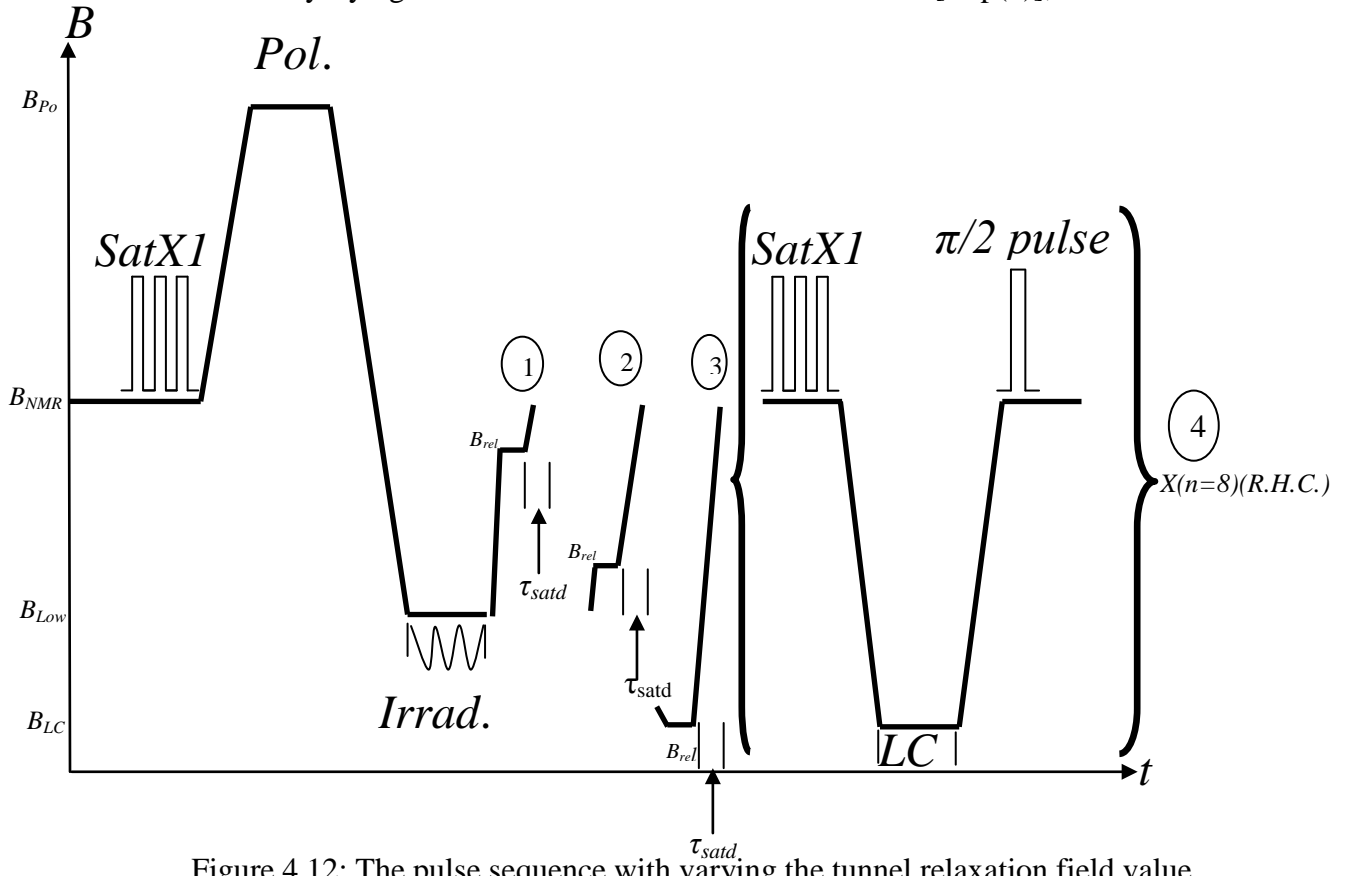


Figure 4.12: The pulse sequence with varying the tunnel relaxation field value.

where we polarize the system at 1 T for 600 s and irradiate it at 405 G for 5 s, using 8600 G as a saturation and measurement field with level crossing at 340 G, reaching it by a 2 s delay, and we vary the saturation delay time τ_{satdel} between 2 and 600 s, and by plotting the difference between the peak and the average of the baseline as shown in Fig.4.13.

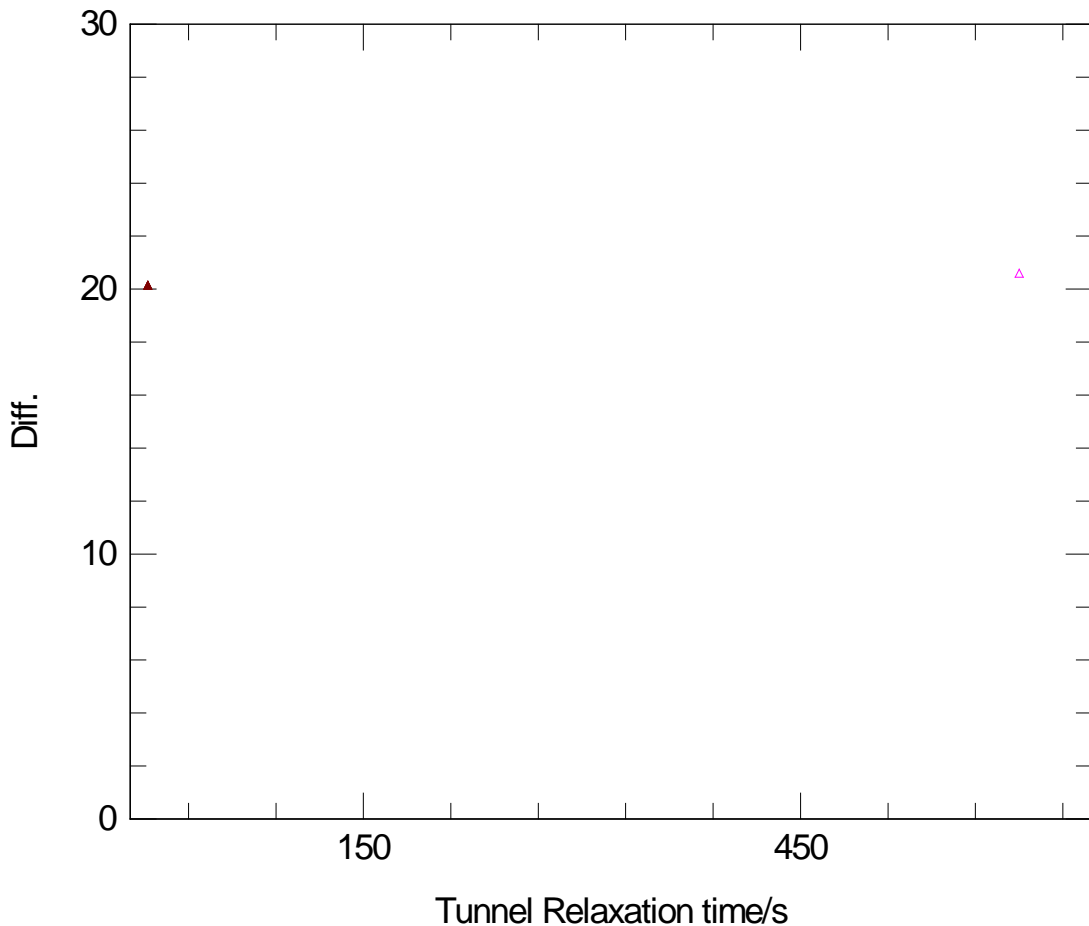


Figure 4.13: The difference versus time of saturation delay time 2 s (▲) and 600 s (▲) for 8 kG as the tunnel relaxation field value.

We notice that both 2 and 600 s have the same value of the difference which means that there is no tunnelling relaxation after 600 s at 8 kG, so we try another field.

2. Secondly we use 450 G as the tunnel relaxation field value as shown in Fig.4.12 [step(2)], and using the same setting as in the first item we vary the saturation delay time between (0.5, 1, 3, 8, 20, 40, 70, 100, 200, 400, 1000, 2000, 3600, 6000, 10000) s, and by plotting the difference between the peak and the average of the baseline, and the average of the baseline only as shown in Fig.4.14.

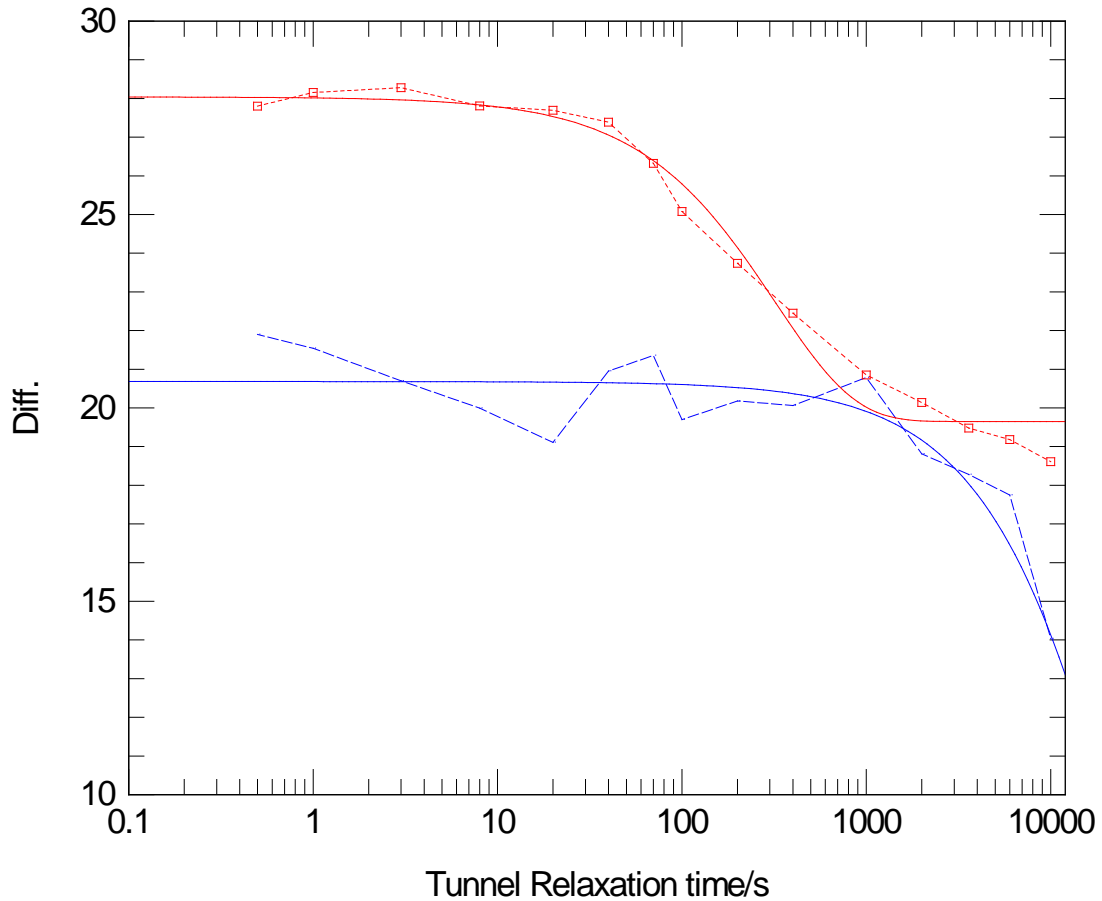


Figure 4.14: The difference (\circ) versus time of saturation delay time (0.5, 1, 3, 8, 20, 40, 70, 100, 200, 400, 1000, 2000, 3600, 6000, 10000) s for 450 G as the tunnel relaxation field value and the average of the baseline (\square), and we fit both curves to the equation

$$y=a \cdot \exp(-x/b) + c \text{ shown as solid lines.}$$

We notice that at 450 G there is very little relaxation, so even after 10000 s the tunnelling reservoir retained polarization as can be seen from the stable behaviour of the 450 G curve. This tells us that the tunnel relaxation has very slow relaxation process to the lattice and this because we are outside the level crossing region which means that there is no connection between the Zeeman and tunnel reservoirs as shown in Fig.4.15.

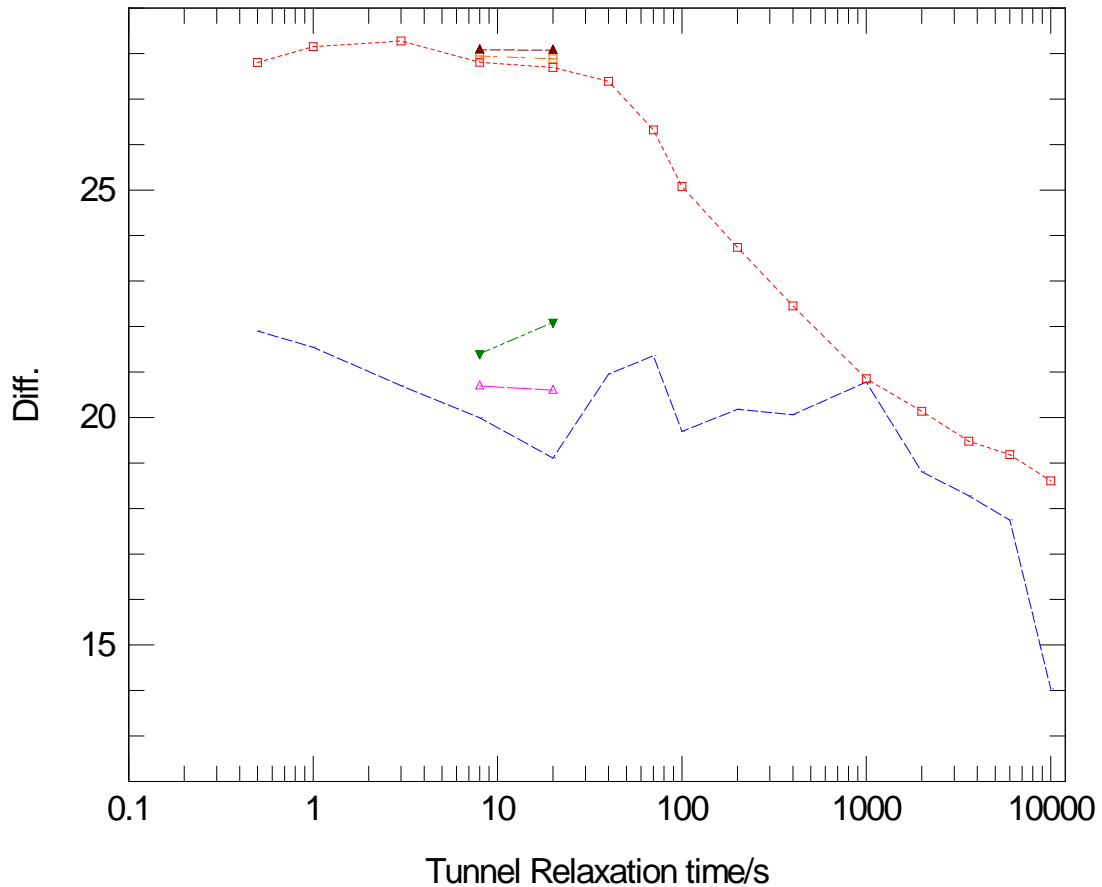


Figure 4.15: The difference (Δ , ∇) versus time of saturation delay time 8 and 20 s for 450 G as the tunnel relaxation field value and for the average of the baseline (\blacktriangle , \square). 3. Finally we use 340 G as the tunnel relaxation field value as shown in Fig. 4.12 [step(3)], and using the same settings as in the first item, and we vary the saturation delay time between (0.5, 1, 3, 8, 20, 40, 70, 100, 200, 400, 1000, 2000, 3600) s as shown in Fig. 4.16, and by plotting the difference between the peak and the average of the baseline, and the average of the baseline only as shown in Fig. 4.16.

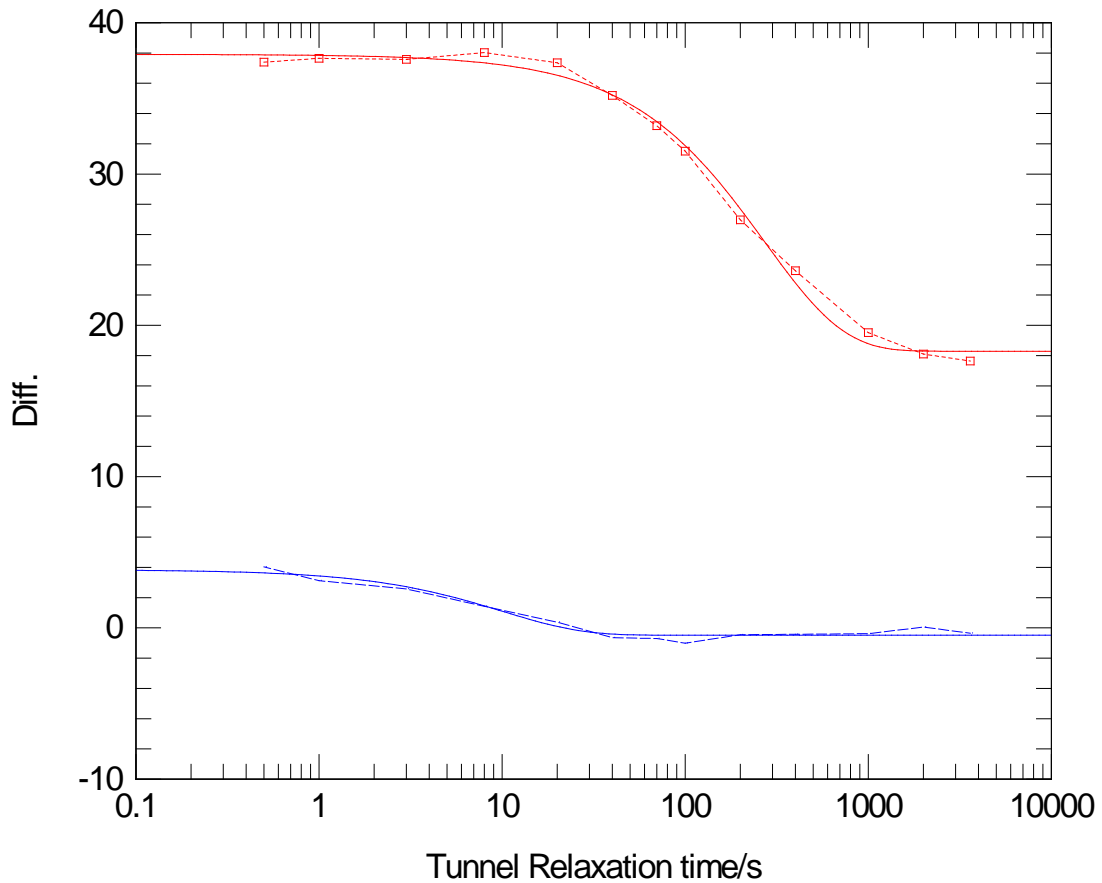


Figure 4.16: The difference (\circ) and the average of the baseline (\square) versus time of saturation delay time ($0.5, 1, 3, 8, 20, 40, 70, 100, 200, 400, 1000, 2000, 3600$) s for 340 G as the tunnel relaxation field value, and we fit both curves to the equation $y=a^* \exp(-x/b) + c$ shown as solid lines.

We notice that at 340 G there is a relaxation, so after 3600 s the tunnelling reservoir lost polarization as you see from the decreasing behaviour of the 340 G curve. This tells us that the tunnel relaxation has very fast relaxation process during one hour to the lattice and this because we are inside the level crossing region which means that there is a connection between the Zeeman and tunnel reservoirs and they are coupled, while outside the level crossing region it will take more than one day.

We fit all 340 and 450 G curves to an exponential decay equation where the parameters represented are (a) the amplitude of the peak, (b) the tunnel relaxation time s and (c) is just an offset representing the value required to bring the system to equilibrium. We

notice that for the difference curves of 340 and 450 G both (a and b) are increased and this means especially for the term $(I/b) \text{ s}^{-1}$, which represents the tunnel relaxation rate, that for 340 G we have an approximate big tunnel relaxation rate ($I/b = 1/10 \text{ s}^{-1}$) and this because there is a level crossing coupling and the tunnel reservoir will relax faster, while for 450 G we get an approximate small tunnel relaxation rate ($I/b = 1/5 \times 10^7 \text{ s}^{-1}$) so it will relax with a longer time because there is no level crossing coupling between the Zeeman and tunnel reservoirs and (a) will approximately increase from 4.3 to 3.2×10^4 . Opposite to this (c) will approximately decrease from -0.5 to -3×10^4 . And for the baseline curves of 340 and 450 G, (a) will approximately decrease from 19.6 to 8.3 and (b) will approximately increase from 272 to 321 in a similar behaviour to the difference curves $(I/b) \text{ s}^{-1}$ ratio, and (c) will approximately increase from 18.3 to 20. So we notice that there are alternative behaviours of (a and c) parameters where for 340 and 450 G difference curves, when (a) increases (c) will decrease and opposite to this for 340 and 450 G baseline curves, when (a) decreases (c) will increase.

4.6 The relative heat capacities of the Zeeman and tunnel reservoirs

We can perform an experiment to determine the relative heat capacities of the tunnelling and Zeeman reservoirs by making repeated contact. We make a relative heat capacity measurement by adding 8 level crossing and measurements steps to the pulse sequence in Fig.4.12 [step(4)], where we polarize the system at 1 T for 600 s, and for a long time 3600 s to get a large signal and irradiate it at 405 G for 5 s, using 8600 G as a saturation and measurement field with level crossing at 340 G, reaching it by 2 s delay, and using a tunnel relaxation field of 8000 G since we do want to relax the system and also we make the saturation delay time 2 s. We make the measurements at the frequencies 1810 and 2010 kHz (off resonance) and 1910 kHz (on resonance) as shown

in Fig.4.17, where we fit the curves to an exponential equation decay to give the decay factor (b) for the heat capacity.

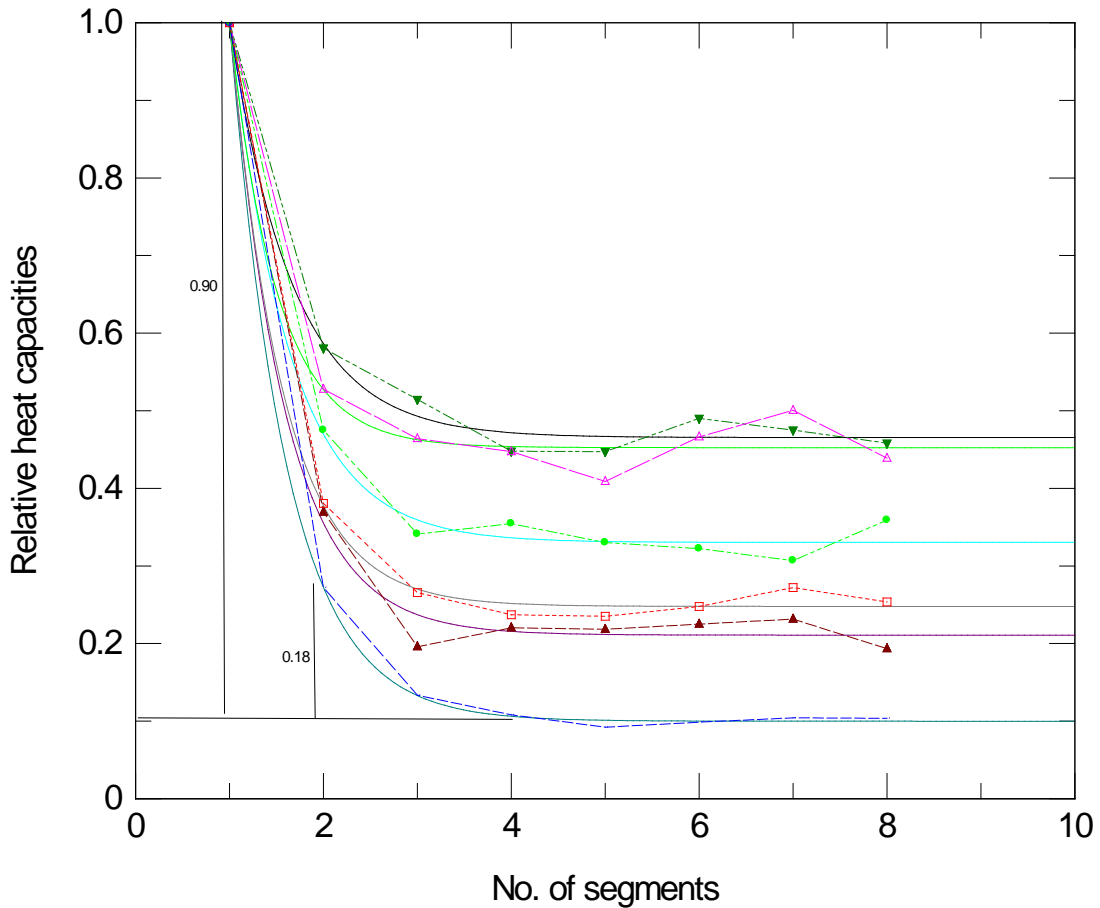


Figure 4.17: The relative heat capacity measurements at the frequencies 1810 and 2010 kHz (off resonance) and 1910 kHz (on resonance) at polarization times 600 s (Δ , \blacktriangledown , \blacktriangle) and 3600 s (\square , \bullet , \circ) respectively, and we fit all curves to the equation $y=a*\exp(-x/b)+c$ shown as solid lines.

We notice from Fig.4.17 that always the curves for 600 s are in top of the figure while the 3600 s curves are in the lower part of the figure for all frequencies (1810, 1910, 2010) kHz and this is because the signal is higher after the 3600 s polarization time and, since we scale all the curves to one by dividing by the first value of magnetization, we get it manually from the saving data (so we divide by a large initial value and hence all of the curve will appear in the lower part of the figure), while in the 600 s polarization

time you get a small initial value of magnetization and by dividing the rest of the values by this small value we will get large numbers appearing in the upper part of the figure.

$$\frac{1}{T_z} = \frac{C_T}{C_T + C_z} [M_z] \quad (1)$$

And by using equation 1 and the 0.9 and 0.18 values in Fig.4.17, we conclude that the

ratio $\frac{C_T}{C_T + C_z}$ is equal to $1/(0.9/0.18) = 1/5$ and this gives us the ratio $\frac{C_z}{C_T}$ equal to 4.

While the usual value of the ratio is 3 in the materials that contain only methyl group protons, here we have this high ratio because in this material there are more protons than in the methyl group and this result assures the fact that in our sample we have more different protons. Also we notice that all the heat capacity curves do not go to zero because during the switching process of the field steps there is some relaxation happening. Finally we notice that for the frequencies (1810, 1910, 2010) kHz the approximate values of (a) for both polarization times 600 and 3600 s are growing to a maximum value at (1910) kHz and then decreasing to ((2.36, 4.33, 4.01) and (4.37, 4.7, 3.22)) respectively, while (c) approximate values for both polarization times 600 and 3600 s have an opposite behaviour of decreasing to a minimum at (1910) kHz and then growing again to ((0.465, 0.211, 0.452) and (0.248, 0.0999, 0.33)) respectively.

Additionally the decay factor for the heat capacity (b) approximate values for a polarization time of 600 s take a decreasing curve by the values (0.673, 0.588, 0.502), and for the polarization time (3600) s by an increasing curve through the values (0.569, 0.605, 0.637).

4.7 The spin-lattice relaxation time T_1 measurements:-

The aim of these measurements of magnetization-recovery, i.e. T_1 measurements, is to use them to calibrate the observed NMR signal amplitude in terms of absolute units of inverse Zeeman temperature and spin polarization to calibrate the spectrometer and

hence making them more connected to the experimental part of this research and we included it here since there will be a similar separated process for Methyl Ethyl Ketone (MEK) will be mentioned with its measurements.

1. We start by measuring T_1 at the temperature 40 K and for two measurements fields 0.4 and 1 T, as shown in Fig.4.18.

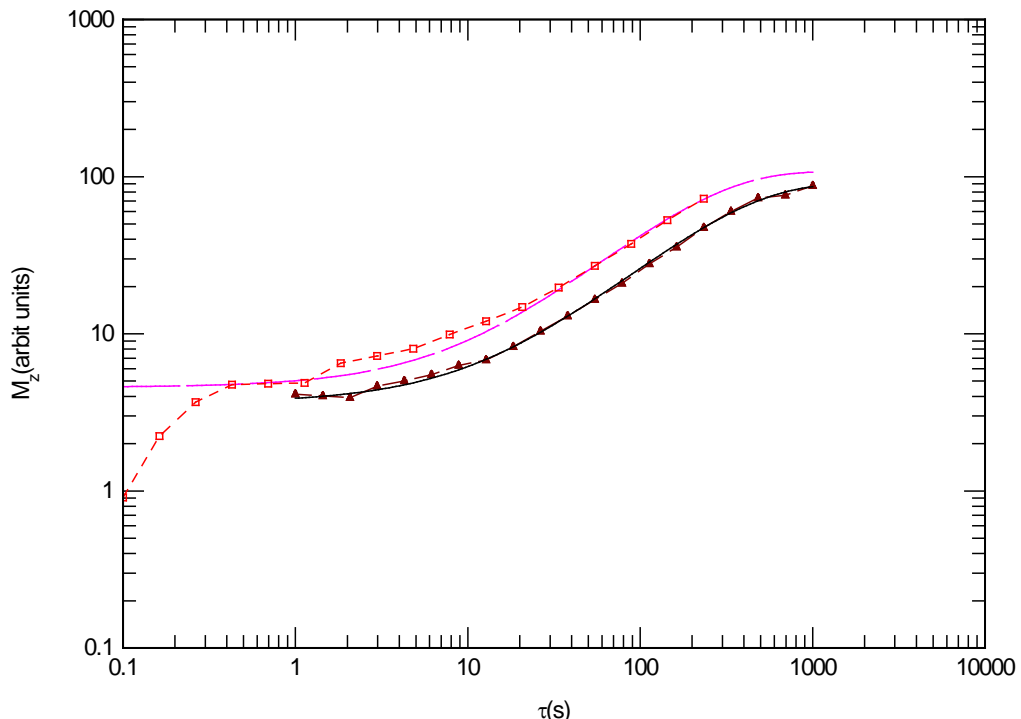


Figure 4.18: The spin-lattice relaxation time T_1 measurement, 40 Kelvin, 4kG (\blacktriangle) and 1T (\square), and we fit both curves to the equation $y=a*\exp(-x/b) + c$ shown as solid lines. And we obtain the following T_1 approximate values 336 and 223 respectively.

2. Secondly we measure T_1 at the temperature 55 K and for the same two measurements fields 0.4 and 1 T, adding to them the 0.2 T measurement.

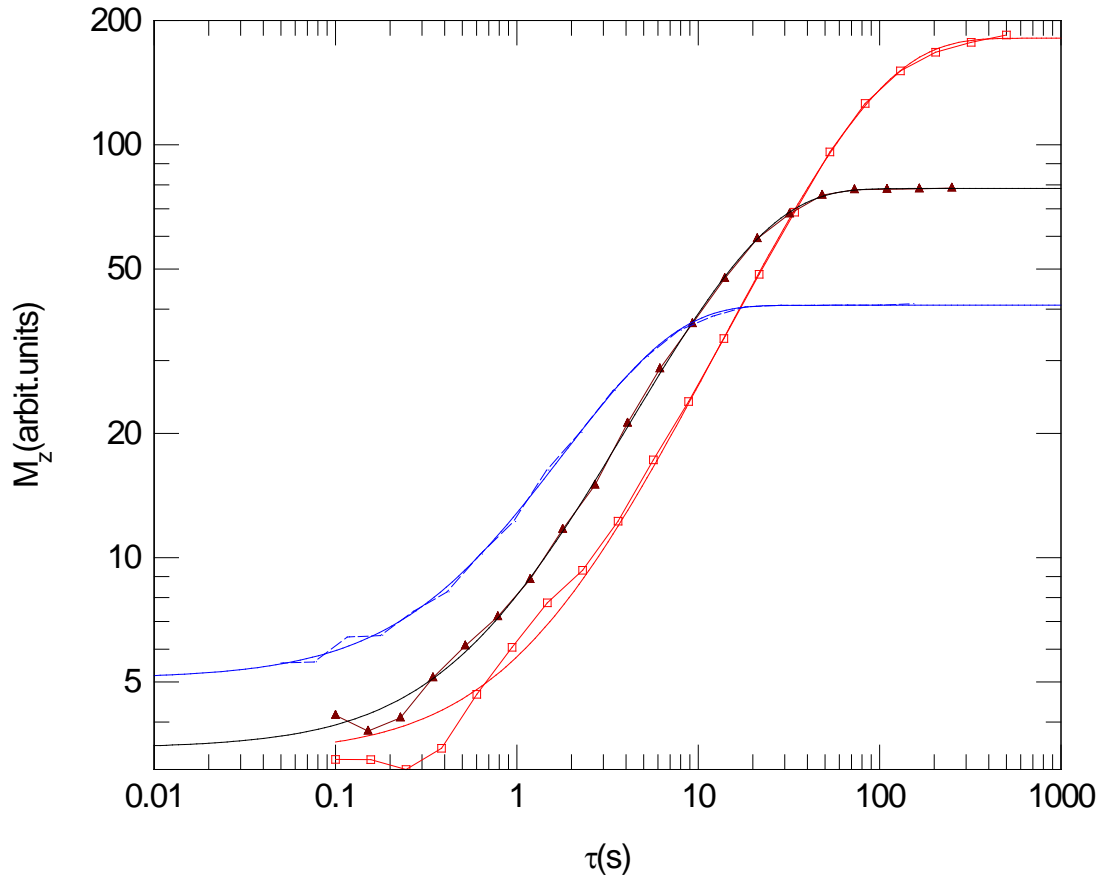


Figure 4.19: The spin-lattice relaxation time T_1 measurement, 55K, 2kG (○), 4kG (▲) and 1T (□), and we fit all curves to the equation $y=a*\exp(-x/b) + c$ shown as solid lines.

And we obtain the approximate values (15.57, 72.98, 4.096) respectively, where we notice how the T_1 values for 0.4 and 1 T have decreased as we increase the temperature, as shown in Fig.4.21.

3. Finally we make a different procedure to measure T_1 at the temperature 4.2 K for the measurement field 1 T since it will take a long time to measure T_1 at the low temperature, as we conclude from the previous two items. We take a series of measurements for T_1 values using a zero dB (no attenuator) case at the start of the spectrum, since it will take a long time to measure all the spectrum, and a 20 dB (attenuator) case for all the spectrum in no continuous steps to get an idea of the values of M_z we will obtain as shown in Fig.4.20.

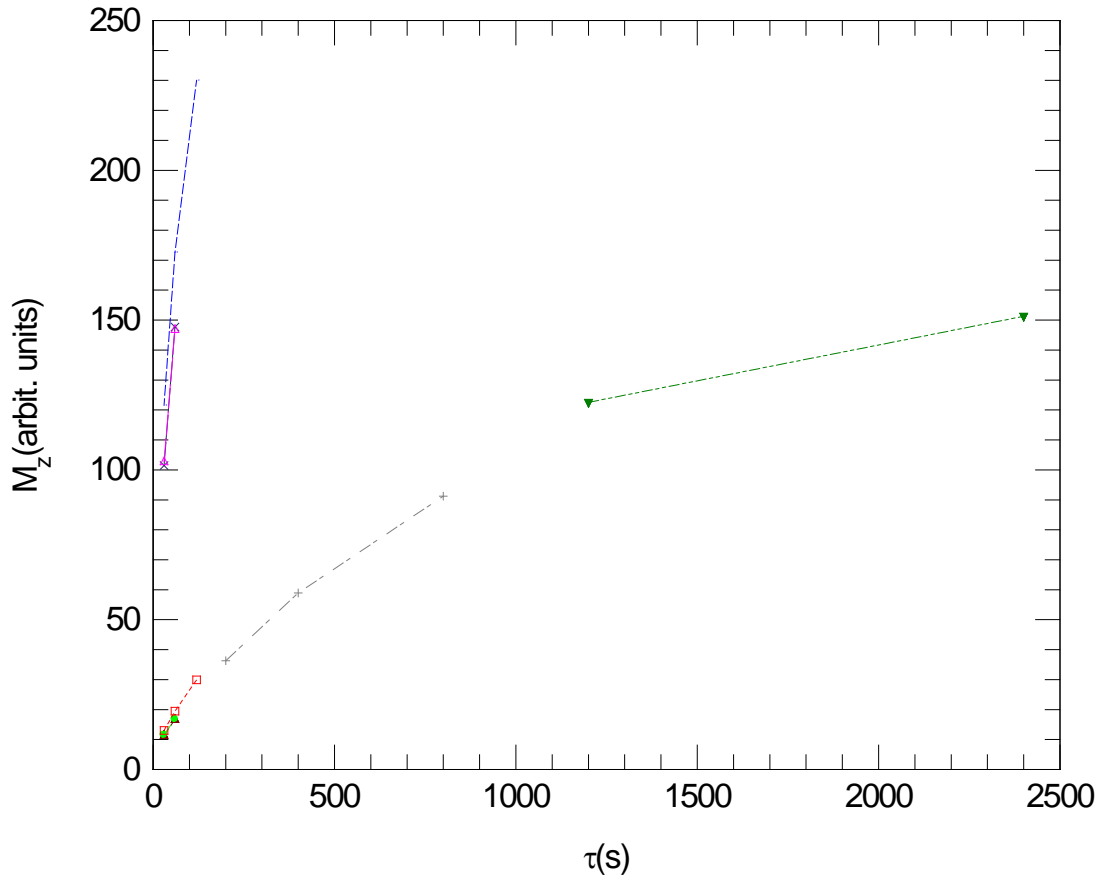


Figure 4.20: The spin-lattice relaxation time T_1 measurement, 4.2 Kelvin, 1T, 0 (\times , Δ , \circ)

and 20 (\blacktriangle , \bullet , \square , $+$, \blacktriangledown) dB.

And we notice that there is a good agreement for the same repeated measurements of 0 and 20 dB. In addition for 20 dB we notice that even if we take no continuous steps measurements, there will be a conventional T_1 curve behaviour as if we imagine them connected, as shown in Fig.4.20.

And if we make an interpolation for the 20 dB curves using a MATLAB program we get an identical continuous curve which by fitting to it we get an approximate value of T_1 equal to 1031. Then we take the 0 dB curve and also make an interpolation for it using the MATLAB program using its values to divide the corresponding values of 20 dB so we can get the ratio of increasing and taking an average for these ratios we find that it equals to approximately 7.8. Multiplying it by the interpolation values we get for 20 dB, which we could not measure for 0 dB, we get a good estimation of the T_1 curve

for the case of 0 dB and this appears after we fit it, getting a similar approximate T_1 value to that we get for the previous 20 dB interpolation fitting which is 1028 s, as shown in Fig.4.21.

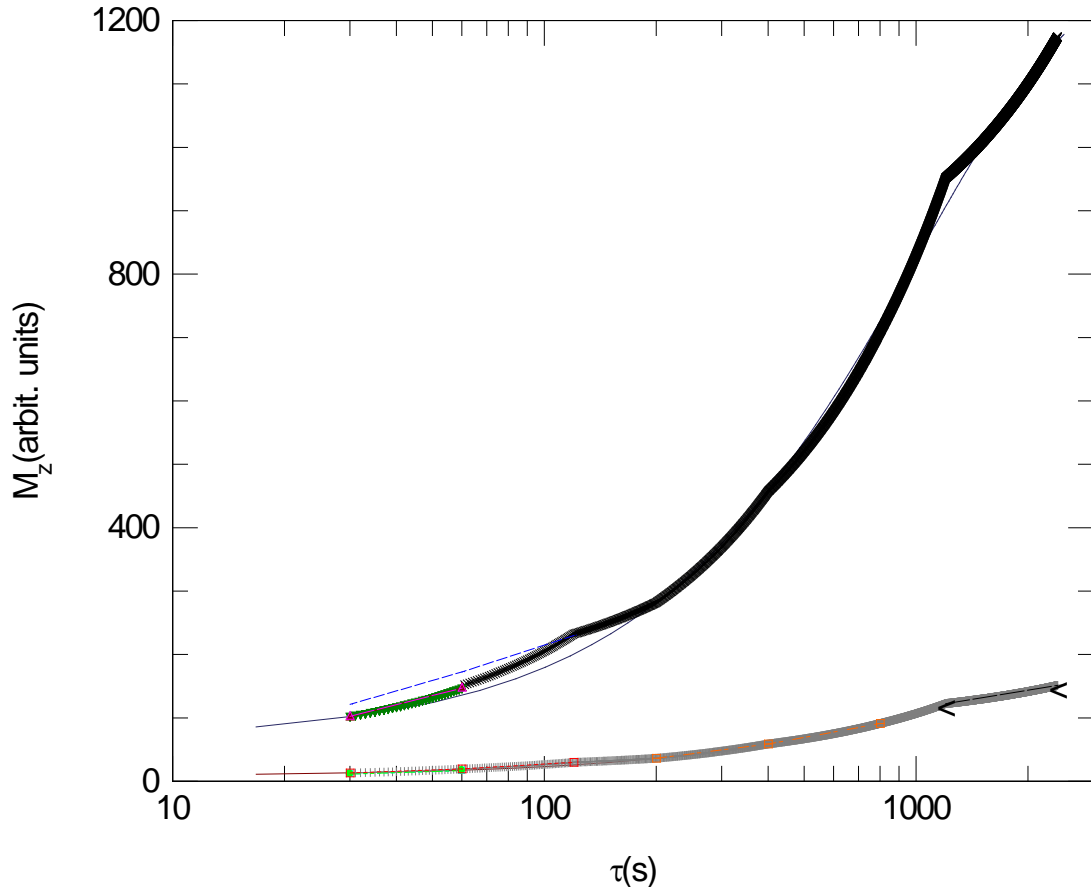


Figure 4.21: The spin-lattice relaxation time T_1 measurement, 4.2 Kelvin, 1T, 0 (\circ , Δ , \blacktriangle) and 20 (\square , $<$, \square , \bullet , \blacksquare) dB and the interpolations for 0 (\blacktriangledown) and 20 (+) dB with the 0 dB resulting from multiplication of ($k=7.765115$) by the 20 dB values (\times), and we fit both curves to the equation $y=a*\exp(-x/b) + c$ shown as solid lines.

And in both cases we notice that the T_1 value is very long since we measure it in a very low temperature 4.2 K.

Chapter 5 Dynamic Tunnelling Polarization: (methyl ethyl ketone)

We are familiar with pulsed NMR techniques for manipulating the polarization and magnetization of a system of spins. A resonant rf pulse applies a torque which rotates the magnetization vector and hence changes the polarization state. Various manipulations may be made by applying multiple pulses and at the end of a sequence; the longitudinal polarization can be measured by applying a 90°-pulse. In investigating methyl group containing materials, the NMR properties are often influenced by the polarization state of the tunnelling levels. This is because the nuclear Zeeman and tunnelling systems are mutually coupled. To gain a deeper understanding a question arises whether it is possible to manipulate the tunnelling polarization in a prescribed manner, analogous to the manipulation of Zeeman polarization states. This is the motivation for this and the preceding chapter. A novel field-cycling pulse sequence will be described that enables the tunnelling polarization state to be manipulated and determined.

The novel experiments to be described depend on a couple of important ideas; 1) to drive ‘forbidden’ transitions that involve a change in tunnelling state, with rf irradiation at low magnetic field, 2) to utilize level crossings within the manifold of tunnelling-nuclear magnetic energy states, which appear at particular values of *B*-field : the ¹H Zeeman polarization can act as a proficient sensor of the tunnelling polarization by bringing the tunnelling system into contact with the previously saturated Zeeman system at a level-crossing.

The sample selected for these experiments is methyl ethyl ketone: CH₃CH₂ (CO) CH₃. This has a methyl tunnel frequency of 490 kHz as determined by low-field NMR. It was considered a good choice of sample because there are known tunnelling sideband transitions involving *A-E* tunnelling transitions in the NMR spectrum. Since MEK is a

liquid at room temperature. The sample was first sealed in a 5mm NMR tube using a Teflon plug. Then it was frozen inside in the NMR probe by slowly immersing in liquid nitrogen. The cold probe was then inserted in the helium sample space before cooling to 4.2K where all experiments were conducted.

5.1 The conventional low field scan and Dynamic Tunnelling Polarization scan:-

5.1.1 Conventional low field scan:-

A conventional low-field scan (see Fig. 4.2) of MEK is shown in Figure 5.1. The 1H polarization time was 60 s at 1 T and the low-field irradiation time was 5 s at 180 Gauss. In the spectrum the NMR lines *A* and *B* are labelled along with three tunnelling sidebands corresponding to the *b*-, *b*+, *a*+ and the $\Delta m = 0$ line *C*. Frequencies below 400 kHz there are three artefacts which should be disregarded; these arise from harmonic distortion of the secondary rf field. These appear at integer fractions of the Larmor frequency in the low field 180 Gauss, namely $\omega_{rf}/2$, $\omega_{rf}/3$ and $\omega_{rf}/5$. Hence they are harmonics of the main NMR line *A*. The lowest frequency harmonic may be obscuring the sideband *a*- in the conventional low field spectrum.

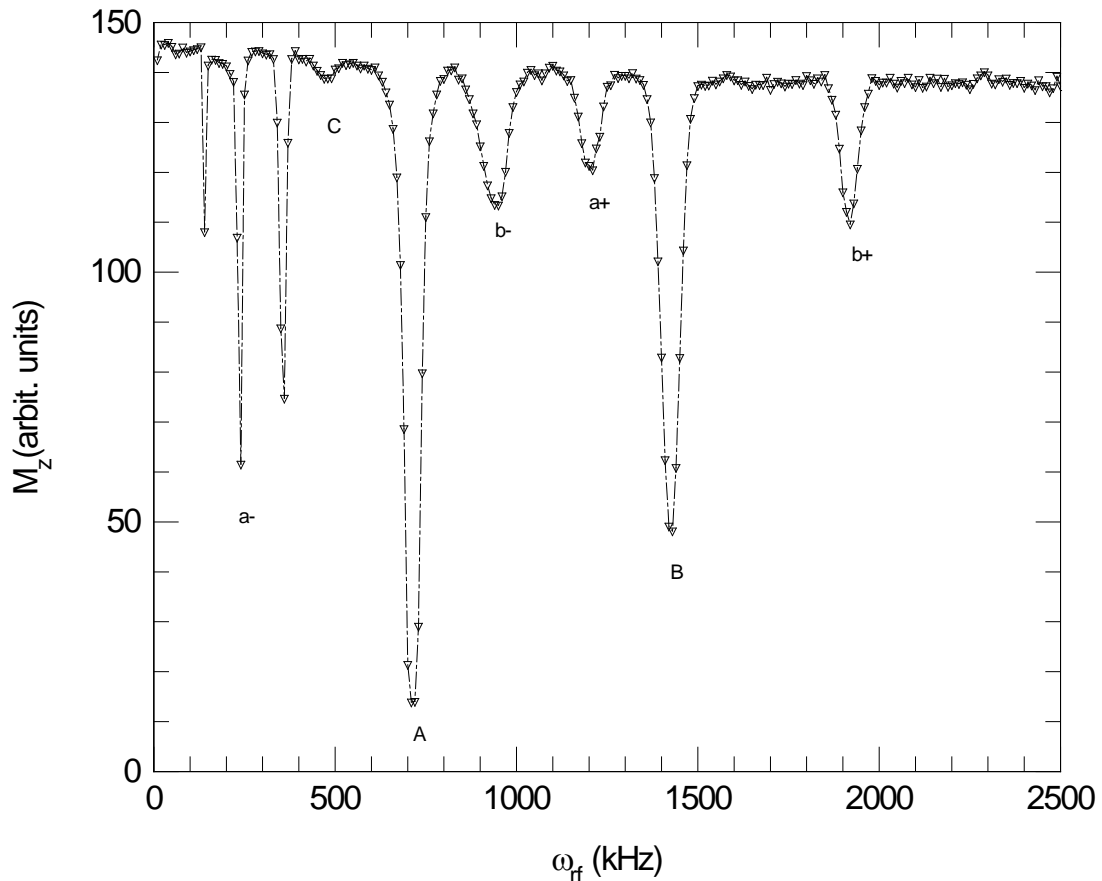


Figure 5.1: The full conventional low field scan with a guessing of the sideband a - position which obscured by the lowest frequency harmonic.

Analyzing the tunnelling sideband transition frequencies, one of the important results extracted from the low-field NMR spectrum is that the tunnelling frequency is 485 kHz.

5.1.2 The DTP pulse sequence:-

The DTP pulse sequence has been described previously (4.1.2.a). To recapitulate, the 1H Zeeman reservoir is first polarised at high field. The magnetic field is then switched down to a low value and the transitions within the tunnelling-Zeeman manifold are driven by rf irradiation. Some transitions involve changes in tunnelling state. To measure the consequent changes in population of the A and E states the Zeeman polarization is first reduced to zero by a burst of rf pulses at the resonant field, then contact between the tunnelling and Zeeman reservoirs is made at a level crossing as shown in Fig.4.3.

5.1.3 Dynamic Tunnelling Polarization (DTP) scans:-

1. A DTP spectrum of MEK is shown in Fig. 5.2, recorded in the frequency range 10 to 2500 kHz. The sample was first polarized at a field of 1 T for 300 s. The rf irradiation was conducted at 180 G for 2 s. Following saturation of the Zeeman system, the transfer of tunnelling polarization to Zeeman polarization was carried out at the level crossing at 130 G for 2 s. The Zeeman (i.e. tunnelling) polarization was determined with a 90° measurement pulse at the resonance field 8525 G.

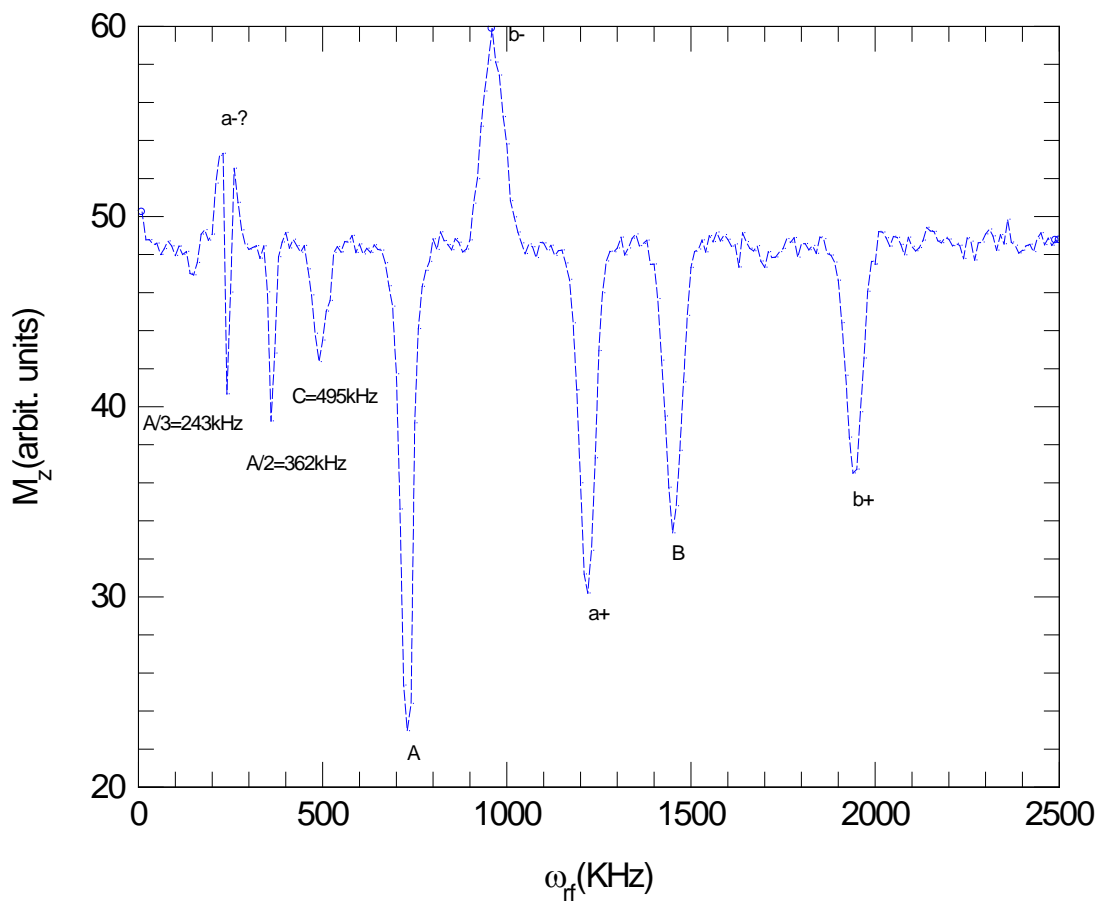


Figure 5.2: The DTP spectrum of MEK recorded at the field 180 Gauss.

There are a number of interesting features in the spectrum. Significantly the negative sidebands a^- and b^- appear as positive peaks while the positive sidebands a^+ and b^+ appear as negative peaks. This is analogous to ‘dynamic nuclear polarization’ and the solid effect [17] in NMR, the difference is that the DTP spectrum maps out the

tunnelling polarization resulting from the secondary rf irradiation. For this reason the phenomenon is described as ‘dynamic tunnelling polarization’ (DTP). For the negative sidebands where positive peaks are observed, the tunnelling states are cooled by rf-irradiation. This observation can be explained by the energy level diagram where it is clear that negative sidebands arise from *E-A* transitions in tunnelling state, leading to a cooling of the tunnelling reservoir. Conversely, positive sidebands arise from *A-E* transitions, leading to a heating of the tunnelling reservoir and hence negative peaks against the baseline. There are a number of problems with the spectrum in Fig. 5.2. We observe the appearance of harmonics of the main $|\Delta m|=1$ NMR line A at the start of the spectrum as seen previously in the conventional low field scan (Sec.5.1.1); this leads to the same problem of determining the *a-* which is partially obscured by them. As we shall see, the solution is to increase the irradiation field so that the *a-* sideband moves to a different region of the spectrum from the harmonic artefacts. A second issue is the significant amplitudes of the NMR lines *A* and *B*; despite the saturation of the Zeeman system, these are appearing with significant intensity. The explanation is that at the irradiation field set, the system lies within the level crossing region, meaning this is a region of the spectrum where there is significant Zeeman-tunnelling coupling and so the rf irradiation is driving changes in both Zeeman and tunnelling polarizations. By recording the spectrum at a higher magnetic field, as in the next section, we expect to alleviate these problems.

2. The DTP spectrum was recorded with an irradiation field of 290 G, Fig. 5.3. The Zeeman system was polarized at 1 T for 270 s, and the rf irradiation was conducted at 290 G for 5 s. Following Zeeman saturation, the transfer of polarization from the tunnelling system to the Zeeman system was conducted at the level crossing field of 125 G for 2 s. The sequence ended with a 90° measurement pulse at the resonance field of 8525 G. The resulting spectrum in Fig 5.3 shows the dynamic polarization of the tunnelling reservoir more cleanly, alleviating the problems described for Fig. 5.2. Since the irradiation field of 290 G is further from the level crossing field of 125 G we significantly reduce the amplitude of the peaks centred on the *A* and *B* NMR lines, meaning that there will be no pure Zeeman transitions during the irradiation step. This has the added advantage of diminishing the harmonic artefacts at low frequency and we are able to clearly recognize *a*- in the spectrum.

The dynamic polarization of the tunnelling system is more clearly observed. The negative sidebands show significant cooling of the tunnelling reservoir. The positive sidebands show significant heating; in fact the polarization is clearly inverted for the *a*+ sideband indicating there is inversion of the populations of the tunnelling levels and the *E*-species acquire a larger population than the *A*-species.

Another interesting feature is the appearance of a new peak existing between *A* and the *a*+ which is a double tunnelling sideband at the frequency $2\omega_L - 2\omega_t$. Evidently there is mechanical coupling between the two identical methyl groups so that rf irradiation drives *EE-AA* double tunnelling transitions. These features of the DTP spectrum will be

investigated in more detail in the next experiments.

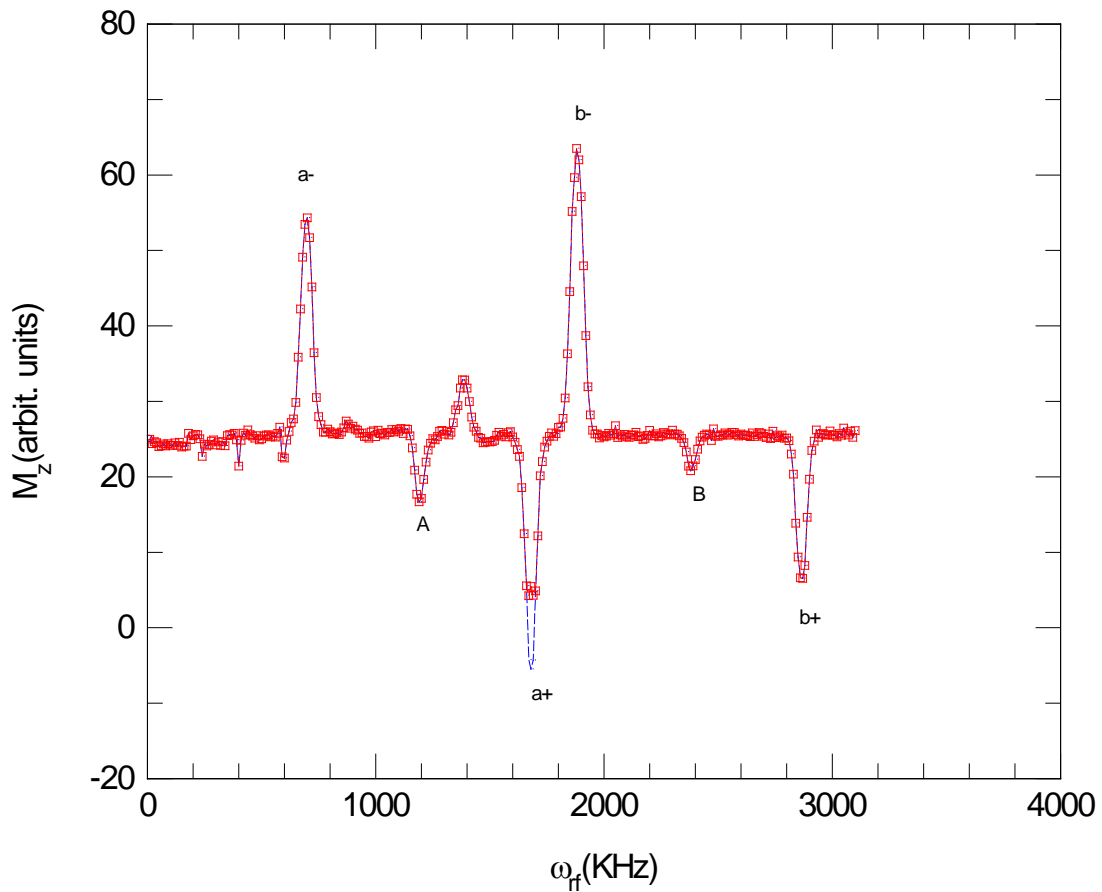


Figure 5.3: The DTP spectrum of MEK recorded with the irradiation field 290 G and Zeeman polarization time of 270 s. A phase correction (\circlearrowleft) appears in the negative region has been made to the $a+$ sideband (\square) which exhibits the population inversion of the tunnelling reservoir. $T = 4.2$ K

A final minor difference between the spectra of Fig. 5.2 and 5.3 is the ordering of the tunnelling sidebands. Notice how the irradiation field B_{low} is chosen in Fig. 5.3 so that ω_L is greater than $2\omega_t$; if the irradiation field had been a little higher then both peaks, the $b-$ and $a+$ would overlap $\omega_L = 2\omega_t$.

The DTP phenomenon involves a transfer of polarization from the Zeeman reservoir to the tunnelling reservoir and this can be clearly seen in Fig. 5.4 where the spectra recorded with Zeeman polarization time 2000 s is compared with that recorded with

polarization time 270 s. The dynamic polarization of the tunnelling reservoir is enhanced when the initial Zeeman polarization is larger, as shown by the growth of the DTP sideband intensities; this will be studied in more detail in a later section.

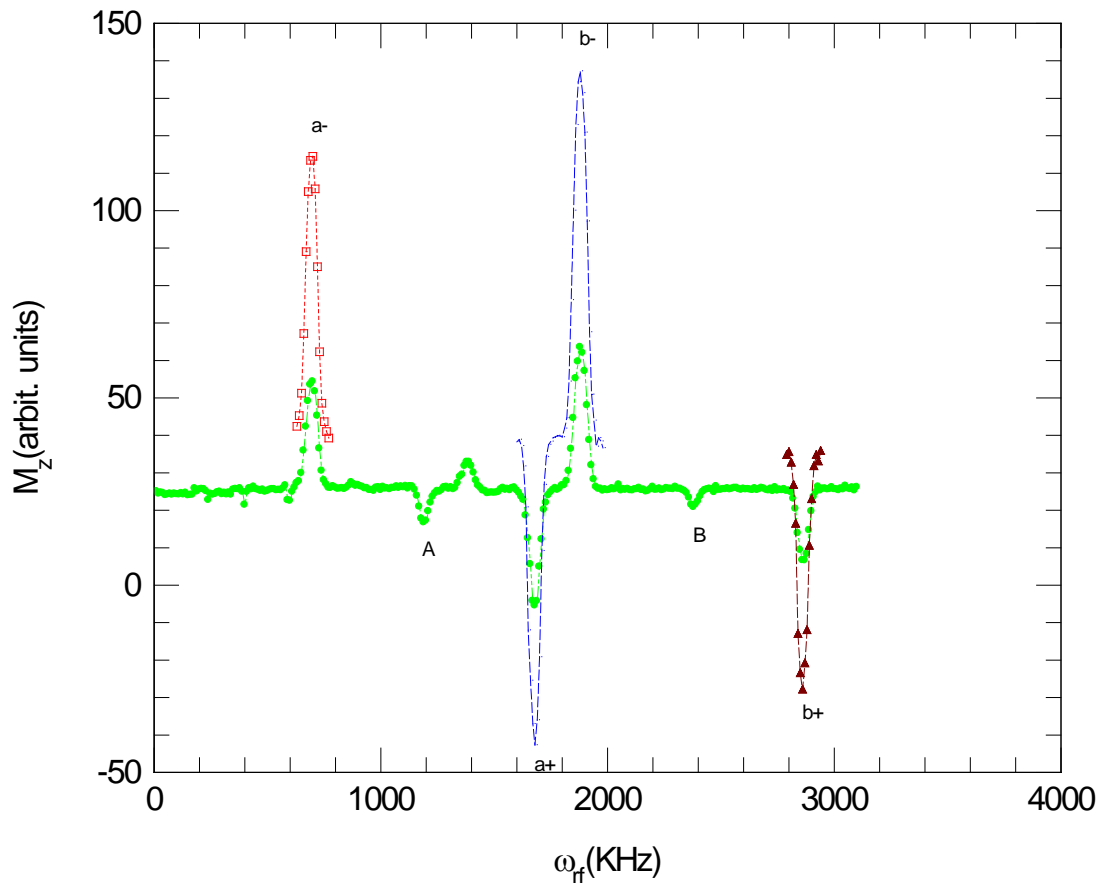


Figure 5.4: The DTP spectrum of MEK recorded at 290 G with Zeeman polarization times of 270 s (●) and 2000 s (□, ○, ▲) at 1 T. The dynamic polarization of the tunnelling reservoir is significantly enhanced for the longer Zeeman polarization time.

3. We shall now investigate the appearance of the double tunnelling sideband peak to understand better where it comes from.

A DTP scan was made with the irradiation field 330 G; Zeeman polarization at 1 T for 270 s, rf irradiation at 330 G for 5 s, level crossing contact at 125 G for 2 s. The spectrum is shown in Fig.5.5., and we notice that we have minimized the double tunnelling sideband peak. In recording the spectrum at a field which is further far from

the level crossing region the probability of a double tunnelling sideband transition has been significantly reduced.

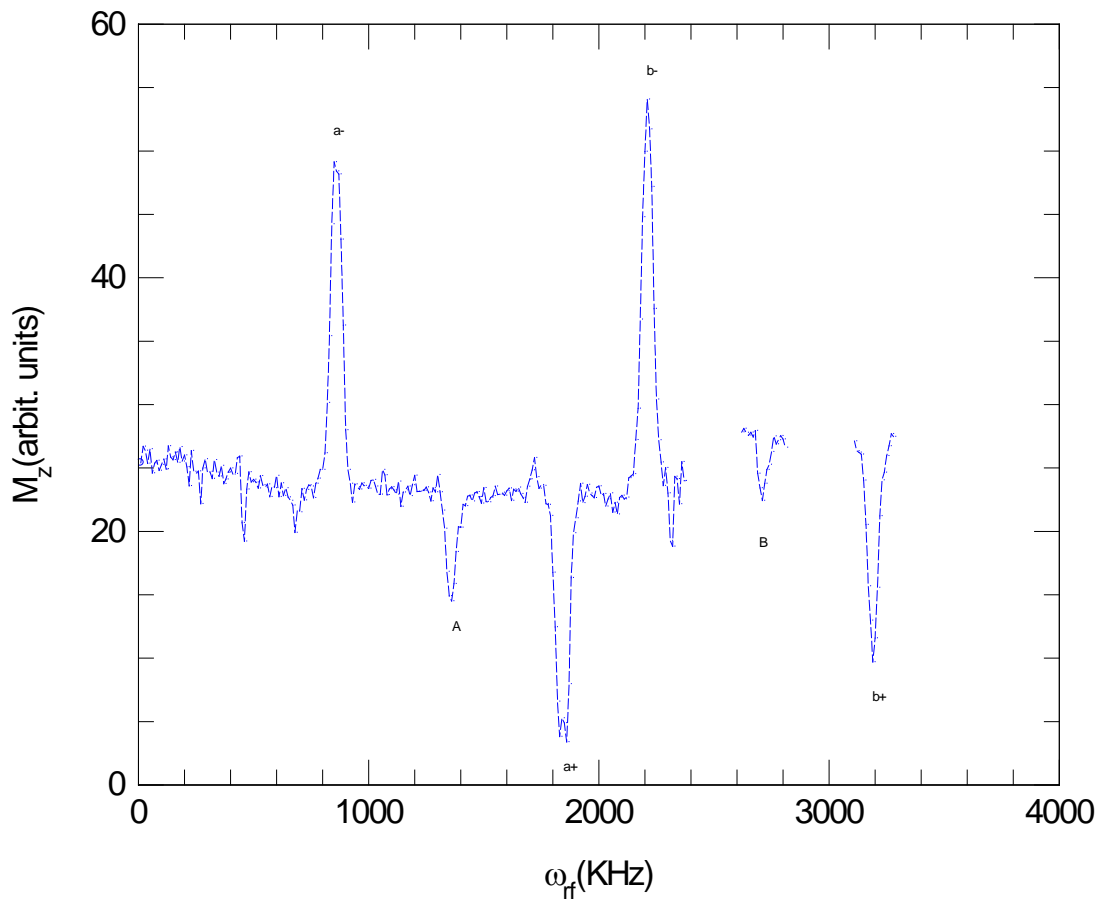


Figure 5.5: The new irradiation field DTP scan for 330 G with small effect of the new peak.

Conversely, the lower the irradiation field, the closer the system is to a double level crossing (*AA-E_E*) and the higher the probability of the double tunnelling sideband transition.

By making a comparison between the 290 and 330 G scans. Fig. 5.6, we notice that the spectrum has been shifted to the right according to the relation ($\omega = \gamma^* B$) and the disappearance of the double tunnelling sideband peak is clear.

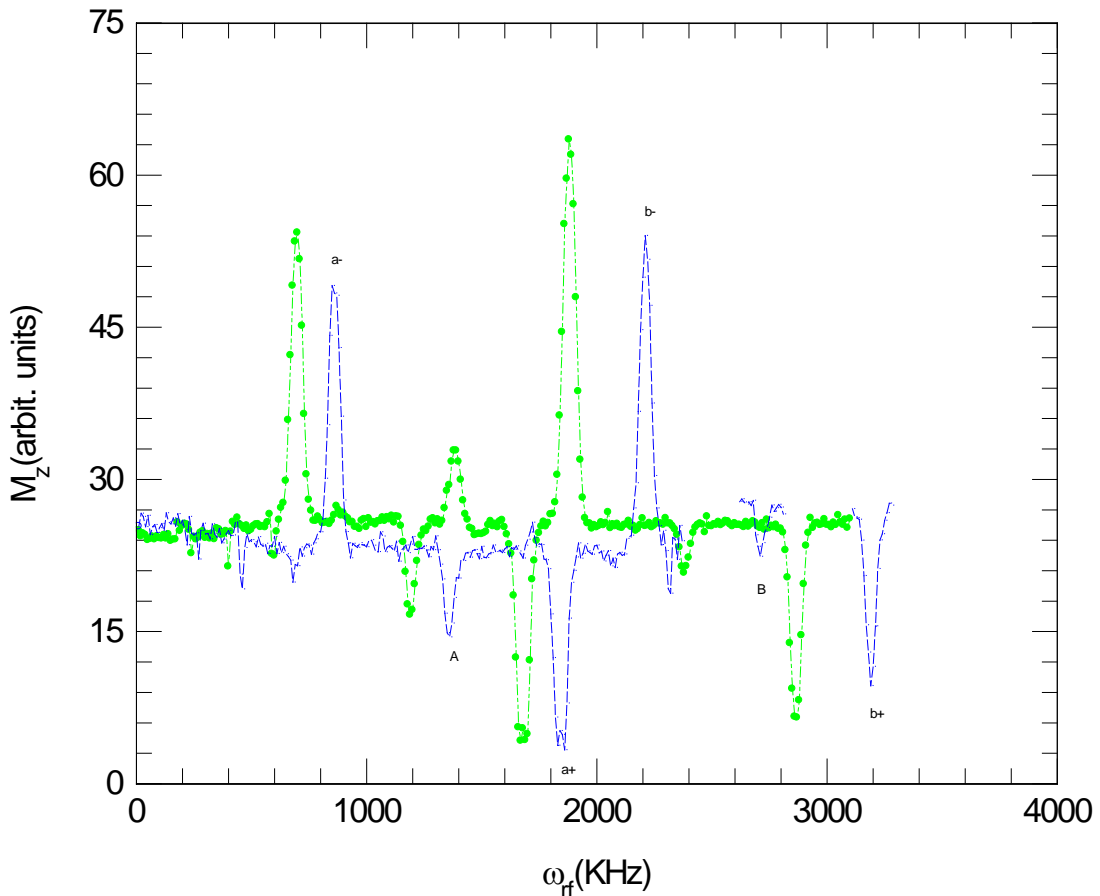


Figure 5.6: Comparison of the DTP spectrum for irradiation fields of 290 (●) with big effect of the new peak and 330 (○) G which shows small effect.

5.2 The effect of changing the Zeeman polarization time on the spectrum:-

5.2.1 The effect of changing the polarization time in the 180 G low field case:-

1. Firstly we study the b- peak with different polarization times (100, 300, 600, 900, 1200, 2000, and 4000) s at 1 T. The rf irradiation is conducted at 180 G for 5 s and the level crossing contact was made at 130 G for 2 s. Secondly we study the b+ peak under the same conditions with polarization times (100, 300, 600, 900, 1200, 2000, 4000) s. The amplitude of the DTP sideband peaks were determined by taking the difference between the peak amplitude and the average of the baseline on either side of the DTP peak. The data is shown in Fig.5.7. We notice that b- increases in the positive direction while b+ increases in the negative direction; this is because we drive tunnelling

transitions in opposite directions, with the $b-$ transition from the E -species to the A -species, while the $b+$ transition is from the A -species to the E -species, as shown in the energy level diagram of Fig.2.15.

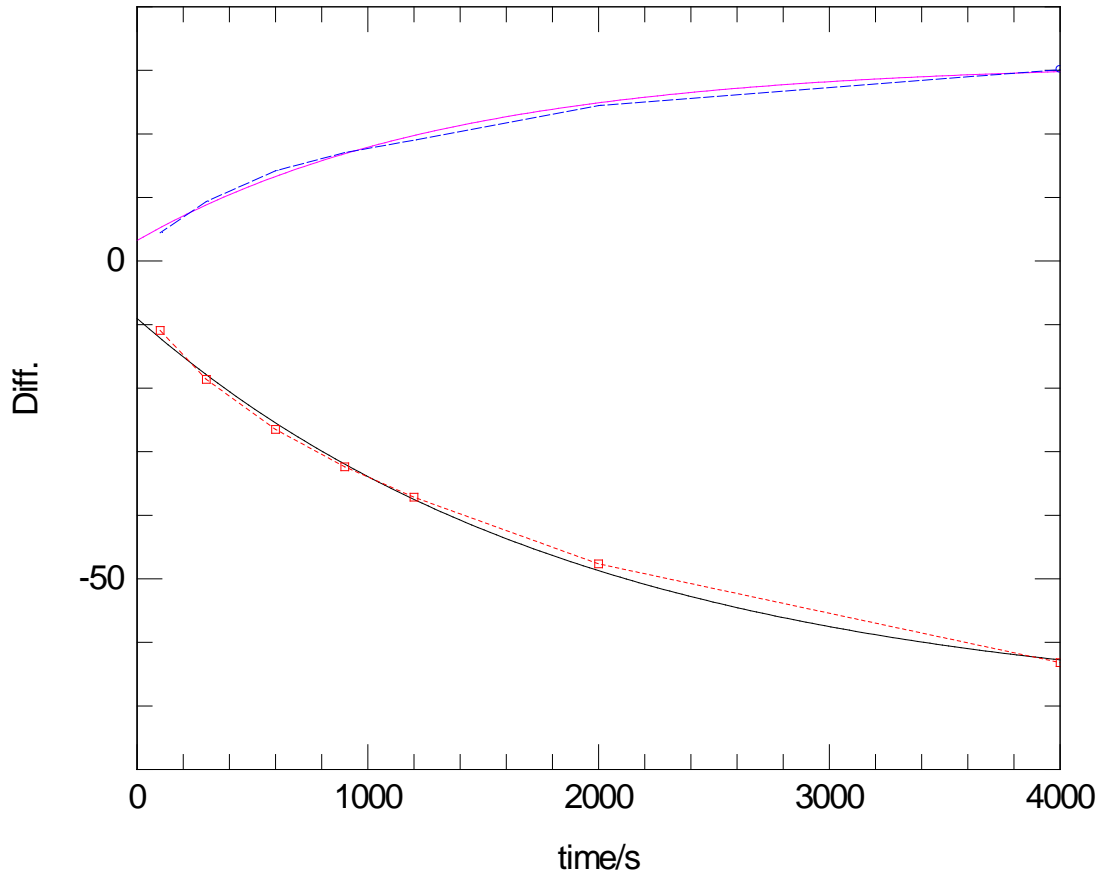


Figure 5.7: The DTP peak amplitude as a function of the Zeeman polarization time for the $b-$ (○) and $b+$ (□) sideband peaks and 180 G irradiation field.

The curves have been fitted with the exponential function shown as solid lines, where C is a constant.

$$y = a \left(1 - \exp \left(-\frac{t_{pol}}{k} \right) \right) + c$$

The time constants ' k ' for the two curves are of order 1500 s which is of similar magnitude to the value of the 1H spin-lattice relaxation time at the polarization field. This indicates that the DTP phenomenon involves a transfer of polarization from the

Zeeman reservoir to the tunnelling reservoir in an analogous way to DNP and the solid effect in NMR.

Also we notice that the baseline of both the *b*- and *b*+ changes and is not fixed in one place, maybe because the system memory is of dipolar order rather than Zeeman order.

2. We study the *a*+ peak at different polarization times (100, 300, 600, 900, 1200, 2000, 4000) s at 1 T and after that we irradiate the system at 180 G for 2 s taking 2 s to saturate the sample followed by a 2 s transfer to the level crossing at 130 G ending with a measurement pulse at the resonance field of 8525 G. By taking the difference between the peak and the average of the baseline of the previous *a*+ peak, see Fig.5.8 included in Fig.5.7, as in item 2 we notice that in the *a*+ there is an increase of the magnetization in the negative direction compared with the *b*- in the positive direction, where for the same reason as for the *a*+ we drive transitions from level *A* to level *E* so the tunnelling reservoir gets warmer, and so it gets more negative.

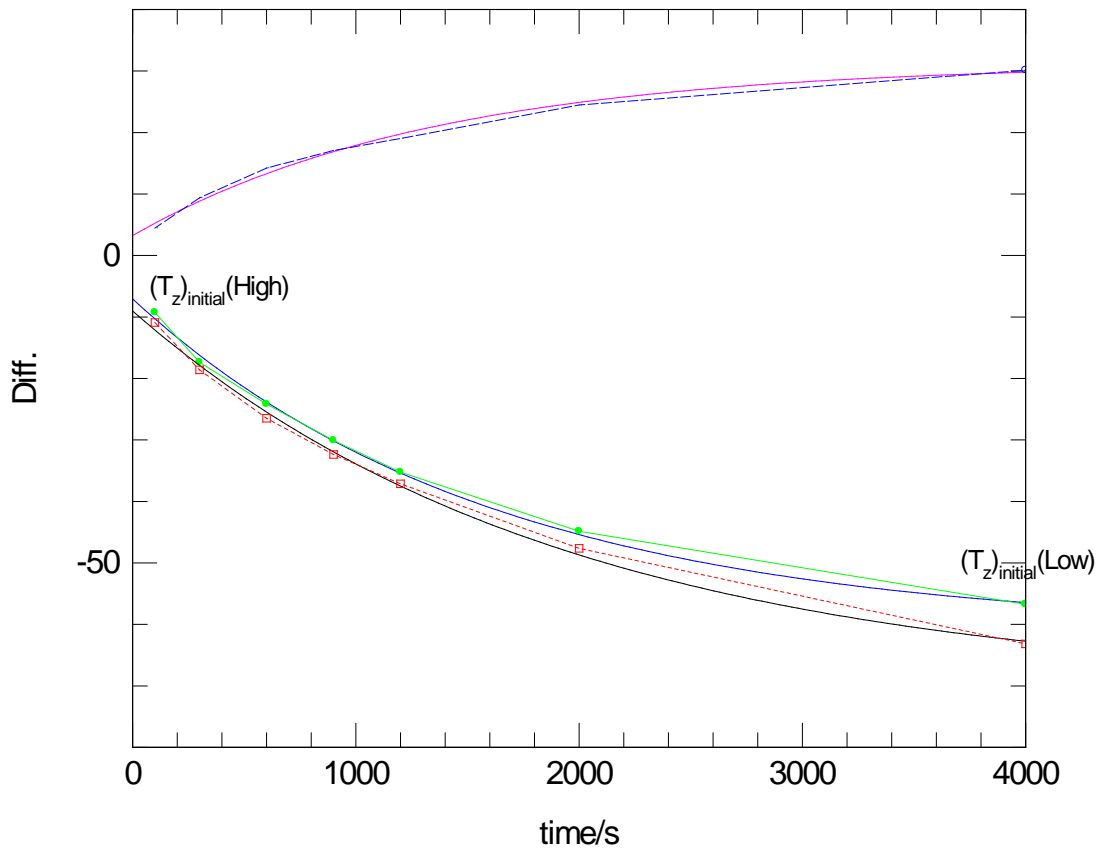


Figure 5.8: The difference between the peak and the average of the baseline for the curves which represent the changing of the polarization time for the $a+$ peaks (\bullet) at the 180 G irradiation field for (2) s, versus polarization time comparing it with the results of

Fig. 5.7.

Also this curve give us the high and low initial Zeeman temperatures, and if we put it with a measurement of T_1 at 1 T and at 4 K temperature using 30 dB as an attenuator, by making the difference values positive we notice that it shows the same spin lattice relaxation curve behaviour, as shown in Fig.5.9.

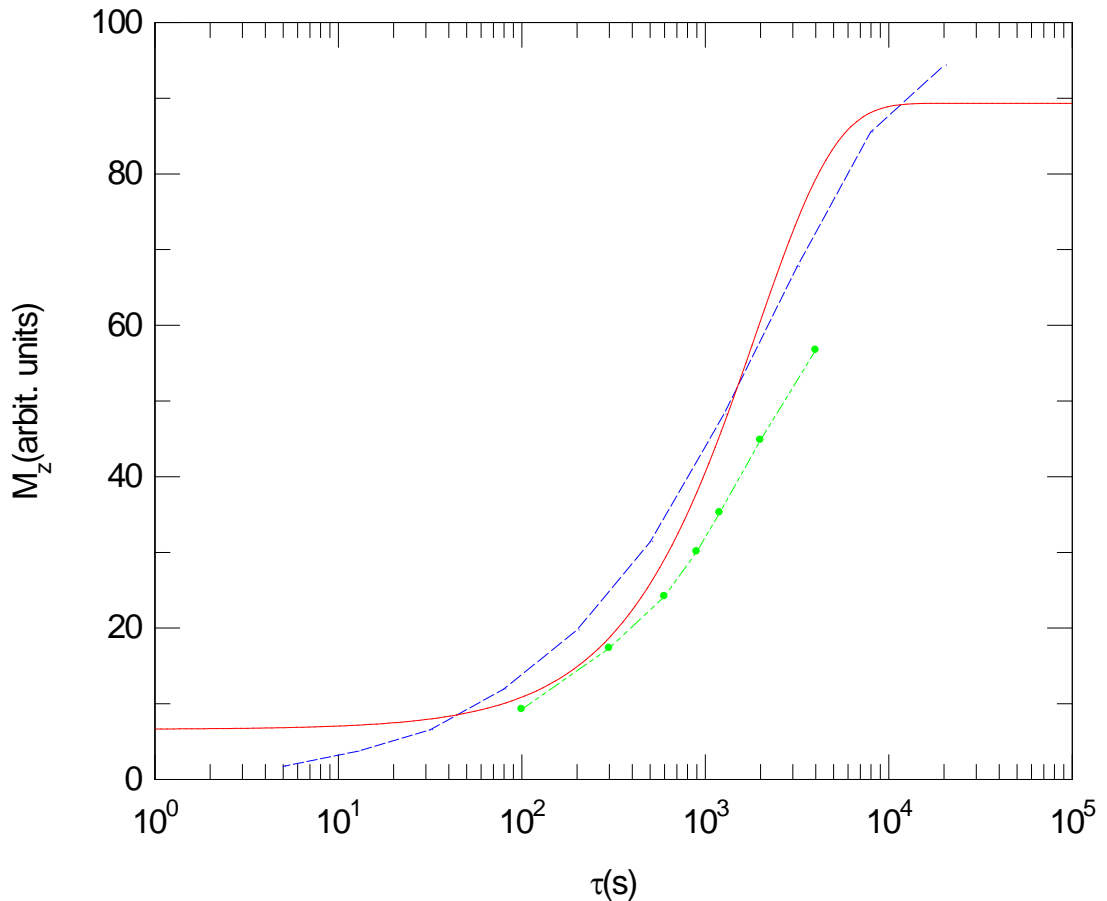


Figure 5.9: The positive values of the difference between the peak and the average of the baseline for the curves which represent the changing of the polarization time for the $a+$ peak at the 180 G irradiation field (\bullet), versus polarization time with the spin lattice relaxation curve (\circ).

3. The *C* and *A* peaks were studied as a function of polarization times (100, 300, 600, 900, 1200, 2000, 4000) s at 1 T. The rf irradiation was 2 s at 180 G. The saturation step was followed by a field switch to the level crossing at 130 G and the cycle was completed with a measurement pulse at the resonance field of 8525 G. By taking the difference between the peak and the average of the baseline of the *C* and *A* peaks, we determine the data in Fig. 5.10.

As in item 2 we notice that in the *a+* there is an increase of the magnetization in the negative direction compared with the *b-* in the positive direction, where for the same reason for *C* we drive transitions from level *A* to level *E* so the tunnelling reservoir gets warmer, and so it gets more negative, and as we see from the curves, both the peak and the baseline become bigger as we increase the time so the difference between them will increase in the negative direction.

Also we notice from Fig. 5.10 that there are different baselines appears in the initial data. This is because the rf irradiation field 180 G is sufficiently close to the level crossing field 130 G, that there is an energy transfer between the Zeeman and tunnelling reservoirs, so during irradiation we change not only the tunnelling but also the Zeeman temperature, giving rise to the observed difference in baseline.

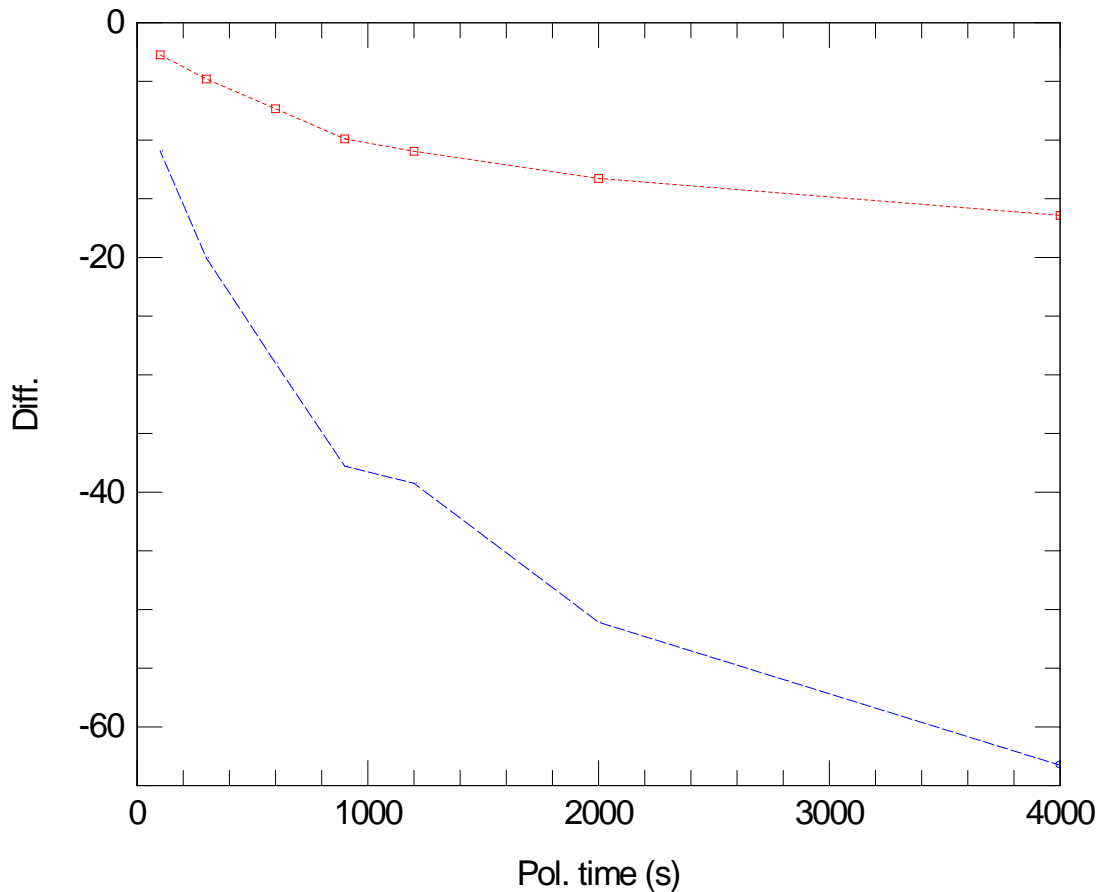


Figure 5.10: The difference between the peak and the average of the baseline for the curves which represent the amplitude of the C (□) and A (○) peaks vs. polarization time.

rf irradiation 2 s at the 180 G.

As in item 2 we notice that in A there is an increase of the magnetization in the negative direction compared with the *b*- in the positive direction, where for the same reason for A we drive transitions from level *A* to level *E*, and so it gets more negative because the readings are contaminated and, as we see from the curves, both the peak and the baseline become bigger as we increase the time so the difference between them will increase in the negative direction.

5.2.2 The effect of changing the polarization time in the 290 G low field case:-

We study the *b*- peak at different polarization times (100, 300, 600, 900, 1200, 2000, 4000) s at 1 T after that we irradiate the system at 290 G for 5 s taking 2 s to saturate the

sample followed by a 2 s transfer to the level crossing at 125 G, ending with a measurement pulse at the resonance field of 8525 G. By taking the difference between the peak and the average of the baseline of the previous *b*- peak, we have Fig.5.11, with a comparison to the previous 180 G curve. Compared with the 180 G curve as shown in Fig. 5.7, we notice an increase of the difference values as we increase the irradiation field from 180 G to 290 G because, as mentioned previously, the 180 G curve is contaminated so it has a small tunnelling reservoir component which should be created in the irradiation process and then converted to a Zeeman reservoir in the level crossing step.

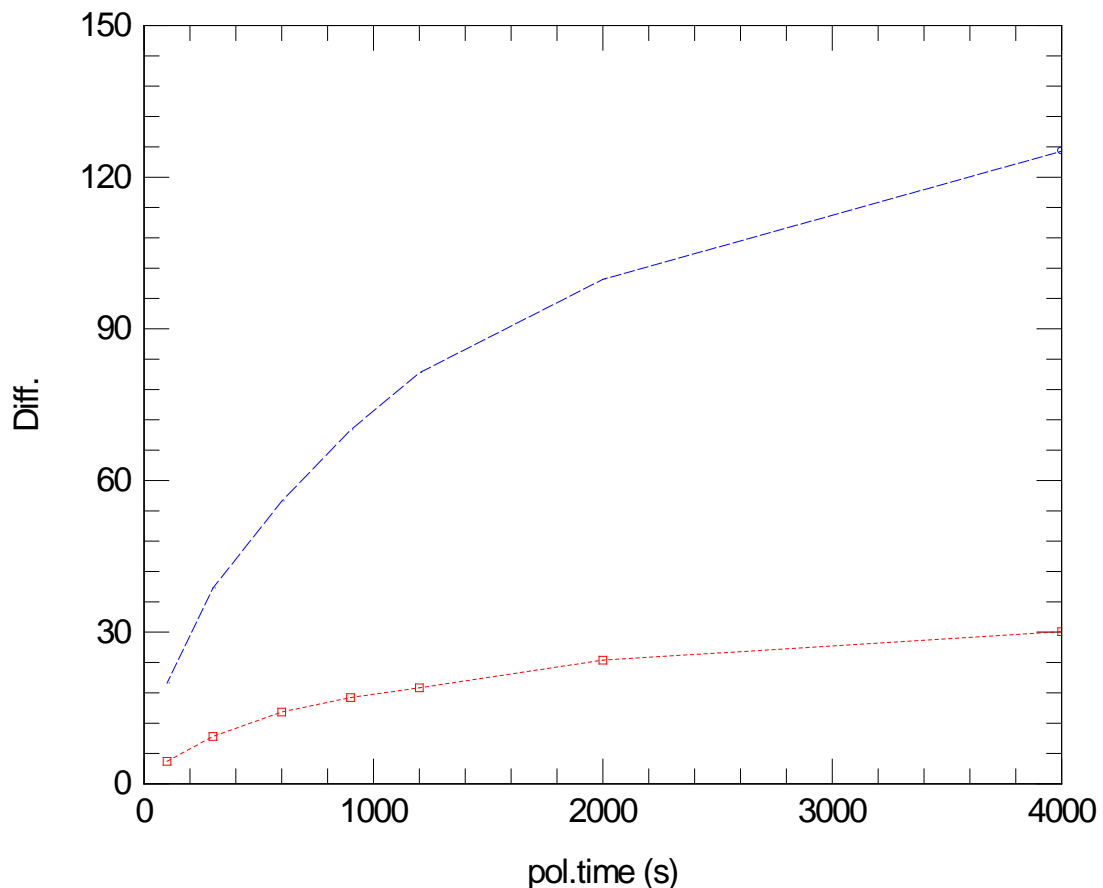


Figure 5.11: The difference between the peak and the average of the baseline for the curves which represent the changing of the polarization time for the *b*- peaks at the 290 G (○) and 180 G (□) irradiation fields, versus polarization time.

5.3 The effect of changing the irradiation time on the spectrum:-

This investigation can give estimation plots of the transition probability arising from rf irradiation.

5.3.1 The effect of changing the irradiation time in the 180 G low field case:-

To investigate the transition probability in response to rf irradiation the b -, b + and a + peaks were studied as a function of rf irradiation time (0.5, 1, 2, 4, 5, 10, 15, 20) s at 180 G. The initial polarization was conducted at 1 T for 600 s. Contact between the Zeeman and tunnelling reservoirs was conducted at the level crossing, 130 G, for 2 s. The final measurement was made at the resonance field of 8525 G. The peak amplitude was determined by taking the difference between the peak and the average of the baseline for the various peaks in the spectrum; the data are collated together in Fig.5.12.

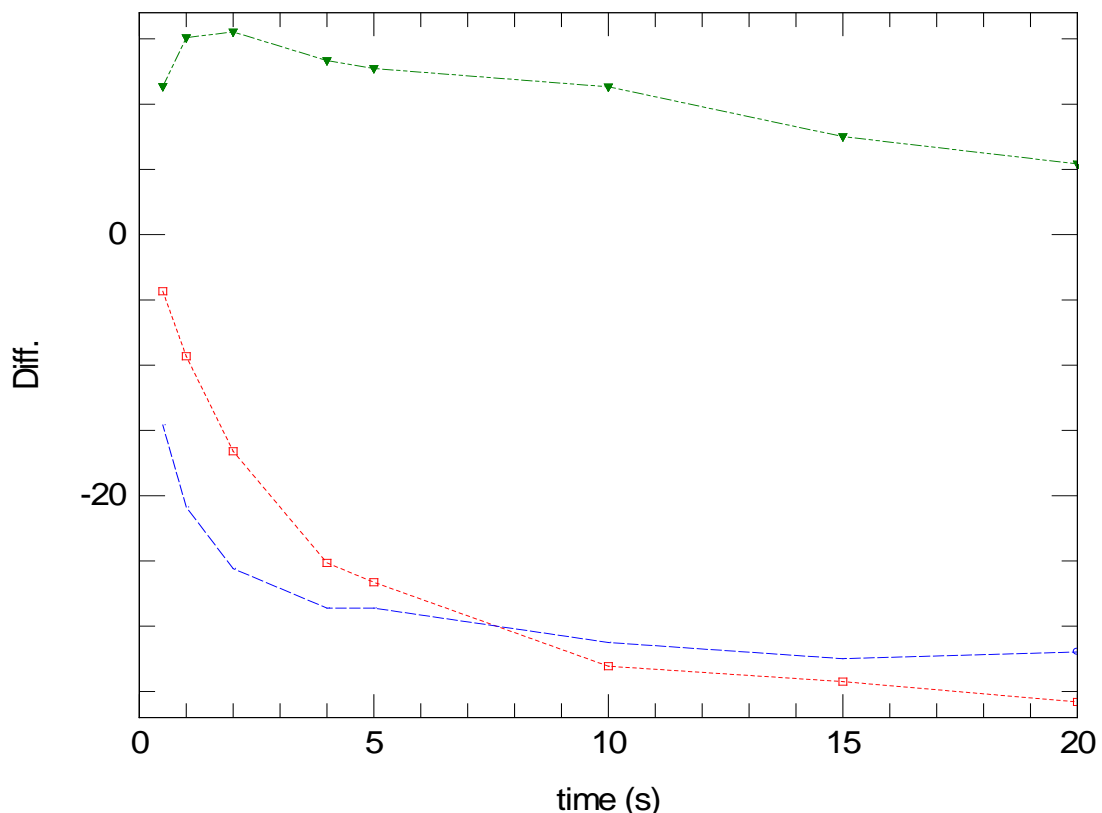


Figure 5.12: The difference between the peak and the average of the baseline for the curves which represent the changing of the irradiation time for the b - (\blacktriangledown), b + (\square) and a + (\circ) peaks at the 180 G irradiation field, versus irradiation time.

We notice that the $b-$ will increase at the first part of the curve (0.5, 1, 2) s and then decrease at the second part of the curve (5, 10, 15, 20) s, so at short times there will be an effective process of destroying the Zeeman reservoir and enhancing the tunnel reservoir, while at long times there will not be an effective process of destroying the Zeeman reservoir and enhancing the tunnel reservoir. There is an explanation for this behaviour in that at short times the relaxation rate is very small so the peak will rise, while at longer times the relaxation rate will be higher and the curve will decrease and this because we are close to the level crossing region where at short times there is still an energy transition from Zeeman to tunnel reservoirs which will disappear at longer times. What we are supposed to get is that at low field 180 G the tunnelling reservoir will get a high energy while the Zeeman (spin) reservoir will get small energy because low field produces a high energy splitting in the energy levels of the Zeeman reservoir which will leave the tunnelling reservoir with small energy splitting, so maybe it will be better to try the same experiment but with a higher field far away from the level crossing region.

We notice that by increasing the low field time there is a fixed behaviour of increasing the base line and decreasing the peak which results in the curve as a decrease in the difference values of $a+$ as irradiation time increases and we can explain this by the fact that at short times there is always a value for the transition probability per unit time which results as an increase in the baseline value and a decrease in the peak value, but then the levels (A and E) are saturated and there will be no value for the transition probability per unit time and hence a decrease in the peak value and a stable high baseline value.

We notice that the same behaviour appears as in the $b+$, which is also because of the saturation of the levels (A and E).

5.3.2 The effect of changing the irradiation time in the 290 G low field case:-

The irradiation time dependence provides a measurement of the transition probability and also helps to optimise the DTP spectra you are recording.

1. Firstly we study the *b*- peak at different irradiation times (0.5, 1, 2, 4, 7, 10, 15, 20) s at 290 G where we polarize the system before that at 1 T for 600 s taking 2 s to saturate the sample following by a 2 sec transfer to the level crossing at 125 G, ending with a measurement pulse at the resonance field of 8525 G. By taking the difference between the peak and the average of the baseline of the previous *b*- peak, we have Fig.5.13. We notice from the figure that by increasing the irradiation field from 180 G to 290 G, the previous behaviour of the difference curve, which was an increase followed by a decrease, will disappear.

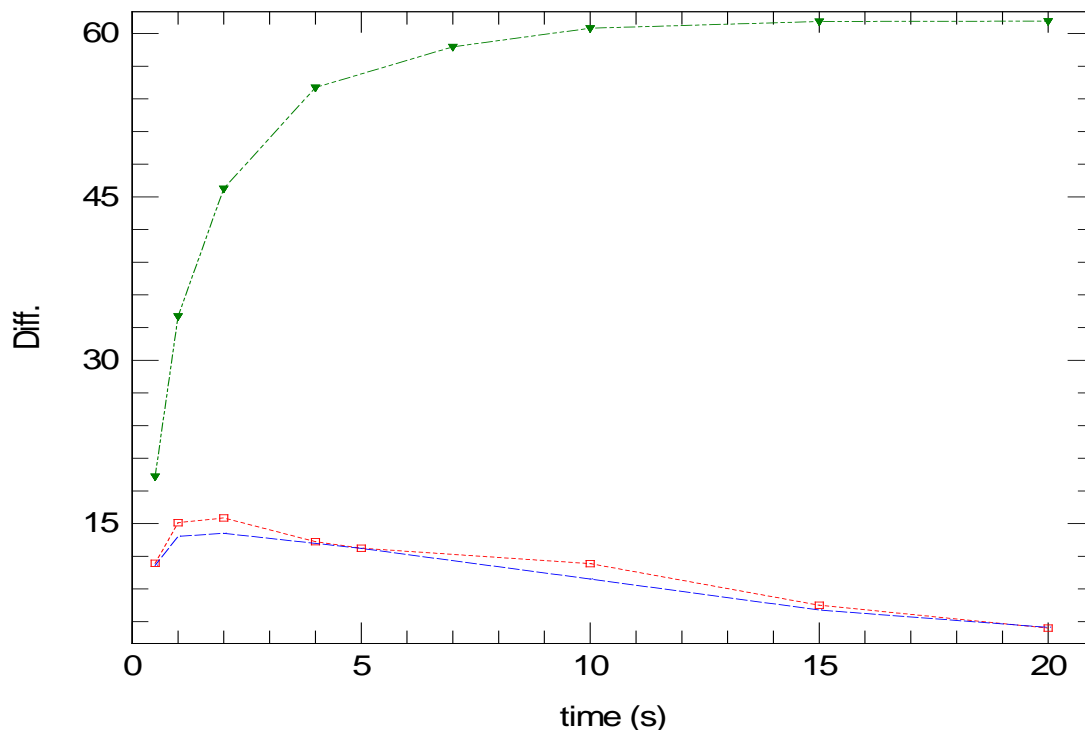


Figure 5.13: The difference between the peak and the average of the baseline for the curves which represent the changing of the irradiation time for the *b*- peaks at the 290 G irradiation field (\blacktriangledown), versus irradiation time, comparing it with the first and second 180 G scans for the *b*- (\circ , \square).

Also the difference curve saturated after 7 s and this is because 180 G was all inside the level crossing region, and hence the transitions from Zeeman to tunnelling reservoirs will be not very effective and there will be some energy inside Zeeman reservoir after the irradiation process, while in the irradiation field of 290 G there will be no contact between the two reservoirs and the contamination of the transitions will be small, and the curve show that the saturation happens after 7 s because both of the levels (*A* and *E*) will have the same population after 7 s which is a specific property of this sample.

2. Secondly we study the *a+* peak using the same steps in 1. By taking the difference between the peak and the average of the baseline of the previous *a+* peak, we have Fig.5.14, we see that it is identical to the behaviour of the previous 180 G scan of the *a+* but with a big increase in the negative direction because we avoid the contamination of the irradiation process at 180 G, so at the end we find that both of 180 and 290 G have the same result of negative decay as the irradiation time increases.

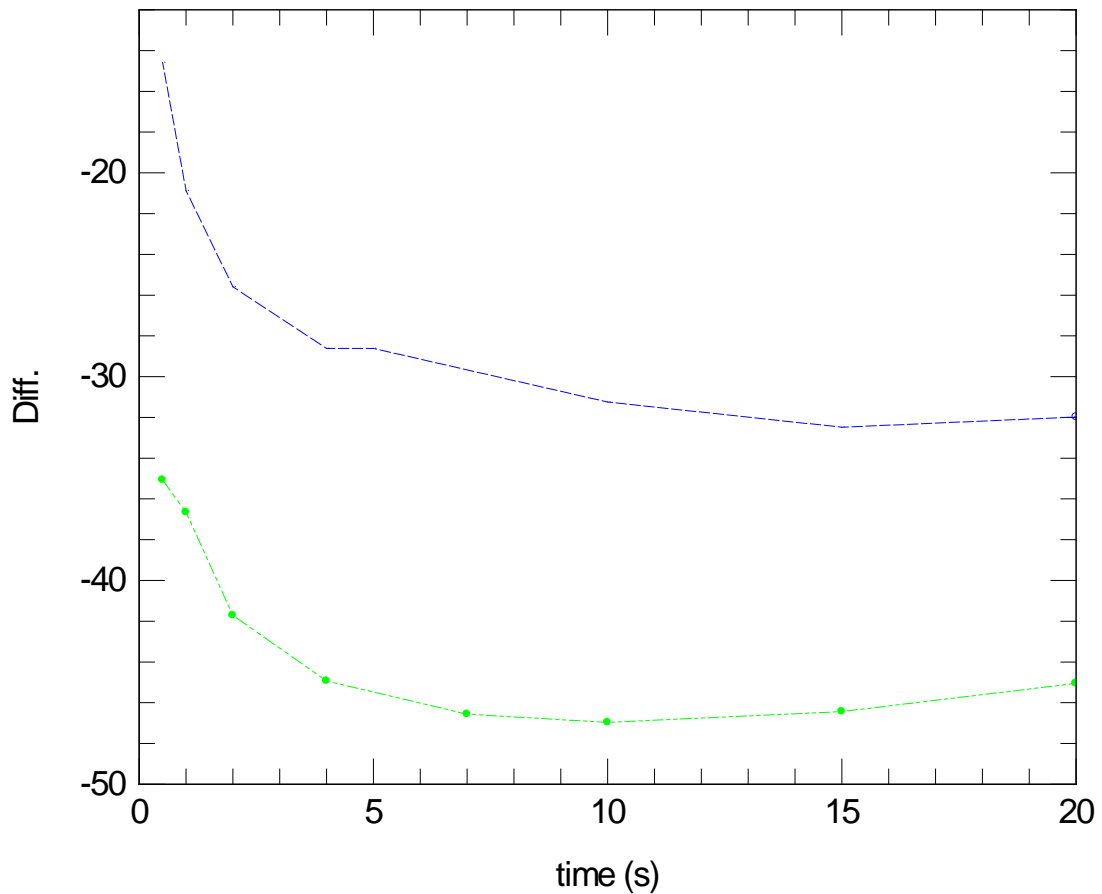


Figure 5.14: The difference between the peak and the average of the baseline for the curves which represent the changing of the irradiation time for the $a+$ peak at the 290 G irradiation field (●) versus irradiation time, comparing it with the first 180 G scan for the $a+$ (○).

3. We study the $a-$ peak using the same steps in 1. By taking the difference between the peak and the average of the baseline of the previous $a-$ peak, we have Fig.5.15, where we do not have a 180 G scan version because we could not recognize it very clearly. We notice that it saturates after 4 s which depends on the strength of the radio frequency field.

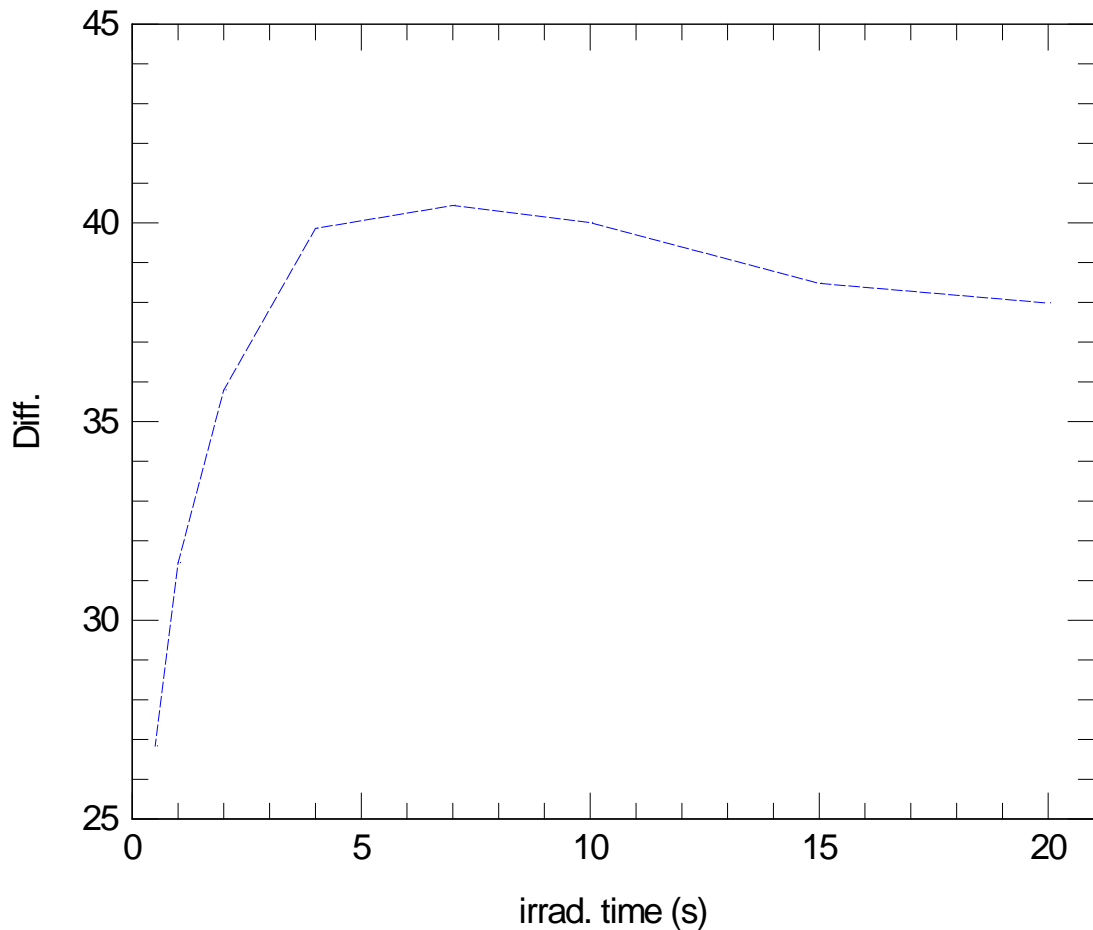


Figure 5.15: The difference between the peak and the average of the baseline for the curves which represent the changing of the irradiation time for the *a*- peak at the 290 G irradiation field, versus irradiation time.

4. Now we study the *b*+ peak using the same steps in 1. By taking the difference between the peak and the average of the baseline of the previous *b*+ peak, we have Fig.5.16, we see that it is identical to the behaviour of the previous 180 G scan of *b*+ apart from a big increase in the negative direction because we avoid the contamination of the irradiation process at 180 G, so at the end we find that both of 180 and 290 G scans have the same result of negative decay as the irradiation time increases.

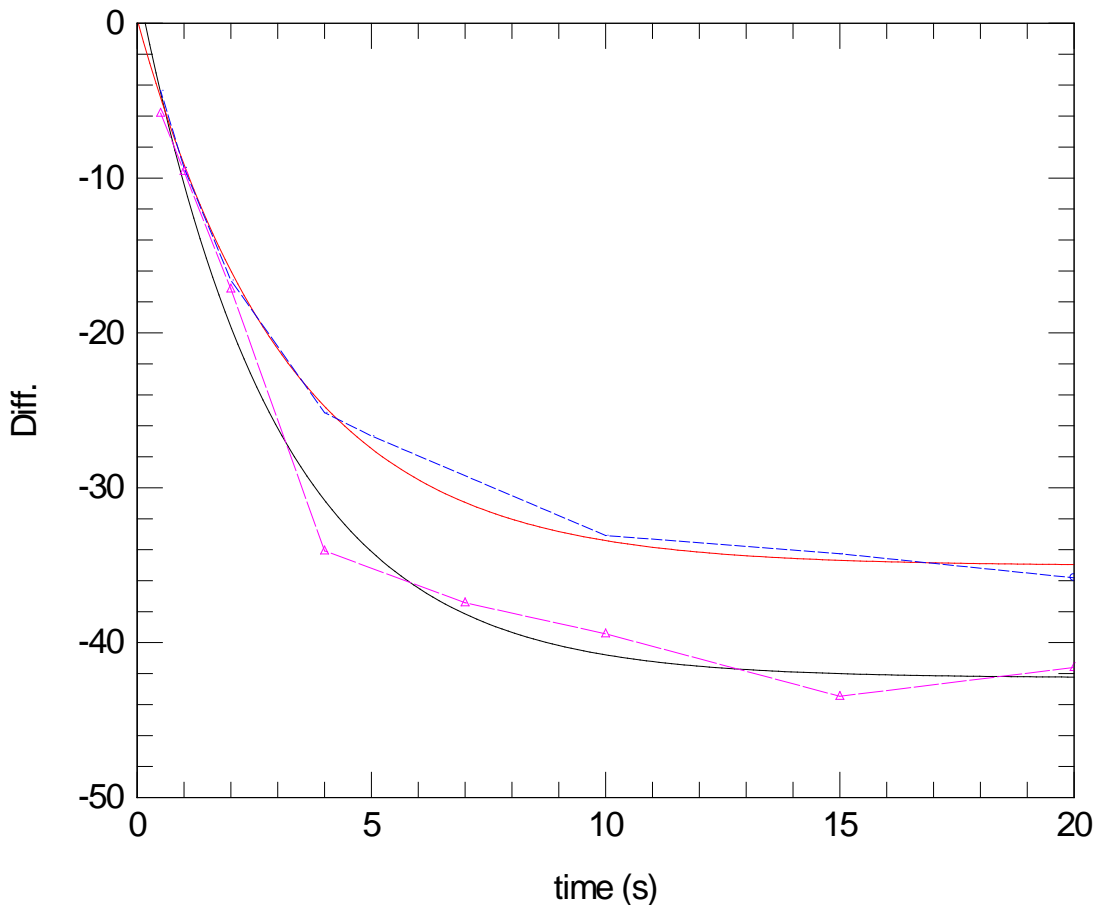


Figure 5.16: The difference between the peak and the average of the baseline for the curves which represent the changing of the irradiation time for the $b+$ peak at the 290 G irradiation field (Δ) versus irradiation time, comparing it with the first 180 G scan for the $b+$ (\circ).

By fitting these curves to a T_1 expression $y=a * \exp(-x/b) + c$ shown as solid lines, the time constant 'b' for the two curves are 2.93 and 3.25 which are roughly the same.

5.4 The spin-lattice relaxation time T_1 measurements:-

Our main reason for doing these experiments was to calibrate the magnetisation signal we measure in terms of a Zeeman polarization or a Zeeman inverse temperature.

1. We start by measuring T_1 at the temperature 4.2 K, and for the measurement field 1 T, with the resonance field of 8525 G, we get the following approximate value for $T_1=2247$, as shown in Fig.5.17, where the value of M_o is 96.3. The attenuation ratio is

28, so we can find the value of M_o at 1 T and 4.2 K for 0 dB by multiplying this ratio 28 by the value of M_o we get from Fig.5.17, which is 96.3, and from the relation $(M_o = (K \times B)/T)$ we can conclude that (K) has the approximate value $(K=(96.3 \times 28 \times 4.2)k/1T \approx 11325(k/T))$ which we can use to express the spectrum in Zeeman temperature terms by using the previous y axis M_z values in the relation :- $(M_z = (K \times B)/T_z)$. Also we can use these T_z values to express the spectrum in the population term instead of T_z values by substituting its values in the relation: - $(N = \frac{y^* h^* B}{2^* k_B^* T_z})$.

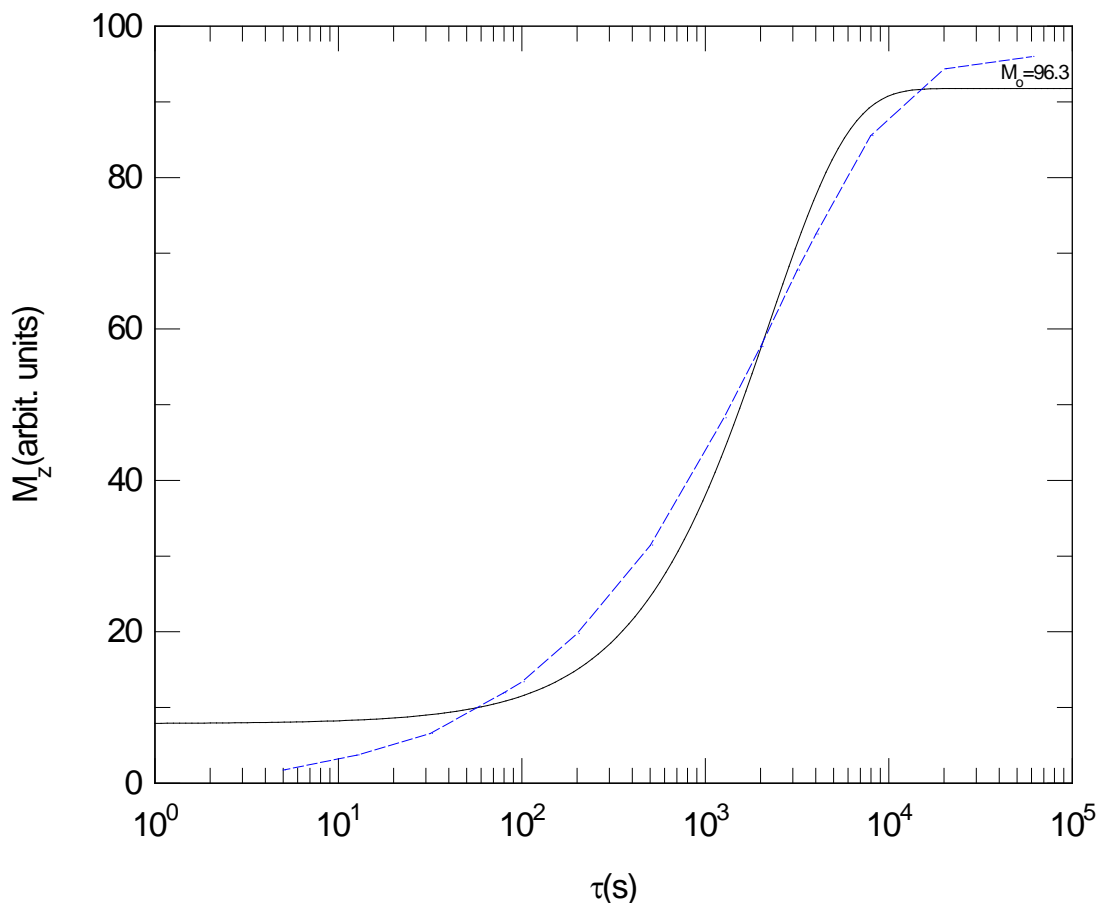


Figure 5.17: The spin-lattice relaxation time T_1 measurement, 4.2 Kelvin, 1T, and we fit the curve to the equation $y=a*exp(-x/b) + c$ shown as solid lines.

2. Secondly we measure T_1 at the temperature 4.2 K and for the measurement low fields 125 and 290 G, with the resonance field of 8525 G, and we get the following approximate values for $T_1=516$ and 571 where we expect at low field to get small values

of T_1 so it will be faster to relax, but we notice here that T_1 is still quite long, as shown in Fig.5.18, where the value of M_o is 44.12 and 88.5 respectively.

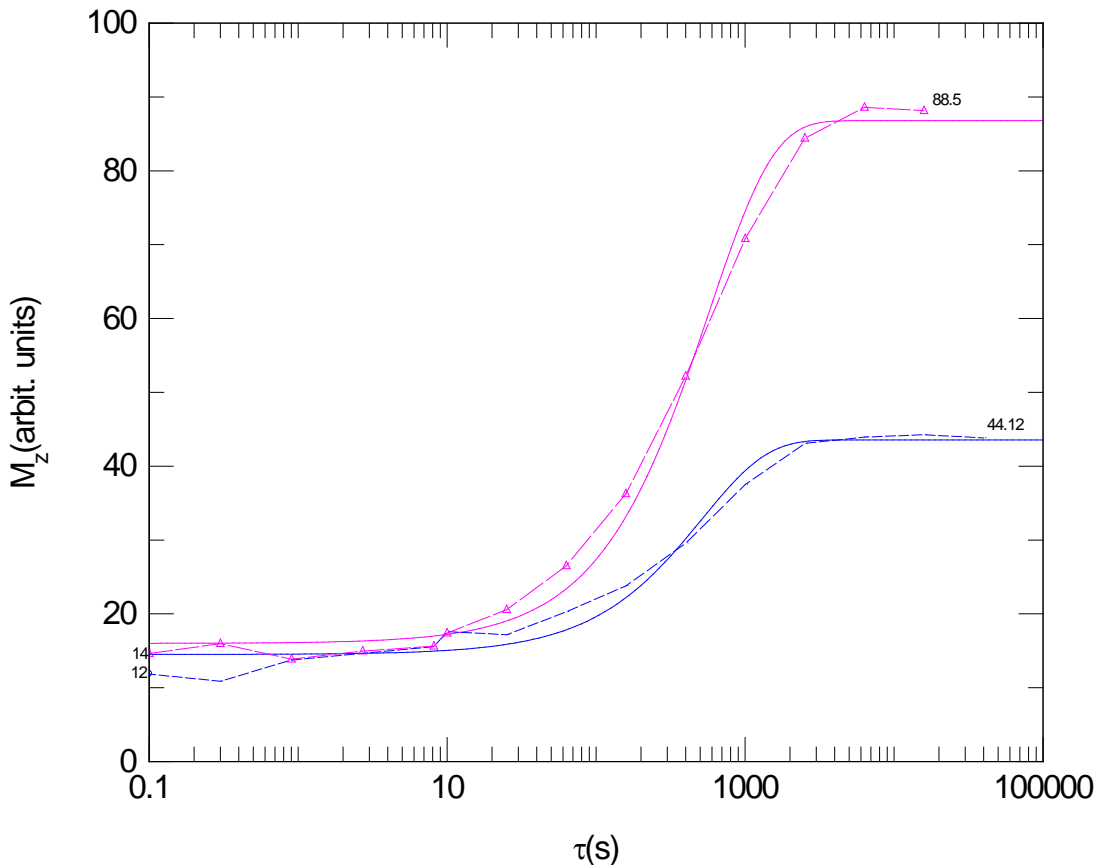


Figure 5.18: The spin-lattice relaxation time T_1 measurement, 4.2Kelvin, 1T, 125 (○) and 290 (△) G, and we fit both curves to the equation $y=a*\exp(-x/b) + c$ shown as solid lines.

By measuring the constant (K) from the relation ($M_o = (K \times B)/T$) for both 125 and 290 G fields we get the values ($K = (44.12 \times 4.2) \text{ k}/0.0125 \text{ T} \approx 14824 \text{ (k/T)}$), ($K = (88.5 \times 4.2) \text{ k}/0.029 \text{ T} \approx 12817 \text{ (k/T)}$) and by comparison to the value we get for 1 T which is approximately (11325 (k/T)), we find a good similarity between them with small differences and if we take the average of them we get the approximate value of (12989 (k/T)) for the constant K . We notice from Fig.5.18 that the baseline signal appears to be field independent, and we can confirm this by subtracting its (decay of the baseline) value which is a little bit of dead time appearing as a signal from the value of M_o .

connecting to the field values, so we get two measurements of M_o which are agree with each other as in the following calculations:- $((88.5-14) \times (115 / 280)) = (44.12-12)$) and the result is :- (30.6=32.12) so there is approximately a good identity between them, where we subtract the offset 10 from the field values 125 and 290 G.

5.5The level crossing spectrum:-

In this section we shall investigate in more detail the step in the DTP sequence where the tunnelling polarization is measured by bringing the tunnel reservoir into contact with the saturated Zeeman reservoir. This is achieved by setting the value of the level-crossing field. This is the field at which the two reservoirs are equilibrated and by making this a variable in the experiment we shall be able to map out the level-crossing region.

Experiments were conducted using the DTP sequence in Fig.4.3. The amplitude of the b - peak was measured as a function of B_{LC} , the setting of the level-crossing field in the sequence. For these experiments the polarization field $B_{pol}=1$ T and the polarization time was 600 s. The b - transition was irradiated with rf for 5 s at 290 G. The amplitude of the b - as a function of B_{LC} is shown in Fig. 5.19. Given the tunnelling frequency in MEK was earlier measured as 485 KHz, we expect the $\Delta m=1$ level crossing to occur at 120 G. Surprisingly, we observe polarization transfer between the Zeeman and tunnelling reservoirs at much higher fields. Indeed polarization transfer is observed as high as 260 G, which is twice the expected level crossing field. This indicates that a single proton spin flip is leading to $A-E$ transitions in two tunnelling methyl groups simultaneously. Therefore, this provides compelling evidence for a mechanical coupling between methyl groups which can be explained by the level-crossing energy level diagram shown in Fig. 5.20. In Fig.5.19, the double tunnelling transition appears as a peak centred on 240 G. This corresponds to $AA - EE$ transitions in the material. The

conventional $\Delta m=1$ level crossing also reveals itself as a peak at 120 G and at fields less than 60 G, which is the $\Delta m=2$ level crossing, the DTP amplitude becomes smaller. Due to the efficiency of the Zeeman-Tunnel contact, the plot represents an integrated effect as the field switches through various level crossing contacts on its way to the set value of B_{LC} , therefore, the line shapes are complex.

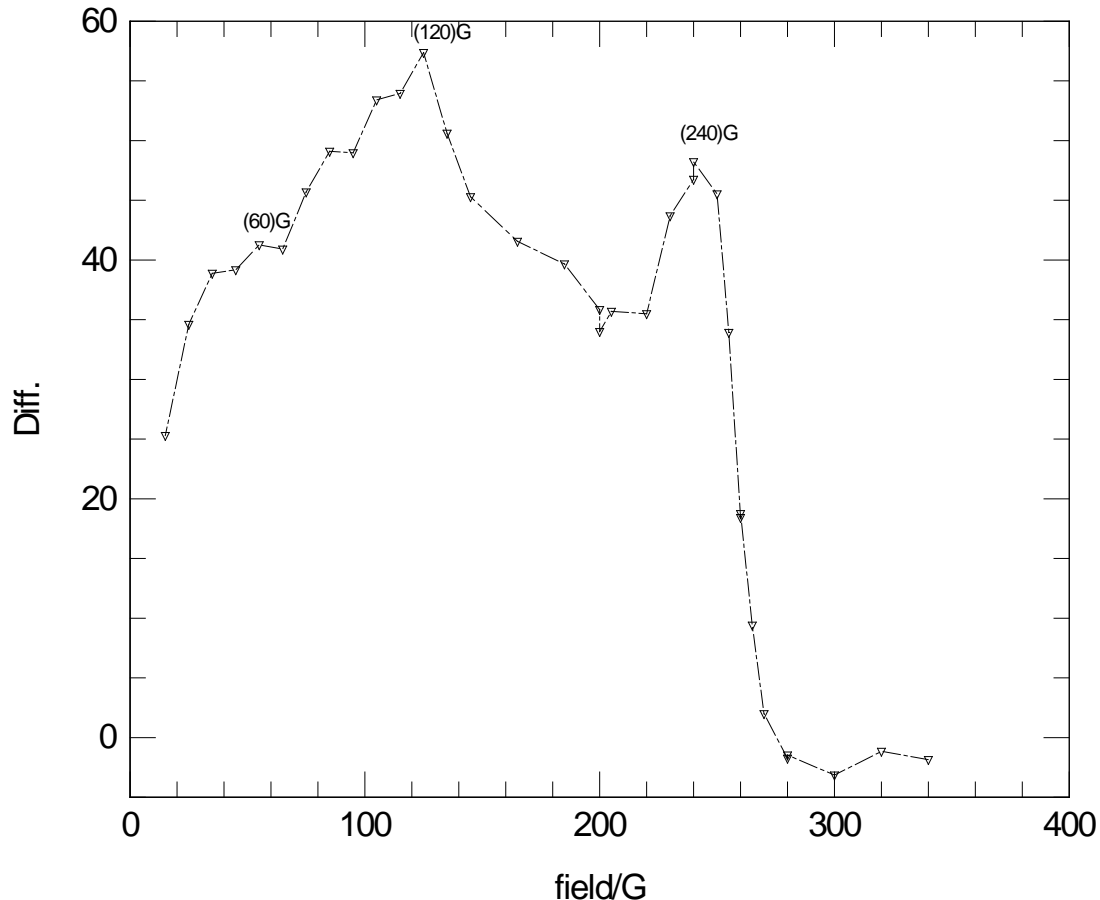


Figure 5.19: The difference between the peak and the average of the baseline versus the level crossing field value in the b -region.

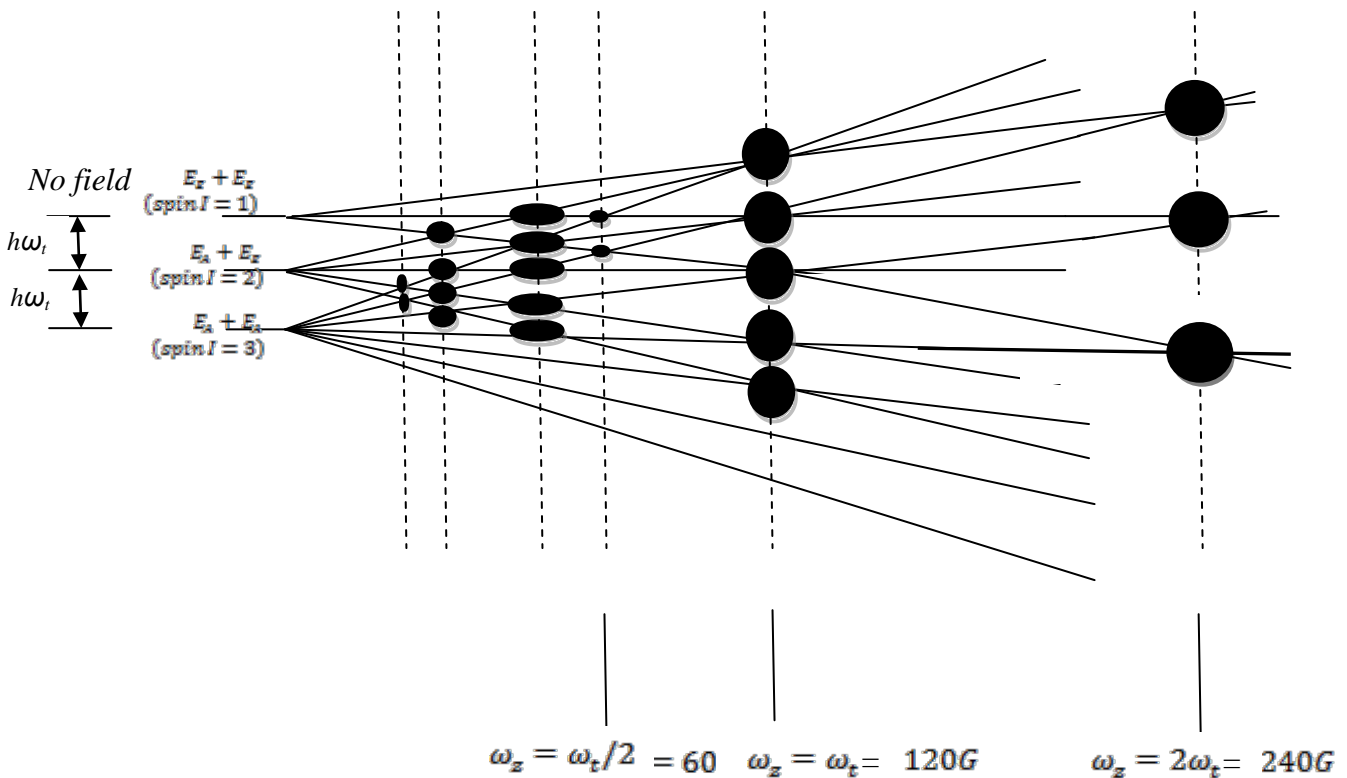


Figure 5.20: Zeeman-tunnel level-crossing in the rotating frame for longer irradiation times.

5.6 Measuring the lifetime (tunnelling relaxation time) of the A and E states:

relaxation of the tunnelling reservoir:-

The effect of rf irradiation is to disturb the tunnelling system away from equilibrium.

Therefore, the opportunity arises to measure the lifetime of the A and E tunnelling states.

The recovery towards equilibrium of the tunnelling reservoir can be monitored by

introducing a relaxation time interval between rf irradiation and saturation of the

Zeeman reservoir, as shown in Fig. 5.21. The effects of relaxation were studied as a

function of relaxation time interval and field at which the relaxation was conducted.

The results are compiled in Fig. 5.22.

1. We start by trying 8 kG as the tunnel relaxation field value as shown in Fig. 5.21 step1 where we polarize the system at 1 T for 600 s and irradiate it at 290 G for 5 s, using 8525 G as a saturation and measurement field with level crossing at 125 G, reaching it by a 2 s delay, and we vary the saturation delay time between (1, 10, 100, 500, 1000, 1800, 3000, 6000) s.

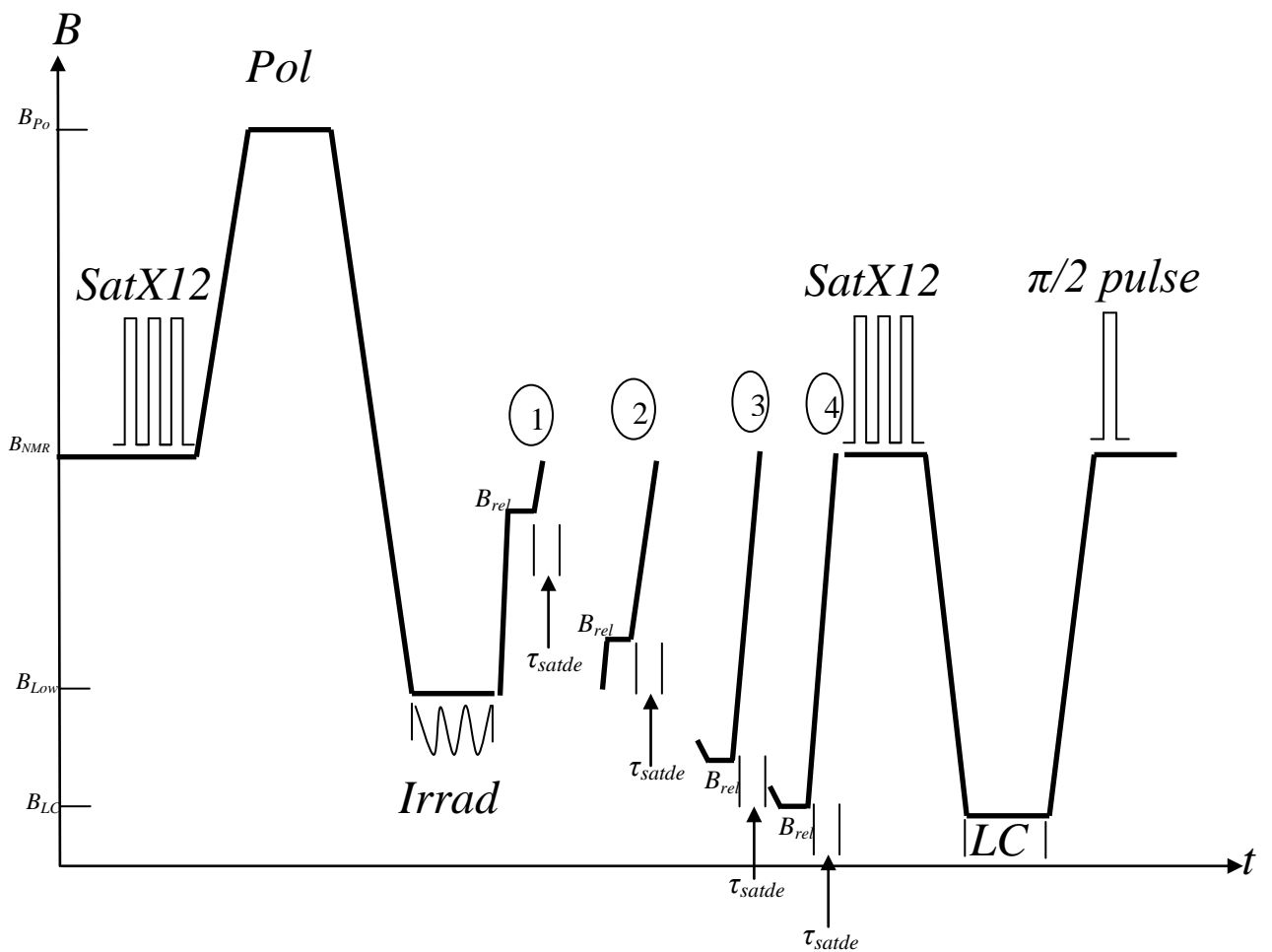
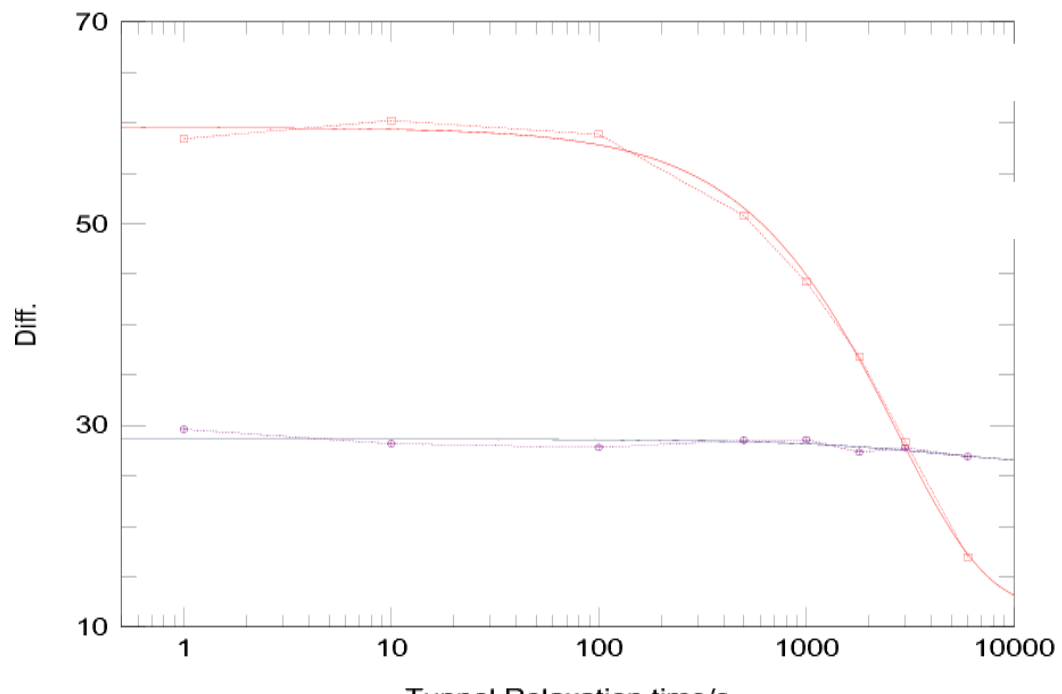
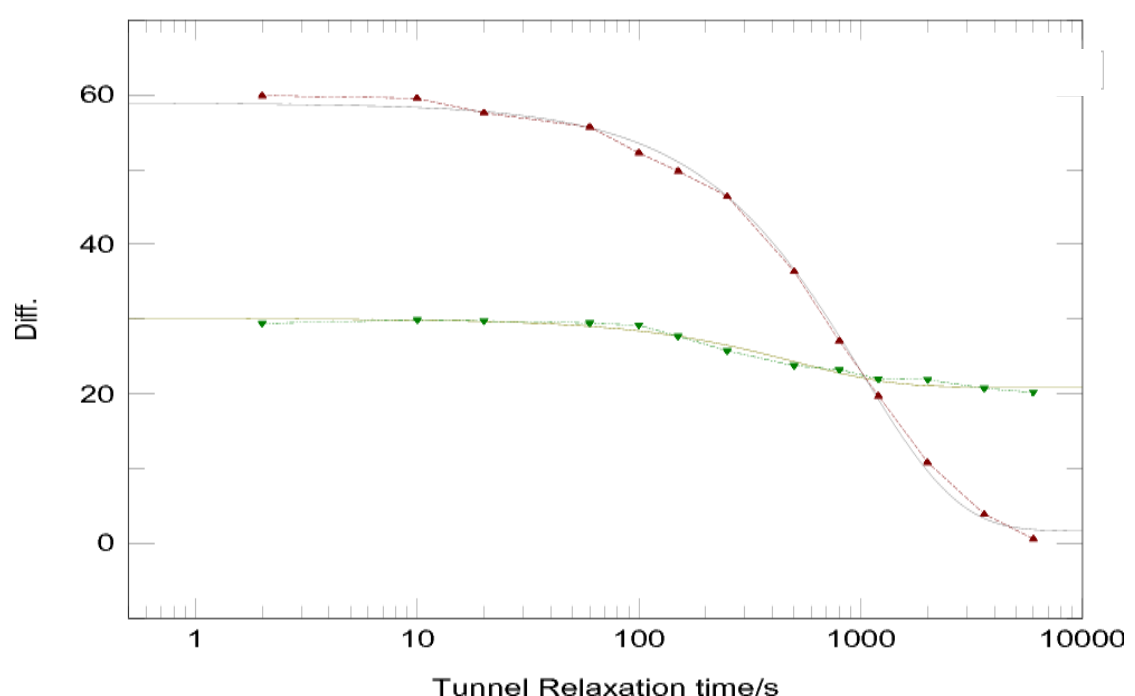


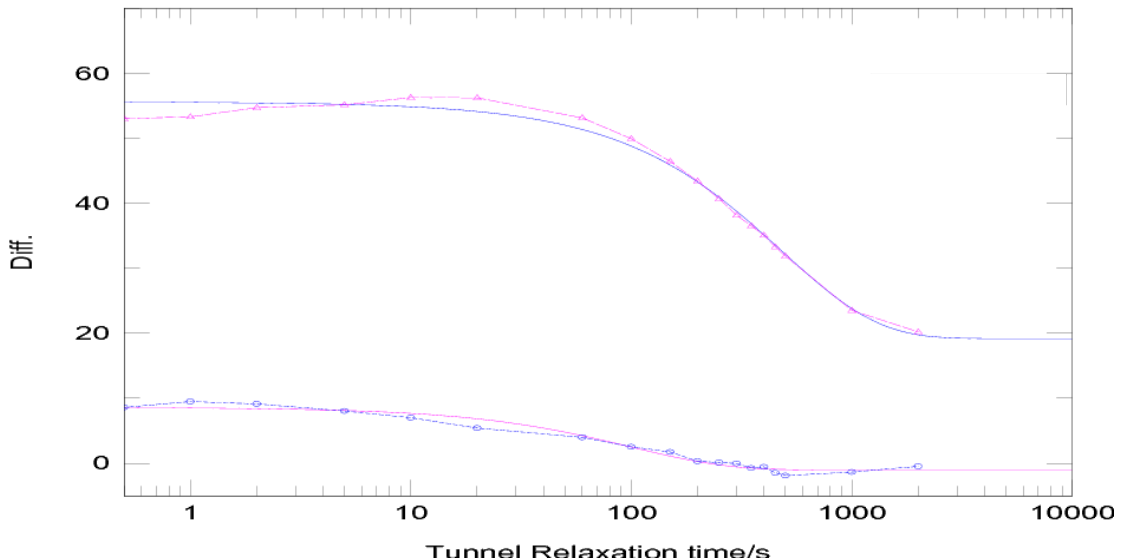
Figure 5.21: The pulse sequence using different tunnel relaxation field value.



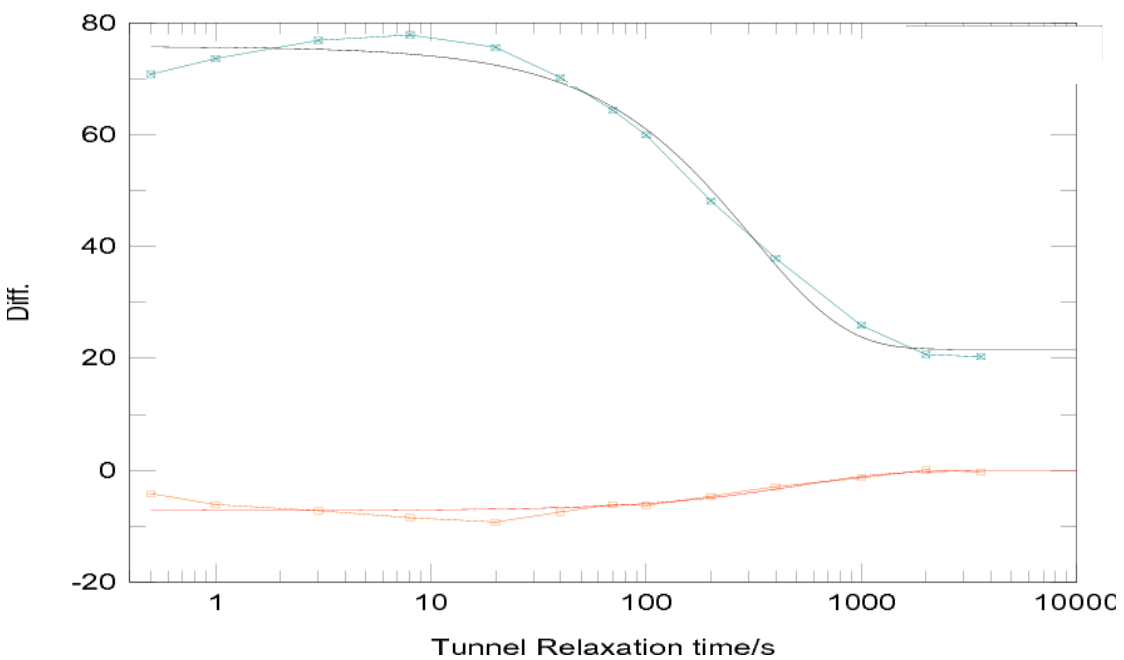
[1]



[2]



[3]



[4]

Figure 5.22: The difference between the peak and the average of the baseline (\square , \blacktriangle , \circ , \square) and the average of the baseline (\circ , \blacktriangledown , \blacktriangle , \square) versus time of saturation delay time:-
 [1] (1, 10, 100, 500, 1000, 1800, 3000, and 6000) s for 8 kG as the tunnel relaxation field value.

[2] (2, 10, 20, 60, 100, 150, 250, 500, 800, 1200, 2000, 3600, and 6000) s for 300 G as the tunnel relaxation field value.

[3] (0.5, 1, 2, 5, 10, 20, 60, 100, 150, 200, 250, 300, 350, 400, 450, 500, 1000, and 2000) s for 200 G as the tunnel relaxation field value.

[4] (0.5, 1, 3, 8, 20, 40, 70, 100, 200, 400, 1000, 2000, and 3600) s for 125 G as the tunnel relaxation field value, and we fit all curves to the equation $y=a*\exp(-x/b) + c$ shown as solid lines.

By plotting the difference between the peak and the average of the baseline as shown in Fig.5.22 (part [1]) we notice that there is a fixed approximate value of the baseline where the decay time is ($b = 4537$ s) and hence its relaxation rate is ($1/b = 0.0002$ s $^{-1}$) which is very small, and for the difference curve there is a tunnelling relaxation after 100 s and the decay time b is equal to approximately 2726 s which leads us to the relaxation rate $1/b$ equal to 0.0003 s $^{-1}$ which is also a small value, meaning that there is a little loss of energy. So we will try another field value, like 300 G, that is smaller than 8 kG but it still outside the level crossing region.

2. Secondly we try 300 G as the tunnel relaxation field value as shown in Fig.5.21 step 2, using the same previous steps, and we vary the saturation delay time between (2, 10, 20, 60, 100, 150, 250, 500, 800, 1200, 2000, 3600, 6000) s.

By plotting the difference between the peak and the average of the baseline as shown in Fig. 5.22 (part [2]) we notice that there is a slight change for the approximate value of the baseline where the decay time is ($b=507$ s) and hence its relaxation rate is ($1/b=0.0019$ s $^{-1}$) which is higher than the 8 kG value and for the difference curve there is a tunnelling relaxation after 10 s and the decay time b is equal to approximately 1016 s which leads us to the relaxation rate ($1/b$) equal to 0.0009 s $^{-1}$ which is a high value compared to that for 8 kG. This because we are close to the level crossing peak region

240 G and there is a start of the effect of the coupling between Zeeman and tunnelling reservoirs which leads to contaminate the transitions between them by new ones and this appears more efficient in the different baseline positions. This leads us to try values of field inside the level crossing region, starting with 200 G between the 120 G and 240 G peaks and the other at the level crossing peak region 120 G at 125 G, and we expect to get a larger relaxation rates since the coupling between the Zeeman and tunnel reservoirs will be very large.

3. Now we try 200 G as the tunnel relaxation field value as shown in Fig.5.21 step 3, using the same previous steps, and we vary the saturation delay time between (0.5, 1, 2, 5, 10, 20, 60, 100, 150, 250, 300, 350, 400, 450, 500, 1000, 2000) s.

By drawing the difference between the peak and the average of the baseline as shown in Fig. 5.22 (part [3]) we notice that there is a large difference between the base line positions and a little more relaxation of the baseline where the approximate decay time is ($b=484$ s) and hence the relaxation rate is ($1/b=0.002$ s⁻¹) which is similar to the 300 G value for the difference curve.

There is a tunnelling relaxation after 10 s and the decay time b is equal to approximately 99 s which lead us to the relaxation rate ($1/b$) equal to 0.01 s⁻¹ which is a high value meaning that there is a high loss of energy.

4. Finally we try 125 G as the tunnel relaxation field value as shown in Fig.5.21 step 4, using the same previous steps, and we vary the saturation delay time between (0.5, 1, 3, 8, 20, 40, 70, 100, 200, 400, 1000, 2000, 3600) s.

By drawing the difference between the peak and the average of the baseline as shown in Fig. 5.22 (part [4]), we notice that there is a larger difference between the baseline positions and a large relaxation of the baseline where the decay time is approximately ($b=314$ s) and hence its relaxation rate is ($1/b = 0.003$ s⁻¹) which is higher than the 200

G value. For the difference curve there is a tunnelling relaxation after 10 s and the decay time b is equal to approximately 510 s which lead us to the relaxation rate ($1/b$) equal to 0.0019 s^{-1} which is small compared with the 200 G value, but it is still high meaning that there is still a high loss of energy.

5. By collecting all the curves of the difference between the peak and the average of the baseline and the average of the baseline versus time of saturation delay time for (8000, 300, 200, 125) G as tunnel relaxation field value as shown in Fig. 5.23, we notice firstly that for the 8000 and 300 G the difference curves appear up while the baseline curves appear down and this is because we are away from the level crossing region, so all the transitions will be directed to increase the peak value and there will be no contaminated transitions converted to the baseline value, while for the fields inside the level crossing region 200 and 125 G the transitions will be contaminated because there is a large coupling between the Zeeman and tunnel reservoirs leading to new transitions that enhance the baseline values, on the account of the peak values leading to make the baseline curves appear up in the curve while the difference curves appear in the lower region. We fit these curves to the equation $(a * \exp(-x/b) + c)$, where (a) is the amplitude of the peak (in arbitrary units) and it takes the approximate values (-7, 10, 57, 48) for the difference curves of the fields (125, 200, 300, 8000) G respectively.

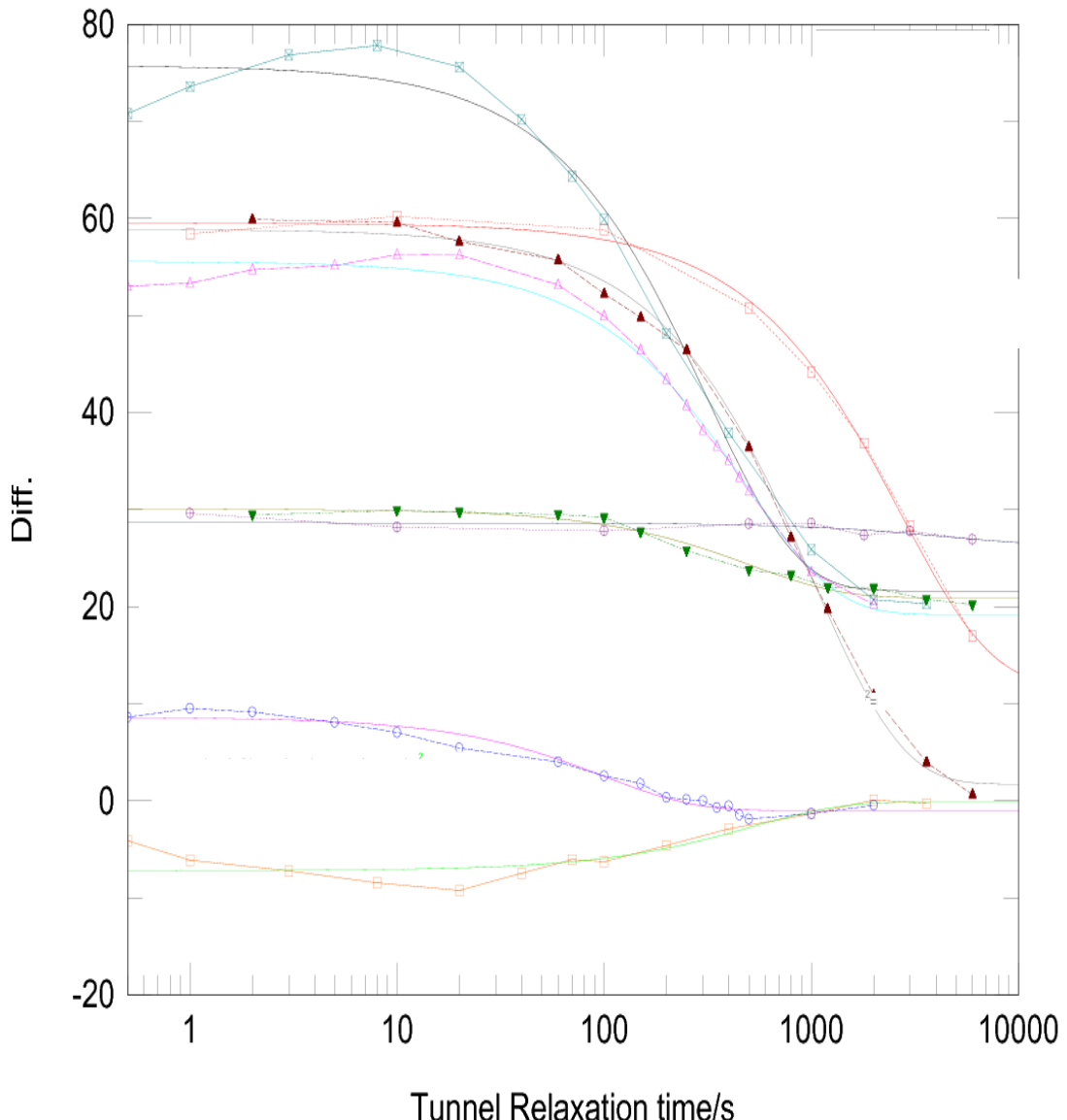


Figure 5.23: The difference between the peak and the average of the baseline (\square , \blacktriangle , \circ , \square) and the average of the baseline (\circ , \blacktriangledown , \blacktriangle , \square) versus time of saturation delay time for (8000, 300, 200, and 125) G as the tunnel relaxation field value, and we fit all curves to the equation $y=a*\exp(-x/b)+c$ shown as solid lines.

Because 125 and 200 G are inside the level crossing region where there is a good contact which yields a small amplitude because the polarization at the start goes to a higher different baseline, this is the reason for getting the baseline up and the difference curve low in the graph, while outside the level crossing region 300 and 8000 G we get the reverse behaviour where the difference curve appears up and the baseline lower

because we have a small coupling between the two tunnel and Zeeman reservoirs. The approximate (a) values for the baseline curves are (54, 36, 9, 2.3) for the fields (125, 200, 300, 8000) G respectively because the peaks get much smaller because the tunnel reservoir is relaxing to the spin system (Zeeman reservoir), so the tunnelling reservoir will be damped rather than the Zeeman reservoir in the irradiation step. For b , which represents the tunnel relaxation time and the inverse of it ($1/b$), which represents the tunnel relaxation rate, it has the approximate values (510, 99, 1016, 2726) for the fields (125, 200, 300, 8000) G respectively for the difference curves and this is because in the low field region 125 and 200 G level crossing region there will be a contact between the tunnel and Zeeman reservoirs so it will cool the tunnel reservoir very quickly, and for fields above the level crossing region 300 and 8000 G we get long relaxation times because there is very small contact between the two reservoirs, so it will cool the tunnel reservoir very slowly and there will be a lot of energy to appear as amplitude at the end. While (b) approximate values for the baseline curves are (314, 484, 507, 4537) for the fields (125, 200, 300, 8000) G respectively and it gives a correct behaviour in that inside the level crossing region we have a small relaxation time which leads to a faster relaxation because of the coupling between the Zeeman and tunnel reservoirs, where outside it there is a high relaxation time and this will lead to a long relaxation. Here c represent an offset which gives the equilibrium value to bring the system to equilibrium, where for the difference curves it takes the approximate values (-0.13, -1, 2, 12) for the fields (125, 200, 300, 8000) G respectively, and it increases because of the switching rate, where if it is long it will enhance more transitions, while c has the approximate values (22, 19, 21, 26.3) which are almost constant on the approximate value 22.

5.7 The relative heat capacity:-

At the level-crossing step in the DTP experiment, the tunnel reservoir is rapidly brought to equilibrium with the saturated Zeeman reservoir. The inverse temperature that these two reservoirs attain is dependent on the relative heat capacities of the two reservoirs. Therefore, by making repeated contacts as shown in the pulse sequence of Fig. 4.12, we shall be able to estimate the relative heat capacities of the reservoirs, a measurement of the inverse temperature acquired by the two reservoirs can be obtained by recording an FID at each step. They systematically decay with each level crossing contact. Plotting the FID amplitude as a function of the number of level crossing contacts we arrive at Fig. 5.24.

We make a relative heat capacity measurements by adding 8 level crossing and measurement steps, and a saturation step before them, to the pulse sequence in Fig.4.12 where we polarize the system at 1 T for 600 s, and for a long time 3600 s to get a large signal, and irradiate it at 290 G for 5 s, using 8525 G as a saturation and measurement field with level crossing at 125 G reaching it by a 2 s delay, and using a tunnel relaxation field 8000 G and, since we do not want to relax the system, also we make the saturation delay time 2 s. And we accomplish this 8 pulse sequence by adding it to the (NTNMR) program window only and change the visual basic program so it prevents the program from making a Fourier transform after the measurement has ended.

We will make this change manually where we create a new feature in visual basic program named *2D* and with it we can see the nine signals, where the ninth one represents the measurement of the baseline and then we click on ‘get data’ once at the start of the analysis and then from commands icon we choose ‘data manipulation’ and then separate records of nine segments will appear as a window where we can choose the specific free induction decay (FID) signal to analyze. Then also from the commands window we choose only for the first signal and we will analyze the data manipulation (left shift) option and then the baseline correction followed by the apodization (a mathematical transformation carried out on data received from a spectrometer to alter the instrument’s response function before the Fourier transformation is calculated to obtain the spectrum) process (exponential multiplication) to reduce the noise. Finally we reach the stage of transform (Fourier transform) and then auto phase 0 and 1 finishing with the baseline correction after the Fourier transform and then we choose the region we want to integrate from the options icon and selecting the integrals option by specifying a window and then choose ‘add’ to get the measure of the signal amplitude. We make the measurements at the frequencies 1680 and 1880 kHz (on resonance for the *a+* and *b-* respectively) and 1980 kHz (off resonance) as shown in Fig.3.9 where we fit the curves to an exponential equation decay to give the decay factor *b* for the heat capacity. We notice from Fig.5.24 that always the curves for 600 s are in top of the figure while the 3600 s curves are in the lower part of the figure for all frequencies (1680, 1880, 1980) kHz, and this is because the signal is higher after the 3600 s polarization time and since we scale all the curves to one by dividing by the first value of magnetization we get manually from the saving data (so we divide by a large initial value and hence all the curves will appear in the lower part of the figure) while in the 600 s polarization time you get a small initial value of magnetization and by

dividing the rest of the values by this small value we will get large numbers appearing in the upper part of the figure.

$$\frac{1}{T_z} = \frac{C_T}{C_T + C_z} [M_z] \quad (1)$$

And by using equation 1 and the 0.9 and 0.2 values in Fig.5.24, we conclude that the

ratio $\frac{C_T}{C_T + C_z}$ is equal to $1/(0.9/0.2) = 1/4.5$ and this give us the ratio $\frac{C_z}{C_T}$ equal to 3.5,

while the usual value of the ratio is 3 in the materials that contain only methyl group protons.

We have this big ratio because in this material there are more protons than in the methyl group and this result assures the fact that in our sample we have more different protons.

Also we notice that all the heat capacity curves do not go to zero because during the switching process between the field steps there is some relaxation happening. Finally we notice that for the frequencies (1680, 1880, 1980) kHz the value of the b and c for both polarization times 600 and 3600 s decrease to a minimum at 1880 kHz and then grow again by the approximate values ((11.3, 2.2, 2.6), (3.4, 1.9, 2.08)), ((0.75, 0.11, 0.61), (0.32, 0.11, 0.34)) respectively. In addition a values for polarization times 600 and 3600 s show a decreasing curve with approximate values (20000, 8.1, 5.6) and (20.8, 6.04, 5.23) respectively.

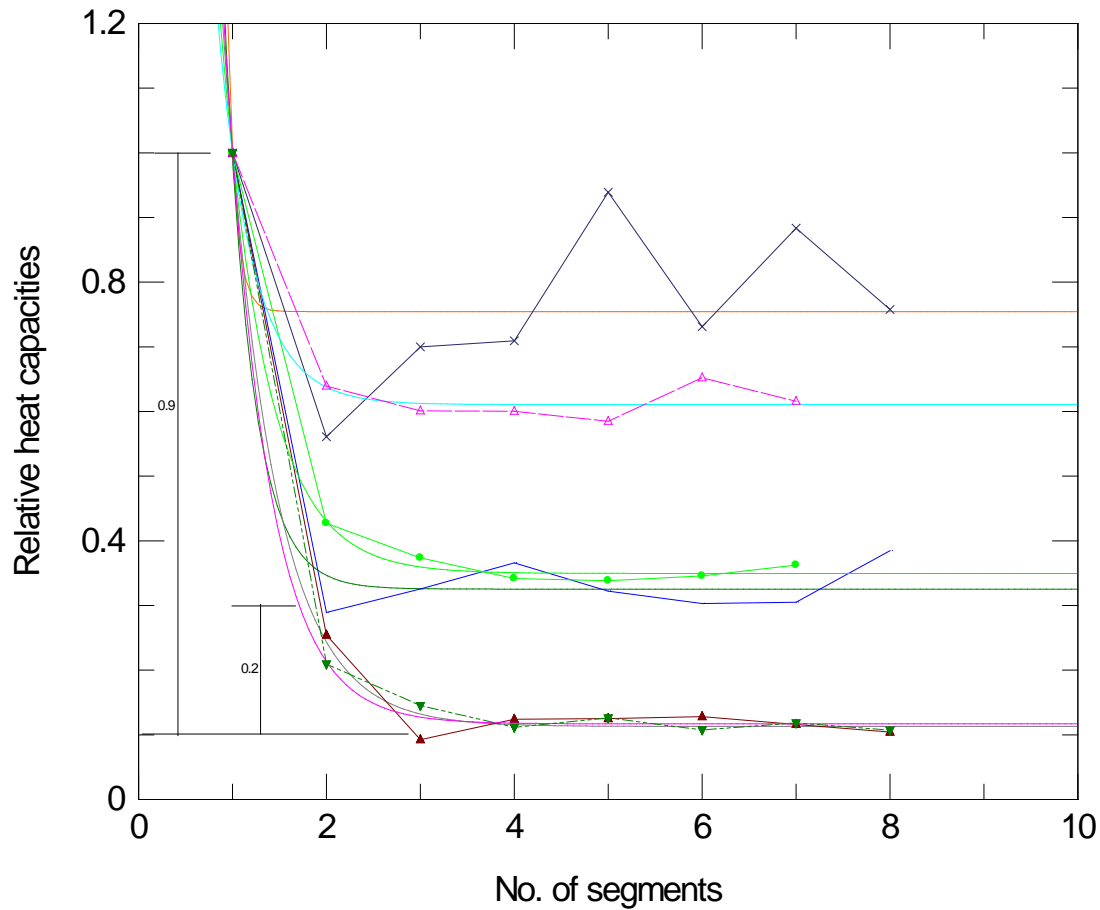


Figure 5.24: The relative heat capacity measurements at the frequencies 1680 and 1880 kHz (on resonance) and 1980 kHz (off resonance) at polarization times 600 s (\times , \blacktriangledown , \triangle) and 3600 s (\circ , \blacktriangle , \bullet) respectively, and we fit all curves to the equation $y=a\exp(-bx)+c$ shown as solid lines.

Chapter 6 Conclusions and discussions (of the most important features

relating to the Dynamic Tunnelling Polarization (DTP) of CH₃ spin-similarity conditions as a Quantum Rotor correspondence of Dynamic Nuclear Polarization (DNP) in the NMR Solid Effect): -

In magnetic resonance a spin – ½ system is characterised by two energy levels split by a Zeeman interaction in the presence of an applied magnetic field. By applying resonant rf pulses, the populations of the two states may be manipulated in a prescribed manner. Indeed by designing custom pulse sequences with many pulses, the spin system may be manipulated in specific ways to reveal insight into the various interactions to which the spins are subject. This is widely exploited across many research activities in magnetic resonance. In the quantum dynamics of molecular rotors, specifically the methyl group, the tunnelling and exchange interactions give rise to two energy levels split by the tunnelling splitting. In this simple and very general sense, the two-level methyl tunnelling system is analogous to a two-level spin-1/2 system. The aim of the principal set of experiments in this thesis, namely those investigating ‘dynamic tunnelling polarization’, is to develop novel experimental procedures for manipulating the polarization of the methyl tunnelling system in a prescribed manner. However, unlike the precession of a nuclear spin in magnetic resonance, the tunnelling polarization does not induce a recordable signal in a coil or other measuring device, so it was also necessary to explore ways in which the tunnelling polarization may be determined experimentally by generating a Zeeman polarization.

A further motivation for the experiments was to investigate whether it is possible to utilise the quantum rotor tunnelling polarization as a means to polarised nuclear spins, thereby providing a technique for creating hyperpolarization. It transpires the experiments which have been devised are analogous to Dynamic Nuclear Polarization

and the solid effect in NMR. For this reason the new experiments in this thesis have been termed ‘dynamic tunnelling polarization’. Both DNP and DTP involve polarization transfer processes between two different two-level systems that are characterised by long relaxation times.

The Pauli Exclusion Principle (PEP) plays an essential role in the description of quantum rotors. It leads to a combination of space and spin eigenfunctions and the establishment of nuclear spin-isomers. The best known example is of orthohydrogen (*o*-H₂) and parahydrogen (*p*-H₂). These are distinguishable species of the hydrogen molecule and significantly the inter-conversion between the two is spin-restricted; the two spin-isomers do not easily come to thermal equilibrium with each other. This means changes in spatial eigenstate of the quantum rotor must be accompanied by changes in nuclear spin state and consequently can only be mediated by interactions that couple space and spin. Such interactions are usually magnetic in origin. The methyl quantum rotor has similar nuclear spin-isomers but in this case they are more commonly known as spin-symmetry species.

Due to the nuclear spin-symmetry, the selection rules mean that electromagnetic radiation is incapable of driving transitions between the nuclear spin-isomers of molecular hydrogen. However, in the case of CH₃, the dipole-dipole interactions between the hydrogen nuclei gives rise to a mixing of the tunnelling-magnetic energy levels. As a result there is a union of *A* and *E* spin-symmetry species and consequently the selection rules become less strict, providing a mechanism for electromagnetic radiation to drive transitions between *A* and *E* states. This gives rise to weak tunnelling sidebands in the NMR spectrum of CH₃ which become weakly allowed. These tunnelling sidebands provide a mechanism for driving prescribed changes in tunnelling polarization by rf irradiation.

The occupant variance of the *A* and *E* type is used as the tunnelling polarization:

$$P_{\text{tun}} = \frac{P_A - P_E}{P_A + P_E} \quad (1)$$

We can describe the reversal tunnelling temperature β_{tun} of these tunnelling conditions with known lifetime by using Boltzmann occupants' data. Also, by using the occupants of the $m_I = \pm 1/2$ Zeeman states, we can describe both the reversal Zeeman temperature β_z with the ^1H spin polarization P_z , respectively.

The DTP pulse sequence that was invented as part of this thesis work succeeded in fulfilling many of the aims that were set at the beginning of these experiments. An example spectrum recorded on Methyl Ethyl Ketone (MEK) or 2-butanone is shown in figure 6.1. Here, at 4.2 K the tunnel frequency is $\omega_t/2\pi = 492$ kHz [33]. Similar data was recorded on Acetophenone (see figure 4.5 in chapter 4).

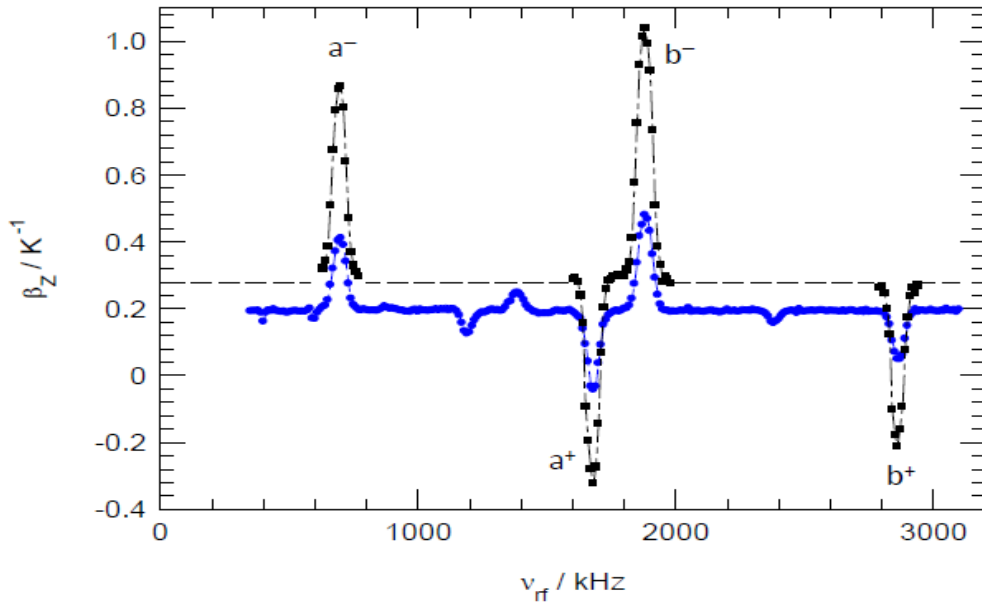


Fig.6.1. Equilibration between tunnelling and Zeeman systems at a level crossing leads to the DTP spectrum of 2-butanone. Here β_z indicates the tunnelling polarization of CH_3 . Significant positive and negative peaks are observed, which are positioned on the $\Delta m = \pm 1, \pm 2$ NMR spectra. (\bullet : $\tau_{\text{pol}} = 270$ s ; \blacksquare : $\tau_{\text{pol}} = 2000$ s . $B_{\text{rf}}=0.028\text{T}$).

In summary, the spectrum (resulted at the field B_{LC}) which denotes the 1H polarization in inverse temperature units, both positive and negative peaks are observed [34]. The positive peaks correspond to NMR sideband transitions that are driven by rf irradiation that drives $E \rightarrow A$ conversion. These are “negative” tunnelling sideband frequencies such as $\omega_z - \omega_t$, and these give rise to a net cooling of the tunnelling reservoir. Of these, the positive peak at 697 kHz (assigned a_-) arises from the $\omega_z - \omega_t$ sideband, while the peak at 1882 kHz (assigned b_-), arises from driving $E \rightarrow A$ conversions at the negative tunnelling sideband frequency $2\omega_z - \omega_t$.

The rf irradiation of the “positive” tunnelling sideband frequencies gives rise to negative peaks. The negative peak at 1680 kHz (assigned a_+), arises from irradiation that drives $A \rightarrow E$ conversion. This leads to a net warming of the tunnel reservoir.

Significantly the negative peaks in the spectra reveal there is a population inversion of the A and E tunnelling levels. The negative peak at 2865 kHz (assigned b_+) arises from $A \rightarrow E$ transitions at the positive tunnelling sideband frequency $2\omega_z + \omega_t$, representing $\Delta m = \pm 2$ spectrum.

In the DTP spectra, the non-equilibrium tunnel states that are created are long lived. This enables their polarization, or the inverse temperature that characterizes the tunnelling reservoir, to be recorded by cross-polarization with the 1H Zeeman reservoir at a level crossing. The effect is closely analogous to the solid effect [17, 35], and dynamic nuclear polarization. However, in this new experiment, the irradiation procedure pumps the tunnel polarization rather than a Zeeman polarization, so we assign the phrase ‘Dynamic Tunnelling Polarization’ DTP to describe it. The DTP peak amplitudes were investigated as a function of initial Zeeman polarization. These measurements showed the tunnelling polarization was directly proportional to the

initial Zeeman polarization, confirming the level-crossing induced cross-polarization mechanism that has been described in the earlier chapters.

Employing the DTP field-cycling sequence, the tunnelling polarization lifetime has been measured by introducing a relaxation period in the DTP pulse sequence, prior to the saturation of the Zeeman reservoir. Because *A-E* conversion involves simultaneous changes in spatial and spin state this lifetime was known to be relatively long. The aim of the experiments was to characterize the lifetime and its magnetic field dependence and therefore to provide experimental insight into the *A-E* conversion mechanism.

The tunnelling lifetime was measured at three magnetic field values and was typically of order two times the $^1H T_1$ at the same field. With its combination of space and spin parts, the intra-methyl 1H - 1H dipole-dipole interaction has the correct symmetry properties to drive the conversion process between spin-symmetry species. Spin-lattice relaxation is driven by modulations of the dipolar interactions so the similarity between the tunnelling lifetime and T_1 suggests a similar mechanism is responsible for *A-E* conversion. That the tunnelling lifetime is longer may be due to the fact that T_1 has both intra-methyl and inter-molecular dipolar components whereas the tunnelling lifetime will be driven only by intra-methyl dipolar interactions. However, to further understand of this mechanism will require more detailed investigations.

An interesting result was obtained for the tunnelling lifetime when the relaxation field was close to the level crossing. In this case the DTP peak is weak in intensity because any tunnelling polarization created by rf irradiation quickly exchanges with the Zeeman reservoir. The tunnelling lifetime is also measurably shorter because of the availability of a level-crossing induced relaxation pathway.

In order to investigate the level-crossing induced cross-polarization in more detail, the *b.* DTP peak was studied as a function of the level-crossing field B_{LC} . As expected,

there is no DTP effect when B_{LC} is greater than the level crossing field. Further, the DTP peak amplitude is a maximum at 0.0115 T where $\gamma B_{LC} = \hbar\omega_t$. However, an unexpected observation is that there is cross-polarization between the tunnelling and Zeeman reservoirs at magnetic fields extending as far as $\gamma B_{LC} = 2\hbar\omega_t$. This provides compelling evidence for mechanical coupling between pairs of CH₃ rotors [36]. This is also indicated by the presence of a DTP peak at $2\omega_z - 2\omega_t = 1384$ kHz in Figure 6.1. The measurement of the tunnelling polarization is an indirect one, being deduced from the ¹H polarization recorded following the level-crossing contact. The calibration depends on the relative heat capacities of the Zeeman and tunnelling systems. We estimate this is of order 6-8 as shown in sections 4.6 and 5.7 with including non-methyl protons in the molecule. Using this value we estimate the tunnelling temperature achieved at a positive DTP peak is of order $\beta_{tun} \approx 6$ K⁻¹, and this is an estimated value which requires further confirmation by investigating it on several materials.

In the DTP experiments conducted in this thesis we have shown how conversion between A and E spin-symmetry species of the methyl group may be induced by rf irradiation of NMR tunnelling sidebands. As a result of this resonant pumping, significant non-equilibrium tunnelling polarizations may be achieved, including inversion of the two-level system. Also, reflecting the strong influence of the anti-symmetry principle and the PEP, these states are long-lived due to the spin-restricted nature of the A-E transitions. The analogy of the DTP effect with the solid effect and DNP has been noted; therefore, exploiting the entanglement of space and spin, the possibility arises that quantum rotor tunnelling polarization may in future be useful in developing schemes for creating hyperpolarized nuclear spin systems. This will require further development and to achieve significant Zeeman polarizations will probably require the exploitation of systems with larger tunnelling frequencies.

Chapter 7 Bibliography

- [1] D.F. Brougham, A. J. Horsewill and R. I. Jenkinson, *Proton transfer dynamics in the hydrogen bond: a direct measurement of the incoherent tunnelling rate by NMR and the quantum-to-classical transition*, Chemical Physics Letters, 272:69-74, 1997.
- [2] H. P. Trommsdorff, M. R. Johnson, A. J. Horsewill and C. J. McGloin, *Proton tunnelling in the hydrogen bonds of halogen-substituted derivatives of benzoic acid studied by NMR relaxometry: the case of large energy asymmetry*, Chemical Physics, 291:41-52, 2003.
- [3] R. I. Jenkinson, A. Ikram, A. J. Horsewill and H.P. Trommsdorff, *The quantum dynamics of proton transfer in benzoic acid measured by single crystal NMR spectroscopy and relaxometry*, Chemical Physics, 294:95-104, 2003.
- [4] J. L. Skinner and H.P. Trommsdorff, *Proton transfer in benzoic acid crystals: A chemical spinboson problem: Theoretical analysis of nuclear magnetic resonance, neutron scattering and optical experiments*, Journal of Chemical Physics, 89:897-907, 1988.
- [5] R. SRINIVASAN, *Tunnelling Processes as studied by Magnetic Resonance techniques*, Physical Chemistry (Series Two, Volume 4) Magnetic resonance, BUTTERWORTHS & CO (PUBLISHERS) LTD , 1975.
- [6] Hund, F., Z.Phys., *Zur Deutung der Molekelspektren. III.*, **43**, 805, 1927.
- [7] Apaydin, F. And Clough, S., *Nuclear magnetic resonance line shapes of methyl groups undergoing tunnelling rotation*, J.Phys.C, Solid state phys., **1**, 932, 1968.
- [8] Allen, P.S. and Clough, S., *Tunneling-Assisted Nuclear Spin-Lattice Relaxation* , Phys.Rev.Lett., **22**, 1351, 1969.
- [9] K.J.Abed and S.Clough, *Methyl tunnelling rotation in the n-alkanes*, volume 142, number (3,4), Chemical physics letters, December 1978.

- [10] Colin A. Fyfe, *Solid state NMR for chemists*, C.F.C. Press, 1983.
- [11] M. J. Barlow, S. Clough, P. A. Debenham and A. J .Horsewill, *Spin thermodynamics and methyl tunnelling*, J.Phys: Condens. Matter 4 (1992) 4165-4171.
- [12] A.J. Horsewill, *Quantum tunnelling aspects of methyl group rotation studied by NMR*, Progress in nuclear magnetic resonance spectroscopy 35 (1999) 359-389.
- [13] Dilip K Roy, *A quantum measurement approach to tunnelling*, World scientific, 1993.
- [14] R. P. Bell, *The tunnel effect in chemistry*, Chapman and hall, 1980.
- [15] Theodore Buyana, *Molecular physics*, World scientific, 1997.
- [16] Malcolm H. Levitt, *Spin Dynamics, Basics of Nuclear Magnetic Resonance*, John Wiley & Sons Ltd, Second edition 2008.
- [17] A. Abragam, *The principles of nuclear magnetism*, Clarendon press. Oxford, 1961.
- [18] E.R. Andrew and L. Latanowicz, *Solid-state proton transfer dynamics and the proton NMR second moment and proton relaxation rates*, Journal of magnetic resonance, 98:232-239, 1986.
- [19] A. J. Horsewill, A. Ikram and I.B.I. Tomsah, *Hydrogen bond dynamics in tetrafluoroterephthalic acid studied by NMR and INS*, Molecular physics, 84:1257-1272, 1995.
- [20] A. J. Horsewill, *Quantum tunnelling in the hydrogen bond*, Progress in nuclear magnetic resonance spectroscopy, 52:170-196, 2008.
- [21] R. V. Pound, N. Bloembergen and E.M. Purcell, *Relaxation effects in nuclear magnetic resonance absorption*, Physical review, 73:679-712, 1948.

- [22] Cheng sun, *Quantum dynamics and tunnelling of methyl rotors studied by field-cycling NMR*, PhD thesis, University of Nottingham/ physics and astronomy department, February 2009.
- [23] A. J. Horsewill, S. Clough and P. J. McDonald, *Methyl tunnelling spectroscopy and level crossing phenomena in solid acetone*, J. Phys.C:solid state phys., 17:1115-1125, 1984.
- [24] A. Kh. Maleev, L.N. Gunderova, N. M. Pozdeev and R. V. Galeev, *Structure and internal rotation of methyl ethyl ketone*, Zhurnal strukturnoi khimii, 29:62-68, January-February, 1988.
- [25] A. J. Horsewill, A. M. Alsanoosi and S. Clough, *Methyl tunnelling spectroscopy in acetophenone*, J. Physics.:Condens. Matter, 1:643-653, 1989.
- [26] Eiichi Fukushima and Stephen B. W. Roeder, *Experimental pulse NMR, A nuts and bolts approach*, Addison-Wesley publishing company, Inc., 1981.
- [27] Jacek W. Hennel and Jacek Klinowski, *Fundamentals of Nuclear Magnetic Resonance*, Longman Group UK Limited, 1993.
- [28] Daniel Canet, *NUCLEAR MAGNETIC RESONANCE Concepts and Methods*, John Wiley & Sons Ltd, 1996.
- [29] C.P.Slichter, *Principles of Magnetic Resonance*, Springer-Verlag Berlin Heidelberg New York, 1978.
- [30] Kuldeep singh panesar, *Quantum molecular dynamics of guest molecules in supramolecular complexes*, PhD thesis, school of physics and astronomy, Nottingham University, 2008.
- [31] Ilya frantsuzov, *An NMR relaxometry study of heteronuclear effects upon proton transfer in hydrogen bonds*, PhD thesis, school of physics and astronomy, Nottingham University, 2010.

- [32] Qiang Xuc, *Proton tunnelling in hydrogen bond studying by NMR*, PhD thesis, school of physics and astronomy, Nottingham University, 2003.
- [33] A. J. Horsewill and A. Aibout, *The dynamics of H atoms in the hydrogen bonds of carboxylic acid dimers*, J. Phys Condens. Matter 1, 10 533 (1989).
- [34] A. J. Horsewill and S. M. M. Abu-Khumra, *Dynamic tunnelling polarization as a quantum rotor analogue of Dynamic nuclear polarization and the NMR solid effect*, Physical review letters, PRL 107, 127602, September (2011).
- [35] A. Abragam and W. G. Proctor, *Une nouvelle méthode de polarization dynamique des noyaux atomiques dans les solides*, C. R. Acad. Sci. Paris 246, 2253 (1958).
- [36] S. Clough, A. Heidemann, A. J. Horsewill, and M. N. J. Paley, *Coupled tunnelling motion of a pair of methyl groups in lithium acetate studied by inelastic neutron scattering*, Z. Phys. B55, 1 (1984).